Alma Mater Studiorum · Università di Bologna

Scuola di Scienze
Dipartimento di Fisica e Astronomia
Corso di Laurea Magistrale in Fisica

Study of the Growth of Ultrathin LiF Films on Ag(100)

Relatore:
Prof. Federico Boscherini

Correlatore:
Dott. Jan Dreiser

Presentata da:
Vladyslav Romankov

Anno Accademico 2018/2019

Abstract

Lo scopo del presente lavoro è stato lo studio sperimentale della crescita di film ultrasottili di fluoruro di litio, depositati sulla superficie (100) dell'argento monocristallino a temperatura ambiente, usando una serie di tecniche, tra cui la spettroscopia di assorbimento di raggi X mediante radiazione di sincrotrone.

La deposizione di film di diverso spessore è stata ottenuta tramite sublimazione della polvere di fluoruro di litio da una cella di effusione in una camera a ultra-alto vuoto. Le superfici dei campioni sono state studiate con un microscopio a effetto tunnel, mentre la struttura e la simmetria della superficie è stata studiata con l'analisi dei pattern di diffrazione di elettroni a basse energie. La struttura locale del fluoro è stata determinata mediante spettri di struttura fine di assorbimento dei raggi X dei campioni depositati e confrontata con quella dei campioni di riferimento. Il dicroismo lineare rilevato da raggi X linearmente polarizzati è stato usato per studiare l'asimmetria della struttura locale del fluoro dei campioni.

I risultati hanno mostrato che sulla superficie (100) del substrato di argento avviene una crescita anisotropa del fluoruro di litio, con la formazione di isole di forma dendritica lungo direzioni preferenziali della superficie del substrato. Una progressiva e inomogenea crescita verticale delle isole è stata rilevata all'aumentare della quantità di materiale depositato. La struttura locale del fluoro dei campioni è stata osservata essere virtualmente identica a quella del volume, con una lieve deformazione originata dal disaccordo reticolare all'interfaccia tra film e substrato e/o il rilassamento della struttura reticolare alla superficie, che ha causato una lieve distorsione del reticolo cubico dei campioni.

Abstract

The aim of the present work was to experimentally study the growth of ultrathin lithium fluoride films deposited on the (100) surface of a silver single crystal at room temperature, by using a range of techniques, including X-ray absorption spectroscopy with synchrotron radiation.

The deposition of films with different thicknesses was performed by sublimation of LiF powder from an effusion cell in a ultra-high vacuum chamber. The surfaces of the samples were studied by scanning tunneling microscopy, while the surface structure and symmetry were studied by the analysis of low energy electron diffraction patterns. The local environment of fluorine was determined by X-ray absorption fine structure spectra of the deposited samples and compared with those of reference compounds. Linear dichroism detected by linearly polarized X-rays was used to study the asymmetry of fluorine local environment of the samples.

The results showed that an anisotropic growth of lithium fluoride occurs on the (100) surface of the silver substrate and that islands with dendritic shape develop along preferred directions of the substrate plane. A progressive inhomogeneous vertical growth of the islands with increasing amount of deposited material was also detected. The observed fluorine environment of the samples is virtually identical to that of the bulk, with a slight strain originated from the lattice mismatch at the film/substrate interface and/or relaxation of the lattice structure at the surface, which resulted in a small distortion of the cubic lattice of the samples.

Contents

1 Growth of Thin Films **8**
- 1.1 The Importance of Thin and Ultrathin Films . . . 8
- 1.2 Surface Structure of Crystals . . . 9
- 1.3 Deposition Procedures . . . 12
  - 1.3.1 Ultra-High Vacuum Chambers . . . 12
  - 1.3.2 Deposition Techniques Overview . . . 13
  - 1.3.3 Thermal Evaporation . . . 15
- 1.4 Adsorption and Surface Diffusion . . . 19
- 1.5 Growth Mechanisms . . . 23
  - 1.5.1 Nucleation and Growth . . . 23
  - 1.5.2 Growth Types . . . 26
  - 1.5.3 Island Shapes . . . 28
- 1.6 Lithium Fluoride . . . 30

2 Experimental Techniques **32**
- 2.1 X-Ray Absorption Fine Structure and Linear Dichroism . . . 32
  - 2.1.1 Synchrotron Radiation . . . 32
  - 2.1.2 X-Treme beamline at SLS . . . 35
  - 2.1.3 Polarization Dependent X-Ray Absorption Spectroscopy . . . 39
- 2.2 Scanning Tunneling Microscopy . . . 43
  - 2.2.1 STM principles . . . 43
  - 2.2.2 Omicron VT-STM . . . 45
- 2.3 Low Energy Electron Diffraction . . . 47
  - 2.3.1 LEED principles . . . 47
  - 2.3.2 ErLEED specifics . . . 51
- 2.4 Quartz Microbalance . . . 52

3 Results and Discussion **54**
- 3.1 Sample Preparation . . . 54
- 3.2 LiF XAFS and XNLD . . . 57
- 3.3 LiF Surface Morphology . . . 66
- 3.4 LEED of LiF/Ag(100) . . . 73
- 3.5 Discussion . . . 77

Conclusions **81**

Growth of Thin Films

1.1 The Importance of Thin and Ultrathin Films

Since last century, our technology developed towards the miniaturization of solid-state electronic devices, which often rely on a sequence of epitaxially grown ultrathin films with atomically sharp interfaces. The development of nanotechnologies requires a constant improvement and understanding of the physical processes occurring in the growth of thin (< 100 nm) and ultrathin (< 20 nm) films [1], as the control of this process allows to exploit the material properties for device applications. One example is the electron confinement in quantum wells. By alternating large and small band gap semiconductor films, it is possible to build heterostructures with tuneable properties, based on quantum confinement of charge carriers in small band gap layers. Such structures are then used to produce ultrafast transistors, lasers and sensors [2]. Because of this, a huge research area developed nowadays, with multiple technologies already on the market, while others still in development.

Another field of application of multilayer structures is the coating of surfaces for purposes such as the anti-reflection treatment for optical interference systems or protective coatings to insulate devices from external environment [3],[4]. By choosing suitable materials and by having a growth control on atomic layer basis, it is possible to choose the exact spectrum for such applications, like extended ultraviolet or even soft X-ray range in anti-reflection coatings [5].

Another example is the stacking of ferromagnetic layers separated by nonmagnetic spacers. In order to mediate the magnetic coupling between two layers, even metallic spacers with few monolayer thicknesses can be used [6]. When insulating or semiconducting decoupling layers are employed, a tunnel junction can form between the magnetic layers. It was shown that it is possible to use an external magnetic field to switch between anti-ferromagnetic and ferromagnetic ordering, in order to control the electric conductance between the layers across the decoupling layer [7]. Because of a strong spin scattering at the interface, such systems develop often a very large magnetoresistance, also called giant magnetoresistance (GMR) [8]. In this case, it is possible to tunnel electrons between the magnetic layers, which has applications in magnetic disk read heads and sensors.

An even more promising application field is the magnetic random-access memories (MRAMs) because of their potentially shorter access and writing times, as compared to nowadays dynamic random-access memories (DRAMs) [2].

The study of insulating tunnel junctions coupled to single-molecule magnets (SMM) or single ion magnets (SIM) is a very promising research field in the last years. In order to enhance the remanence of magnetic molecules deposited on metallic surfaces, epitaxially grown insulating decoupling layers are employed. It was already demonstrated that wide band gap insulators such as MgO allow to use an electron tunnelling barrier to stabilize the magnetic structures on the surfaces [9]. The possibility to epitaxially grow large insulating single (or double) layers on electrode surfaces opened a path to study the evolution of magnetic properties of SIM/SMM over time, and made it possible to reach unprecedented giant hysteresis opening for some systems [10]. Thus, the future of this application, as well as that of other monolayer interface-based technologies, depends strongly on the progress of growth techniques, especially the epitaxial one.

Three-dimensional (3D) growth morphology is also technologically relevant for several applications, like that of optoelectronic devices, single-electron transistors or chemical sensors and heterogeneous catalysis [2]. A typical example of 3D nano-scale grown particles are the semiconductor quantum dots, which are widely employed in several fields, like the solar cell research and development [11],[12].

1.2 Surface Structure of Crystals

If a crystal is cut in two along any arbitrary angle, we have the formation of a surface. The direction of the cut with respect to the lattice sets the orientation of the surface plane. The most important planes are the so-called low-index (or singular) planes, which are the simplest and flattest surfaces and are energetically the most stable. The planes are expressed by the Miller indexes in round parentheses. In metals with a cubic (BCC, FCC) or hexagonal (HCP) structure, for example, those surfaces are expressed by the smallest values of Miller indices possible, like the plane families 100, 110 and 111 (note: a four-index scheme is used for HCP structures). If the surface is cut with a small angle from a low value $(hk\ell)$ surface a vicinal plane is formed.

Singular and vicinal planes cannot maintain a low index structure to match the macroscopic surface orientation, so step-like discontinuities in a sequence of terraces develop along the surface, as shown in Figure 1.1. When there is a high density of steps on a surface, a high-index faceted surface is formed.

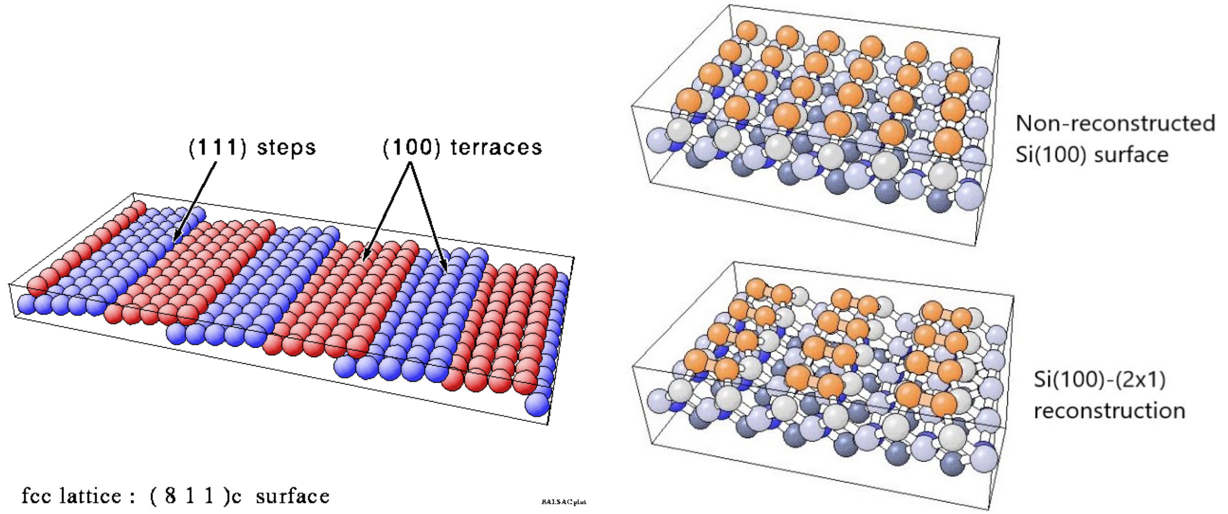

Figure 1.1: (left) An example of vicinal (811) surface of a FCC lattice [13]; (right) the reconstruction of Si(100)-(2x1) surface [14].

Generally, atoms on surfaces have partially unsaturated "dangling" bonds because the crystal structure is suddenly interrupted. This causes an increase of the surface energy, which is unfavourable, and the process of reconstruction takes place. In order to find an energetically more stable configuration, atoms rearrange themselves in a different symmetry from bulk lattice. In most cases a new surface structure is formed, where the symmetry is given by a different binding of the surface atoms to the inner atomic layer, as the electrons from the unsaturated bonds participate in this process.

The combination of stretched and compressed bonds with respect to the bulk structure cause a displacement of atoms toward one (or both) direction of the 2-dimensional surface lattice. The configuration of the surface unit cell can be expressed by the lattice vectors $\vec{a_1}$ and $\vec{a_2}$ of the bulk unit cell, multiplied by two factors m and n, respectively. The most common way to express a reconstructed surface is through the Wood notation [15]:

$$X(hk\ell) - (m \times n) - R\Phi \tag{1.1}$$

where $(hk\ell)$ is the reconstructed surface of the material X and $R\Phi$ is the rotation of an angle Φ of the surface symmetry with respect to the non-reconstructed one. The reconstruction depends strongly on the surface and the material.

A simple example is the reconstruction of the Si(100) surface presented in Figure 1.1. Adjacent silicon atoms gain stability on the surface by getting closer in pairs along the <100>direction, which results in a surface unit cell of double length of that of the bulk, along this direction. The reconstructed pattern is thus labelled as $\mathrm{Si}(100) - (2 \times 1)$.

In transition metals, the electronic states are highly delocalized and correlate poorly with partially occupied single-atom orbitals. Usually, in those materials the surface reconstruction does not occur, while the relaxation process takes place through a variation of the inter-planar distance of the topmost layer of atoms.

The electronic properties of atoms forming the terraces can differ considerably from those at the step edge, which can have a great impact on the surface diffusion, as explained in the following sections. Also, real crystals differ from ideal ones because they exhibit structural defects such as edge and screw dislocations. The first one appears when an extra half plane of atoms is added to the lattice, forming a line of distorted bonds at the edge where the half-plane terminates. The second one requires the crystal to be half-cut until a line of atoms is reached, where the dislocation occurs; the two surfaces are then slipped, one with respect to the other, in the direction of the dislocation, to form a screw-type bonding of atoms around the dislocation line.

A defect may arise at the step as a discontinuity of the ledge (step), called kink. Vacancies are point defects that arise from a missing atom at a lattice point. They are quite common on the crystal surface because their energy of formation is not particularly high, and their density depends on the temperature. Impurity atoms adsorbed on the surface could also act as surface defects. The main surface defects are shown in Figure 1.2 right.

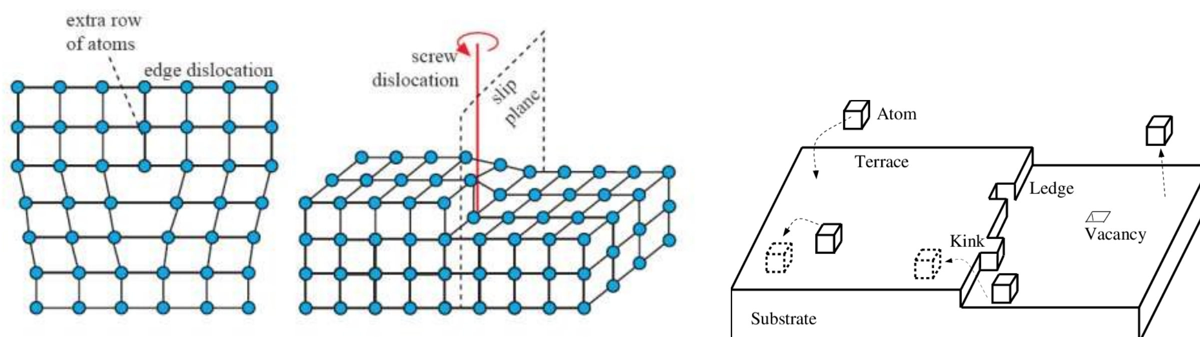

Figure 1.2: (left) Edge and screw dislocations diagram [16]; (right) typical defects present on a surface [17].

1.3 Deposition Procedures

Now that the surface structure of crystals has been introduced, it is time to explain how deposition works. This section starts with a brief introduction of vacuum chambers and technologies, as they are fundamental in the process of film growth. A summary of the principal deposition techniques will follow, where physical and chemical vapor depositions are explained. Subsequently, the evaporation technique is illustrated, along with the main evaporation sources. What happens to the evaporated material at the surface, the adsorbate dynamics and the different types of growth is explained in the next sections.

1.3.1 Ultra-High Vacuum Chambers

The study of surface properties of materials, as well as deposited nanostructures or thin films, requires a particularly clean environment. This is even more true during the deposition process of atoms on a surface, in order to minimize the interaction with contaminations [18]. For this purpose, most of the growth techniques require an ultra-high vacuum (UHV) system, with a pressure below 10^{-9} mbar (10^{-7} Pa or 10^{-9} torr). A detailed explanation, as well as the scheme of the X-Treme UHV system is given in Section 2.1.2. Here we focus on general aspects of vacuum technology.

UHV systems are based on a stainless-steel chamber and an active pumping system to keep the inner pressure as low as possible. The average density of residual molecules is 10^{-6} cm^{-3} for pressures of 10^{-10} mbar. On a standard time span of 10^4 s, typical for surface studies, the residual molecules do not interfere significantly with the experiment. Such low pressure grants these molecules a ballistic motion, so they travel in the chamber from one wall to another in a free molecular flow, with a very low probability of interaction with each other on the stated time span.

Refined experimental procedures are used to reach a good pressure during experiments. The inner walls of the chamber tend to adsorb a layer of molecules on their surface, so it is a common use to bake it out above 100°C for several hours, to get rid of water and other molecules, especially after the exposure to air. Another way to keep good pressure is to use one or several interlocks with smaller volumes, which are used to load and outgas samples from air until a mid-low pressure is achieved. Some systems allow even to preheat samples, in order to accelerate the cleaning process before the sample is transferred into the experimental chamber.

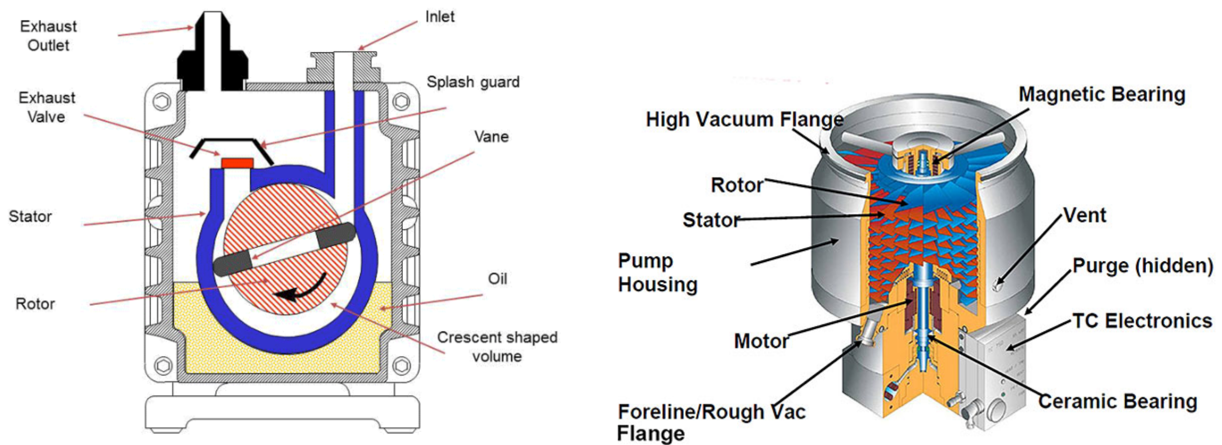

Figure 1.3: Schemes and main components of: (left) a rotary pump [19] and (right) a turbo pump [20].

The key feature to reach and maintain UHV is to use a good combination of pumps. There are two major categories of them: the roughening pumps to evacuate the vacuum chamber to a pressure of 10^0 - 10^{-3} mbar and the pumps for the UHV regime. The most used roughening pumps are rotary (Figure 1.3 left) and membrane pumps. These pumps are fundamental to establish a good vacuum regime for the environment and allow UHV pumps to start operating. When the range of high vacuum is reached, a trigger switches on the UHV pumps. Among a great variety of UHV pumps, the turbo-molecular pumps are the most widespread mechanical ones. The principle of work is based on a fan of several rings of rotating blades with a special geometry that allows capturing and preventing the molecules to get back in the chamber (Figure 1.3 right).

To keep track of the pressure in the experimental chamber and various interlocks, a great variety of pressure gauges can be used, each one with a specific range of operation pressures. It is rather common to find several of them for a single UHV system, each one measuring a specific duct or vessel [21].

1.3.2 Deposition Techniques Overview

In the last years several deposition techniques were developed to coat surfaces with thin films. Despite the great variety of those techniques, two general categories can be drawn, depending on whether the primary process involved is either chemical or physical.

When the method used to deposit the substance is mechanical, electromechanical or thermal, it means the main process is of physical type. There are three dominant techniques of this category: pulsed laser deposition (PLD), evaporation and sputtering. These procedures require high vacuum conditions and are often referred to as physical vapor deposition (PVD). The details of the PLD process are rather complex, but the

working principle is based on laser ablation of the source material through high energy pulses. The vaporized target material emits a plasma plume toward a substrate material, where the deposition process occurs [21].

The evaporation requires a thermal source to vaporize a molten substance and transfer its molecules via a vapor phase onto a clean surface, where deposition occurs. An analogous process occurs when a solid source is sublimed (see next Section 1.3.3).

In the sputtering process, charged ions (usually Ar^+) are accelerated toward a solid target material where sample's atoms are dislodged and scattered away with different energies. A small fraction of those, ballistically fly to the substrate where they deposit as a thin film. There are variants to this technique which can be categorized in four subcategories:

- DC sputtering is the standard setup which uses a diode configuration to charge ions and accelerate them to the substrate surface. It is mostly used to deposit metallic coatings.
- RF sputtering uses high frequency alternate current between electrodes to ionize and deposit insulating films.
- Magnetron sputtering uses magnetic field to confine charged plasma particles close to the surface of the spattered target to increase the probability of ionizing collisions and establish a higher deposition rate.
- Reactive sputtering uses metallic targets and a mix of inert and reactive gases in order to form films of mixed phases or alloys.

The variety of sputtering techniques virtually sets no limits to the kind of material that can be deposited, and the target stoichiometry is generally maintained in the film growth. Unlike evaporation, sputtering does not require ultra high vacuum conditions, so the rate of collisions between particles in the gas phase is higher. In such conditions it is more difficult to have directional evaporation, although it can be achieved with high sputtering rates. The growth of films often presents a less ordered structure, with many different grain orientations [15].

The chemical vapor deposition (CVD) is the process of chemically reacting a volatile compound with other gases to deposit a non-volatile material on a suitable substrate. Generally, a precursor is introduced in the chamber where, with specific thermodynamic conditions or laser/plasma supported systems, a chemical reaction occurs between the substance and the substrate. After this process, the first gas is pumped out and a second one could be introduced for another reaction to occur. This sequence continues with several cycles, at the end of which a film compound of required thickness is grown.

Films and coatings produced with high-temperature CVD processes have found a wide application in the production of solid-state electronic devices, fabrication of metalwork tools, rocket engines and nuclear reactor components. The possibility of scaling up the process and the ability to produce a large variety of crystalline and amorphous films, with a good control of stoichiometry and high purity, made this technique one of the most developed and employed in industry.

CVD enlists different techniques that depend on the pressure conditions, the physical characteristics of the vapor, the substrate thermodynamic state, the use of hybrid combination of physical processes and chemical reactions. In the last decades two very special CVD techniques emerged and established their importance. The first is the metalorganic chemical vapor deposition (MOCVD), a process for growing crystalline layers to create complex semiconductor multilayer structures, which is widely used in the manufacturing of optoelectronics. The second is the atomic layer deposition (ALD), by which alternating atomic layers are grown in a cyclic manner, using two or more precursors that exhibit self-limiting surface reactions on the substrate [15],[22]. These two techniques are somewhat complementary, although there are some major differences between them, which are explained elsewhere [23],[24].

1.3.3 Thermal Evaporation

Evaporation is one of the main physical vapor deposition (PVD) techniques to deposit thin films onto a surface. As stated in the previous section, the key feature of it is to vaporize (or sublime) a source material in order to have a stable flux of atoms/molecules on the substrate. If the source is kept in solid phase, the process of sublimation occurs instead. From kinetic gas theory [25], it is possible to derive an equation for the flux of the atoms in vapor phase, known as Hertz-Knudsen equation:

$$\varphi = \frac{\alpha N_a (P_e - P_h)}{\sqrt{2\pi MRT}} \tag{1.2}$$

In which φ is the number of evaporated atoms per unit area per unit time, α is the evaporation coefficient that ranges from 0 to 1, N_a is the Avogadro number, M the mass of the atoms, R the perfect gas constant, T the temperature of the substrate. In this equation P_h is the hydrostatic pressure applied on the surface of the material while P_e identifies the equilibrium vapor pressure of the material at a given temperature. The relation between the equilibrium vapor pressure of an element and its temperature can be found in the Clausius-Clapeyron formula (1.3), which states that an infinitesimal variation of enthalpy and volume of any material influences the pressure and the temperature of its equilibrium, at a given phase.

$$\frac{dP}{dT} = \frac{\Delta H(T)}{T \Delta V} \tag{1.3}$$

This allows to define a curve of coexistence between different phases of a substance but can also be used to find out the vapor pressure at a given temperature. If the molar enthalpy of evaporation $\Delta H(T)$ can be approximated as constant and the law of the perfect gas holds, the (1.3) can be simply integrated to have (1.4), where I is an integration constant.

$$LogP = \frac{\Delta H(T)}{RT} + I \tag{1.4}$$

The Arrhenius plot of the previous equation could be drawn for most elements and an example is shown in Figure 1.4. From this plot it is possible to extrapolate the temperature needed by an evaporation source to have a good vapor pressure and thus a good flux of particles for the deposition [25],[26].

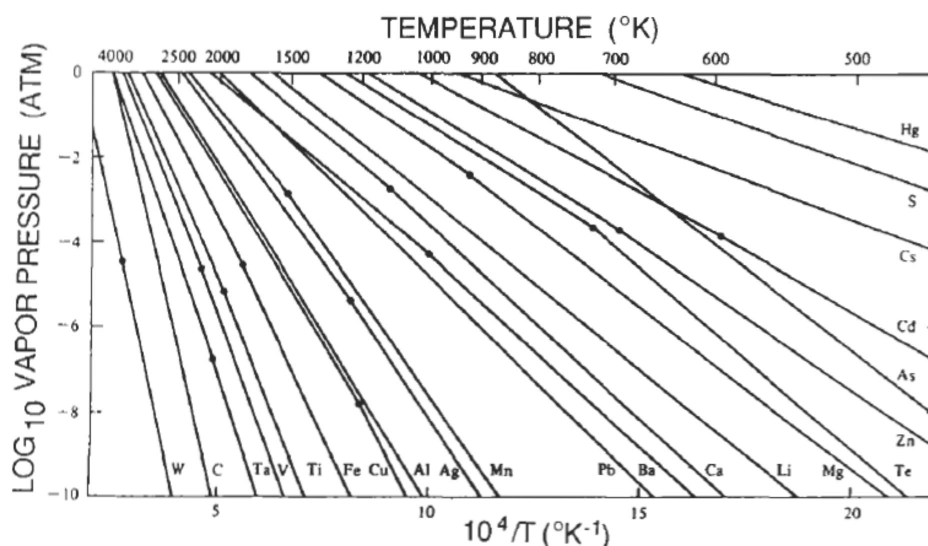

Figure 1.4: Arrhenius plot of log P vs 1/T for several materials [27].

When the source material is a single element (eg. Ag), the evaporation occurs mostly in form of single atoms [27]. For most compounds the vapor composition is likely to differ from that of the original solid or liquid source. A molecular association (or dissociation) can easily occur and the stoichiometry of the deposited film is usually different from that of the source.

The constituents of such compounds tend to evaporate almost independently, and each species enter the vapor phase seemingly to the pure metals. Given a binary alloy AB, from the Raoult's law is possible to evaluate the ratio between the evaporation fluxes as:

$$\frac{\varphi_A}{\varphi_B} = \frac{\gamma_A \chi_A P_A}{\gamma_B \chi_B P_B} \tag{1.5}$$

in which γ is the activity coefficient, χ is the molar fraction and P is the vapor pressure for each of the components. A practical application of equation (1.5) is difficult due to variation of the composition of the source over time. To match the stoichiometry of the evaporating material, the ratio estimation from equation (1.5) could be a good reference to understand the amount of enrichment needed to compensate the loss of the source element evaporating the most. In case this solution is impossible, evaporation from two sources maintained at different temperatures is required.

The heat sources used for the evaporation must match the properties required for the deposit of the specific material. They must reach the temperature required for the process to occur without reacting, contaminating or alloying with the source. Also, their vapor pressure must be negligible compared to that of the substance at issue, and they must not release reactive atoms such as oxygen, hydrogen or nitrogen. These requirements led to the development of devices based on resistant filaments and electron-beam heated sources.

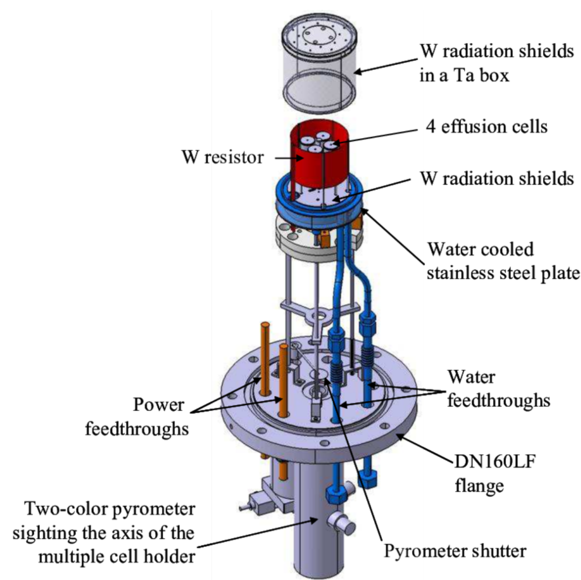

Figure 1.5: Typical Knudsen thermal evaporator with 4 effusion cells [28].

The most used joule-heated device for thermal evaporation is the Knudsen effusion cell (Figure 1.5). The working principle consists in heating, usually with a tungsten wire, a cell containing a crucible where the evaporating material is allocated. Crucibles are small sockets of a refractory oxide or another suitable material (molybdenum, tantalum, quartz, etc.) which are heated by a tungsten coil wrapped around it. They have different shapes depending on the geometry of the device. The wire is surrounded by radiation shields and an active water cooling shroud to avoid the overheating and the outgassing of the vacuum flanges. The water and the current for the filament are provided by feedthroughs

designed for UHV systems. For a reliable temperature reference, a thermocouple is placed close to the sample.

The evaporation occurs in a broad conus shape, with a flux of particles following a cosine distribution, where the angle is taken from the normal of the crucible aperture. At the normal direction from the source, the flux is at maximum value, reaching a null value on directions perpendicular to it. A movable metallic shutter is placed in front of the aperture, which allows to quickly start/stop the evaporation flux of the outgoing atoms to the substrate direction. To narrow the flux distribution pinholes with different sizes could be placed in the flange between the cell and the substrate. The cell is usually placed closer to the deposition surface to increase the rate of the impinging atoms, bearing in mind that its high temperature could thermally affect the substrate, if the distance is too small (the actual safe distance depends on the system configuration).

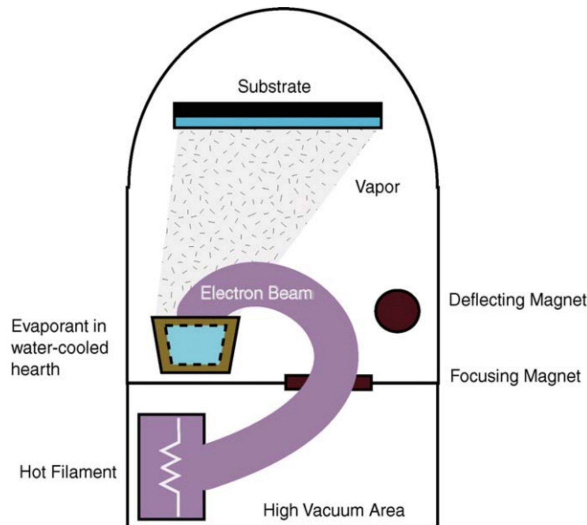

Figure 1.6: A typical configuration of an electron beam evaporator [29].

An alternative to the effusion cell is the electron-beam evaporation. The most common configuration has a gun which emits a beam of electrons from a negatively biased cathode (filament) by thermionic effect. The electrons are accelerated toward a grounded anode with a voltage difference from 4 to 20 kV. The beam is shielded from a direct line of sight of the substrate and the substance held in the crucible. A transverse magnetic field is applied to the beam to deflect the electron trajectory by 270° and focus the electrons in the middle of the crucible (Figure 1.6). This setup allows to avoid any contamination from crucibles, heaters and supporting materials, especially for the high melting point substances, while keeping a good evaporation rate. The high purity of deposition is granted because only a small spot of the source material melts or sublimes, the rest of it forms a natural shield all around, thus preventing the overheat of the crucible [23],[30].

1.4 Adsorption and Surface Diffusion

Evaporated atoms approaching the substrate surface with rate F, which depends on the partial pressure of the gas, could interact with it through different "scattering channels".

Elastic scattering happens when there is no energy exchange occurring between a particle and the surface. This is the main channel for electrons and small atoms/molecules (e.g. H_2, He), and is widely used to study the surface structure via techniques such as LEED (see next Chapter 2.3).

When the atom loses/gains energy, the scattering is inelastic, which may occur as "direct inelastic scattering" or trapping/sticking. The main difference between the two could be linked to the time of interaction of atoms with the surface. In the former case, an atom interacts by gaining or losing energy and momentum, after which is *immediately* scattered back to the gas phase. In some cases, however, when an atom loses enough energy, it can be trapped on the surface. If this happen, the atom may still return to the gas phase by desorption after a temporary permanence close to the surface. The kinetics of desorbed atoms is governed, then, by the surface temperature, as they do not preserve the memory of the previous vapor phase. If, however, the atom sticks to the surface in a more permanent bound state, it's called adsorbed. The probability with which an atom is adsorbed is given by the sticking coefficient σ_S, a number below unity which expresses the strength of interaction of the atomic species with the surface.

The sticking coefficient is a dynamic quantity that depends mainly on the energy of the incoming atoms/molecules, the surface adsorbate coverage and the free binding states, as well as the specific atom-surface interaction potential barrier. At equilibrium, the interplay of adsorption and desorption processes determines the probability of an atom to stick to the surface, with an Arrhenius dependence of the coefficient from the temperature.

In order to be adsorbed on the surface, an incoming atom may, or may not, encounter an energy barrier to overcome. When no energy barrier is present on the surface of the substrate, the process is called "non-activated adsorption" and can be illustrated via a 1D Lennard-Jones potential graph, as the one shown in Figure 1.7.

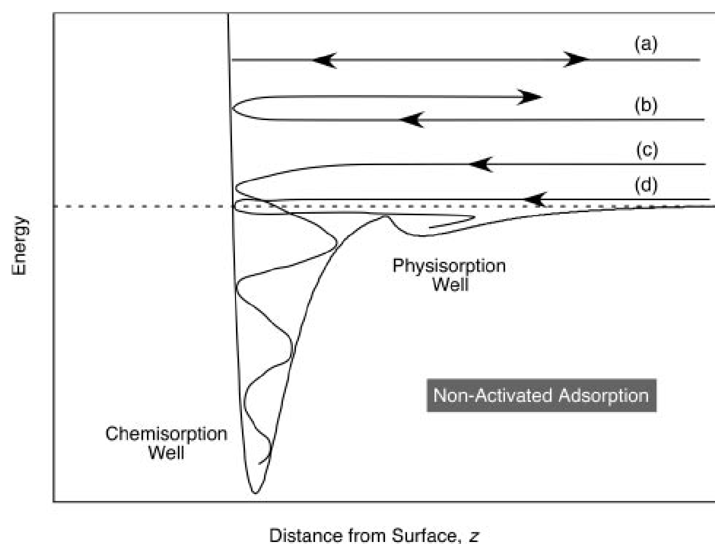

Figure 1.7: A one-dimensional representation of non-activated adsorption: (a) elastic scattering trajectory; (b) direct inelastic scattering trajectory; (c) sticking event (chemisorption); (d) sticking event (physisorption) [15].

The binding of an adsorbate on the surface can occur via two types of interactions: a chemical or a physical one. The former interaction is called chemisorption and it is the strongest type, as chemical bonds are formed between the adsorbate and the substrate. In this case, the particles reside at the closest equilibrium binding position to the surface. The adsorption sites depend on the dangling bonds and the co-ordination of the surface atoms. The adsorbed atoms are usually bound in a stable position at a fixed mean distance from the surface where the potential well minimum is located (Figure 1.7).

Physisorption happens when particles bind weakly to the substrate. In this case, weak dipolar Van der Waals force keeps the atoms adsorbed to the surface. In general, the higher the energy of the incoming particle the lower is the sticking coefficient as the probability to bounce on the surface and come back to the gas phase is greater.

In some cases, the sticking coefficient could increase with temperature of adsorbed atoms. This is the case when a potential barrier is present on the surface and an activation energy is required for the atom to overcome it (Figure 1.8). Therefore, this process is usually called "activated adsorption". Low energy particles hitting the surface are bounced back, while those atoms that have a sufficiently high energy can end up in the chemisorption potential well.

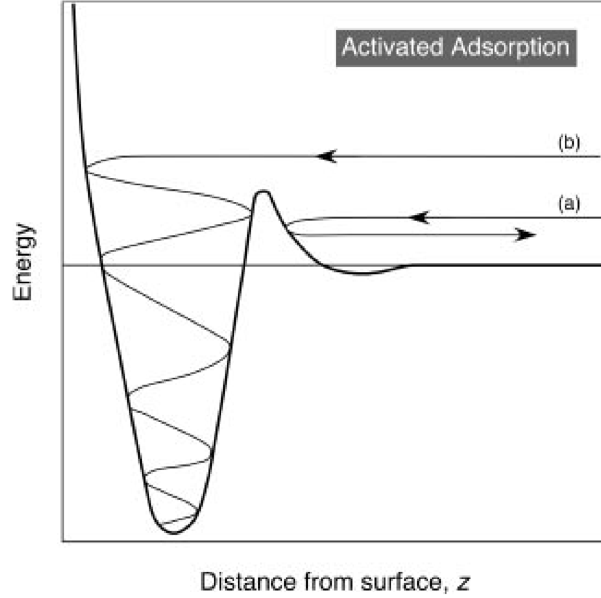

Figure 1.8: A Lennard-Jones potential diagram for activated adsorption in one dimention. The energies of two hypothetical trajectories at (a) low and (b) high kinetic energy are shown [15] .

Adsorbed atoms are bound to the substrate along the direction normal to the surface, but they can diffuse on the surface plane through thermally activated jumps. Assuming the classical model with a parabolic potential in one dimension, it is demonstrated [27] that the jump rate Γ of atoms from a local low energy site to the neighbour one is given by:

$$\Gamma = \nu e^{-\frac{E^m}{k_B T}} \tag{1.6}$$

Where E^m is the barrier energy of migration, k_B the Boltzmann constant, T the temperature and $\nu = \frac{1}{2\pi}\sqrt{\frac{\beta}{m}}$ is the attempt frequency, which depends on the mass m and the restoring-force constant β of the potential well. Although models like the Transition State Theory (TST) [2] can better predict the experimental behaviour of the attempt frequency, the values of such frequency are typically close to the Debye range of $10^{12} - 10^{13}$ Hz. The term E^m usually takes into account both the potential energy barrier of the well and the vibration contribution arising from the lattice dynamics.

Atoms possessing enough energy to overcome this potential barrier can jump in the neighbour low energy site, with a displacement given by $\vec{r}$. The formula (1.2) shows that, the higher the temperature of the lattice, the greater is the diffusion rate of the particles. At thermodynamic equilibrium, after a time τ, each atom will execute $N\tau = \Gamma\tau$ jumps in a random walk motion. It can be demonstrated [27] that the mean square

distance covered by an atom after a time τ is proportional to the mean-square jump distance $< \vec{r}^2 >$ multiplied by $N\tau$. It is then possible to assume the diffusion from an instantaneous point source model and see how the atomic jump rate is related to the macroscopic diffusivity D. Given the gaussian concentration profile:

$$c(r,\tau) = \frac{n_d}{(4\pi D\tau)^{3/2}} e^{-\frac{r^2}{4D\tau}} \tag{1.7}$$

where n_d is a constant, it is possible to demonstrate [31] that $D = \frac{N_\tau < \vec{r}^2 >}{2d\tau} = \frac{\Gamma < \vec{r}^2 >}{2d}$, with d number of dimensions. In case of surface diffusion (2D) it can be written:

$$D^* = D_0 e^{-\frac{E^m}{k_B T}} \tag{1.8}$$

where $D_0 = \frac{\nu < \vec{r}^2 >}{4}$ and D^* is called tracer (or intrinsic) diffusion. The tracer diffusion is usually different from the chemical (or collective) diffusion used in Fick's law, but in case of low-growth rate the mean inter-particle distance can be considered large enough to allow the use of the tracer diffusivity to determine the cluster densities [22]. Multiple concurrent diffusion processes can occur on a free surface, so the understanding of all the mechanisms that are involved can be a very complex task. Nevertheless, the most common phenomena are illustrated in the Figure 1.9.

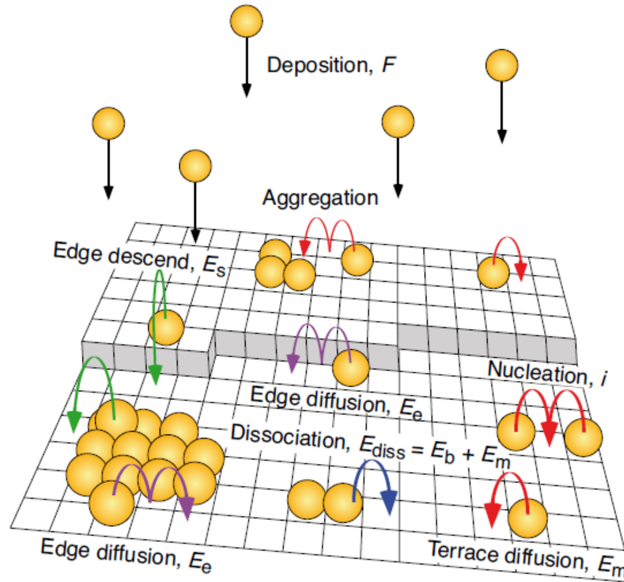

Figure 1.9: Typical diffusion processes occurring on a crystal surface [22].

Terrace migration, which is expressed by the intrinsic diffusivity above, is usually the dominant process. This process is mostly anisotropic, as the symmetry of the substrate

determines the migration energy barrier and can enhance the diffusion rate in certain directions. The crossing of the edge of an atom diffusing across a step of the substrate or descending from an already-nucleated cluster is often subjected to the Ehrlich-Schwoebel barrier E^s, which can block the atoms from this process. Edge diffusion has an energy barrier E^E and usually happens along the step edge of the substrate or along the edge of a cluster. This diffusion is critical for the nucleation and growth process, especially if the heterogeneous nucleation is the dominant process.

Other mechanisms of atom diffusion involve dislocation and vacancy diffusion and usually enhance the adatom diffusion rates. An adsorbed atom can also diffuse through the exchange mechanism, where an atom from the substrate is pulled out the lattice and replaced by the diffusing one [27]. When a diffusing atom collides with one or more of their own, or when a structural or chemical defect is met, the diffusion stops and the nucleation process could take over [2],[18].

1.5 Growth Mechanisms

1.5.1 Nucleation and Growth

The formation of a thin film on a surface is a non-equilibrium process that requires several steps to occur, like the nucleation of multiple atoms into small clusters, the growth of such clusters and their coarsening to form, in the end, a single layer. As explained later, the formation of a stable film could occur through different growth mechanisms, according to the favourable growth type, and most of the time is not a straightforward process.

The nucleation is usually treated as a four-stage discontinuous phase transition at constant temperature [27]. The four stages are presented in Figure 1.10, and can be explained as following:

- Stage I is the incubation period in which particles continuously aggregate and dissociate to form small clusters, until a critical stable size is reached.
- Stage II is the quasi-steady-state nucleation regime, where stable nuclei are being produced at a constant rate, such that the number of nuclei N increases over time.
- Stage III shows a decrease of the nuclei formation rate due to a decrease of the driving forces of the process and the growth process takes over.
- Stage IV occurs when the coarsening process dominates, and the nucleation of new clusters become more and more negligible.

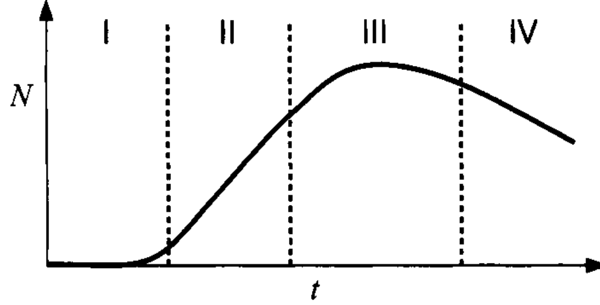

Figure 1.10: Number of clusters N formed per unit time during the nucleation process as a function of time t, for a fixed temperature [27].

We distinguish two cases of nucleation. The homogeneous nucleation occurs when the atoms aggregate on the terraces, without the involvement of a surface defect. Particles impinging on the surface with rate F, diffuse on the terraces with rate D^*. The nucleation starts when a critical number of particles N_C aggregate together to form a stable cluster. In order to keep the particles in a bound state, the free (bulk) energy of the cluster must overcome the interfacial energy γ, which acts as a potential barrier for the nucleation. It is possible to demonstrate [27] that, in order to overcome the critical potential barrier ΔG_C, a minimum number of particles N_C have to bind together, with a relation:

$$\Delta G_C = \frac{1}{3}\eta\gamma N_C^{2/3} \tag{1.9}$$

where η is the geometrical factor and γ is the interfacial energy per unit interfacial area (assumed to be isotropic). As the particles bind together in form of a small cluster, a critical cluster size is reached when N_C particles bind together. From that point, the rate of adsorption of particles to the cluster is greater than the desorption and the clusters proceed toward the growth phase.

The formation of new stable clusters increases the cluster density n_x. Generally, the cluster density depends on several factors, the main being the diffusion processes. There usually exists a threshold density of islands, after which further deposition leads most exclusively to the growth of existing clusters into bigger islands. The mean-field nucleation theory [30] relates the island density to the diffusivity D^* and the deposition rate F as follows:

$$n_x = \eta(\theta, i)\left(\frac{F}{D^*}\right)^{\frac{i}{i+2}} exp\frac{\Delta G_i}{(i+2)k_B T} \tag{1.10}$$

Where i is the critical cluster size, ΔG_i is the cluster binding energy and $\eta(\theta, i)$ is a function of surface coverage θ, in terms of a monolayers (MLs) of adsorbed atoms [2]. Because the diffusion constant varies exponentially with temperature, the density of the

islands decreases rapidly with temperature, while the average isle size increases. In the formula above, the $\frac{F}{D^*}$ term is proportional to the sixth power of the mean diffusion length of an adatom before a nucleation process occur, in the compact islands and coverage saturation regime. From this parameter it is possible to estimate which type of nucleation could occur on a surface [2].

When the nucleation takes place at point or line defect, the process of heterogeneous nucleation occurs. This case is similar to the previous one, but the energy ΔG_i has an additional contribution coming from the defective state that lowers the value of the nucleation barrier, and thus facilitate the self-assembly of particles on surface defects and along step edges.

In the later stages of the growth process, the mechanism of coarsening is usually the dominant one. It consists of diffusion of different-sized clusters, driven by the tendency of an overall minimization of the cluster interface with the surrounding environment. As smaller clusters have more surface atoms, the growth of large island at the expenses of the smaller ones is usually energetically more stable.

The process of Ostwald ripening is the main coarsening mechanism for solid solutions and it was explained by the mean field theory of Slyozov and Lifshitz [31]. Depending on the limiting mechanism, the process could be diffusion or source limited. In case of diffusion of adsorbate on a surface, the theory was adopted to fit the experimental results, such that from the atomic point of view, atoms evaporate from the edge of an island, then diffuse toward another island and condensate at its step. It can be demonstrated [32] that the temporal evolution of the area A of an island with radius r is:

$$\frac{dA}{dt} = -\beta(\rho(r) - \rho_{eq}(r)) \tag{1.11}$$

where $\rho(r)$ is the density of adatoms in the vicinity of the island, while $\rho_{eq}(r)$ is the adatom equilibrium density for circular islands with isotropic step free energy and substrate cell density n [22]. The rate β includes several contributions, such as the step evaporation, the terrace diffusion and the step condensation barriers, as well as the three preexponential factors. The equation (1.11) can also be rewritten as [32]:

$$\frac{dA}{dt} = \frac{2\pi D\rho_\infty \gamma}{n^2 k_B T} \frac{1}{ln(\frac{R}{r}) + \frac{a}{kr}} \left(\frac{1}{r_C} - \frac{1}{r}\right) \tag{1.12}$$

which depends on the critical radius r_C for the process to occur, where R is the radius of the island where ρ dominates over ρ_∞, and k and a are parameters depending on the specific system. In this regime, called the "diffusion limited coarsening", the temporal evolution of the radius is $r(t) \propto t^{1/3}$ [27].

In most experiments the surfaces are analyzed some time after the deposition, whether the substrate is held at the deposition temperature or not. In this conditions, the adsorbed monomers continue to be mobile even after the incoming flux of atoms is stopped, and the nucleation process or the island growth can proceed further. This effect is called

post-nucleation and post-growth and it could be still very important in determining the final shape of the islands or the formation of films [22].

1.5.2 Growth Types

In general, the growth modes of a thin film deposited on a substrate are classified by thermodynamic arguments [2]. The strength of the film-substrate interaction determines the structure and the morphology of the film, which can be explained by the Young's equation. For a planar geometry of the substrate, the Young's equation for surface tension states that at equilibrium the film forms an angle θ with the substrate:

$$\gamma_S = \gamma_i + \gamma_O \cos\theta \tag{1.13}$$

The three surface free energies per unit area γ refer to the substrate/vacuum (S), substrate/film (i) and film/vacuum (O) interfaces(Figure 1.11).

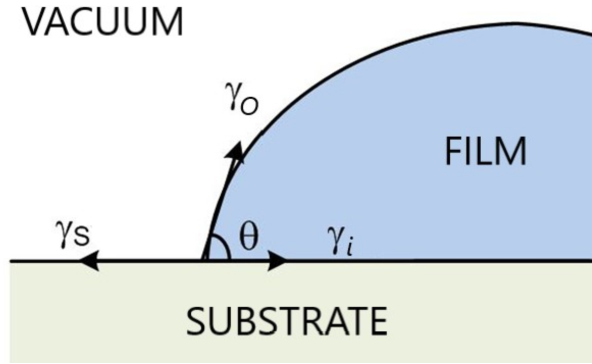

Figure 1.11: Formation of the film on a substrate according to Young's equation [33].

If a film is composed by n layers and γ_i and γ_O are small compared to γ_S, such that $\gamma_i(n)+\gamma_O(n) \leq \gamma_S$, the system will be stable if the growth occur on layer at a time. This type is called Frank-van der Merwe (FM) mode and is typical for systems with adhesive forces stronger that the cohesive ones.

On the contrary, when $\gamma_O(n) > \gamma_S$ the system prefers to form 3D islands and the growth mode is called Volmer-Weber (VW). There is a third mode, called Stranski-Krastanov, which is a mixture of the previous two: after a first "wetting" layer is formed, which may consist of several layers, the system is still more stable by forming three-dimensional islands on top. These three modes are presented in Figure 1.12.

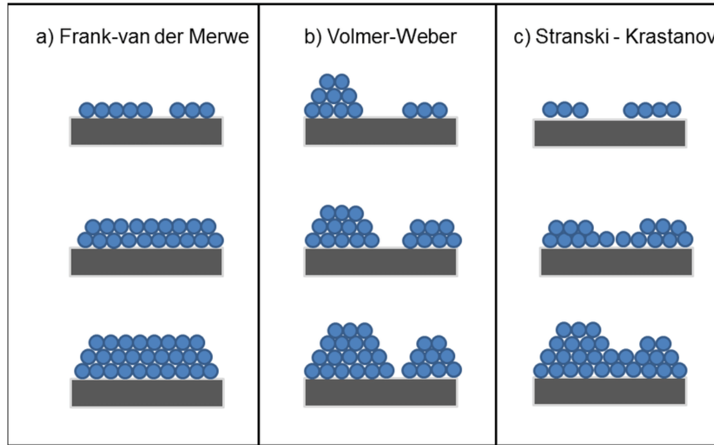

Figure 1.12: Epitaxial growth modes of adsorbed atoms on a free surface [34].

The growth mode could be largely affected by the lattice misfit at the interface. Even within the epitaxial growth boundaries, the misfit generated by compressive or tensile strain parallel to the surface affects the interfacial energies. So, for example, by increasing the lattice misfit for a system with preferred Stranski-Krastanov growth mode it is possible to shift it toward the Volmer-Weber type [2].

The growth mode of thin films deposited by vapor phase can also be predicted by the classical structure-zone model (SZM) proposed by Movchan and Demchishin [35]. This model links the growth process to regimes defined by the homologous temperature, that is the substrate temperature T relative to the melting point of the film material T_m. The model was further expanded to include important effects of different deposition techniques, in order to give a general and simple picture of the deposition process.

By sorting the conditions of the film growth into regimes where a small number of physical processes dominate, it is possible to predict the general structure of the film, without considering the interface that is formed on the substrate. However, this model is meant to be a general guideline in understanding the outcome of the film deposition for given thermodynamic conditions and is not to be used in quantitative way.

The basic assumptions are that the film growth occurs via a three-steps process, where the first step is the transport of the evaporated atoms to the substrate. The second step is the adsorption, surface diffusion, nucleation and growth, as well as any chemical reaction that may occur on the surface for the atoms to bind to the surface. The third step involves atomic diffusion of atoms toward their final and stable positions through bulk diffusion and solid-state reactions. At sufficiently low temperatures the surface diffusion is usually low, so that atoms have poor mobility after sticking and the growth is dominated by the incoming atom flux. These conditions are favourable to the segregation of atoms into separate islands and a vertical growth into columns form, also referred to as columnar growth (Figure 1.13).

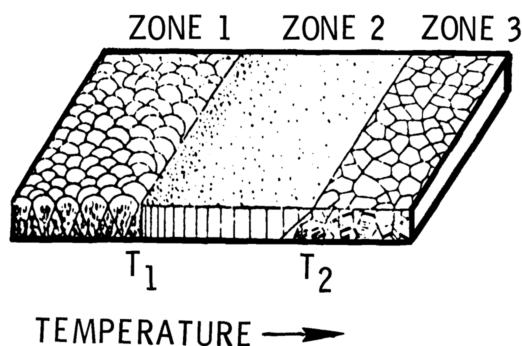

Figure 1.13: Structure-zone diagram introduced by Movchan and Demchishin from their study of vacuum evaporated metals and oxides [35].

This regime is usually called zone 1 and is highly sensitive to the direction of the incoming atoms. Zone 2 regime happens when the homologous temperature $T/T_m < 0.5$. The activation energies for surface diffusion are low enough such that it becomes the leading mechanism by forming columnar grains with defined grain boundaries and larger grain widths, compared to those of Zone 1. At high enough temperatures the bulk diffusion becomes the dominant process and the film grows by forming equiaxed grains.

Although such definitions were later modified by adding intermediate zones and by shifting the threshold temperatures [31], the original model is still useful to understand the general trend of the film formation.

1.5.3 Island Shapes

The correlation of the thermodynamic conditions, such as pressure, temperature and humidity, to the shape of the grown crystallites in nature, revealed that the shape is dominated by material transport at the surface (or interface), where the diffusion is usually the rate-limiting process [36]. This mechanism is exactly the same that governs the self-assembly of clusters on a free surface of a crystalline substrate held at low temperature [2]. In some cases, like the aggregation of sub-monolayer coverages of metal atoms on a singular surface, the structure is two-dimensional and much easier to understand than more complex 3D patterns. At thermodynamic equilibrium, atoms can desorb from clusters and condense again at different positions, until the total energy of the island is minimized.

If the islands have anisotropic steps with different surface free energies γ, then the length of these facets evolve according to the Wulff construction, until the equilibrium shape is reached. In this case, the shape is not given by kinetic limitations and the steady-step atom exchange between different facets can be detected by small step oscillations through STM/AFM imaging [2].

The substrate temperature is a strong factor in determining the evolution of island shapes, and by increasing such temperature it is possible to have a transition from less to more ordered sub-monolayer structures for a large variety of materials. Besides greatly affecting the adatom surface diffusion and nucleation processes, as explained in the previous sections, the thermal energy can promote the transition from a metastable configuration of islands to a more stable one, by bringing the system from a configuration at a local energy minimum to the global one. Thus, deposition at different substrate temperatures, or a subsequent annealing of the system, could lead to different shapes of islands, according to the interplay of the relevant mechanism energies.

An example is the formation of randomly oriented branches in fractal growth that occurs at low deposition temperature. In this case, the slow edge diffusion of adatoms leads to the formation of tips, due to the Saffman-Taylor instability [37]. The statistical fluctuations of adsorbed atoms lead to the formation of such protrusions, which captures terrace-diffusing adatoms with a higher rate than straight or concave step sections.

If the edge diffusion is low comparing to the capturing process, the protrusions grow out as branches, forming fractal-shaped islands. When a branch is sufficiently long, the tip becomes exposed to a great solid angle of incoming atoms, causing the ramification into secondary branches. This ramification thus forms a self-similarity of the growth patterns with the increasing of the island dimensions.

In some cases, the substrate surface symmetry can play a major role by conditioning the island edge diffusion or even the terrace diffusion itself. When the anisotropy of the adsorption sites becomes strongly directional, the islands assume a dendritic shape. The preferred growth directions are then those which minimize the interfacial energy of the cluster, whether the system is in its local or global minimum. This minimization occurs when atoms diffusing on the terraces and along the cluster edge binds to energetically favourable sites at the cluster edge. These sites thus have a higher capture rate for the diffusing atoms and the growth proceeds along the directions of the energetically favourable sites [2].

As stated in the Section 1.4, the terrace diffusion can also be anisotropic, as adsorbed low-energy atoms prefer to follow the crystal directions which offer less "resistance" in terms of diffusion energy barrier. The strongly directional surface diffusion, combined with the anisotropy of the island growth, can explain the surface dendritic growth of low temperature deposited systems [2],[38],[39].

In some systems the terrace diffusion and island edge diffusion energies are comparable. Once a process gets thermally activated, the other follows, leading to compact islands formation, with the shape given by the substrate symmetry and island anisotropy, as stated previously.

1.6 Lithium Fluoride

Lithium fluoride is an inorganic compound widely used in industry applications both as a bulk crystal and as a thin film coated over other substances. Its chemical formula is LiF and it is a binary phase of lithium (Li) and fluorine (F), which makes it part of the alkali halide group.

Halides are known to be insulating materials, with their properties originating from the bond of a halogen atom and a less electronegative atom, such as an alkali metal. Among all halides, lithium fluoride has the largest band gap and it was used so far for its peculiar optical and electronic properties [40].

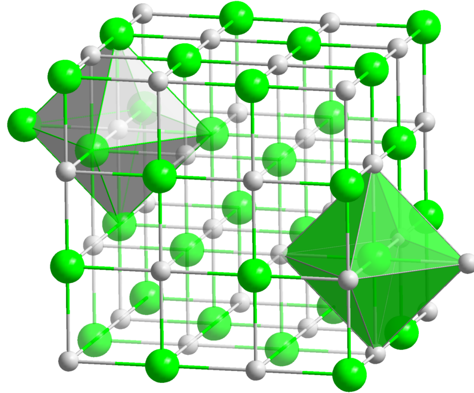

Figure 1.14: Lithium fluoride crystal lattice structure.

Lithium fluoride has a rocksalt crystal structure, which consists of two interpenetrating fcc lattices, one for Li^+ ions and one for F^- (Figure 1.14). Its lattice parameter is 4.027 Å [41] and the unit cell can be modelled with two atoms: one chemical species in (0,0,0) position and the other at (0.5,0.5,0.5), in terms of lattice units. The point group of the structure is $Fm\bar{3}m$ and the coordination geometry is octahedral. Each atom is surrounded by nearest neighbours of the other chemical species at the distance of half the lattice parameter. Atoms of the same type are located along the <110>directions at a distance of 2.848 Å.

The density of lithium fluoride at room temperature is 2.639 g/cm^3. The melting point is 1119 K and the boiling point is 1953 K, at ambient pressure [40],[42]. The band gap is 13.6 eV, which makes the bulk material optically transparent [43].

Lithium fluoride has applications in optical devices that require a transparent material in the visible range and interaction with ultraviolet light. It's used in the thermoluminescent dosimeters to detect gamma rays, beta particles and neutrons [44]. It also constitutes one of the main compounds of the salt mixture used by liquid-fluoride nuclear reactors, for its strong stability at the operation temperatures [45]. A thin film

of lithium fluoride is used in PLEDs (Polymer Light Emitting Diodes) and OLEDs (Organic Light Emitting Diodes) as a decoupling layer, to enhance the electronic injection in such devices, as well as in solar cell industry [46],[47].

Recently, the possibility to grow ultrathin layers of insulating materials has opened a path to a new class of systems with tunable properties. Dielectrics in miniaturized electronic devices, magnetic devices based on oxide nanostructures, plasma display panels and magnetic tunnel junctions are just an example [48].

It has been demonstrated by Wäckerlin et al. [10] that by introducing an insulating decoupling layer between a metallic substrate and single molecule magnets (SMM), the magnetic remanence of devices based on SMMs is greatly enhanced. In particular, an epitaxial growth of magnesium oxide (MgO) on the (100) surface of silver (Ag) allowed Wäckerlin et al. to see a giant opening of the hysteresis loop of $TbPc_2$ double-deckers SMM.

In search of a valid alternative to MgO as the insulating layer, different compounds were considered. Lithium fluoride was finally chosen as best candidate for epitaxial growth on the silver (100) surface. The main reasons are its large band gap, the cubic symmetry and the lattice parameters close to that of the Ag(100) surface, which are promising for a heterogeneous epitaxial deposition. The understanding of the type of growth of this material will, indeed, bring more insight on its physical properties and the possibility to use this compound as a decoupling layer for SMM devices,as wellas other technologies. In order to understand that, several different techniques are used, which are explained in next chapter.

Experimental Techniques

2.1 X-Ray Absorption Fine Structure and Linear Dichroism

In order to use X-rays as a probe for material analysis, it is important to have a proper photon source, with technical specifications to ensure that the relevant physical processes can be detected. For certain applications, a lab X-rays source, such as a cathode tube, is employed. However, when a high photon flux and a good spatial and time coherence of the X-ray beam, as well as a good energy resolution is required, a synchrotron radiation is used. This is the case when X-ray absorption fine structure (XAFS) and X-ray natural linear dichroism (XNLD) are employed to study the properties of deposited thin films, as in the present work.

2.1.1 Synchrotron Radiation

Synchrotrons are large scale facilities used to produce highly collimated and coherent X-rays, with a high brilliance and the possibility to use linearly and circularly polarized light. Such facilities require a great number of components and machines to work, but the main parts are illustrated in Figure 2.1.

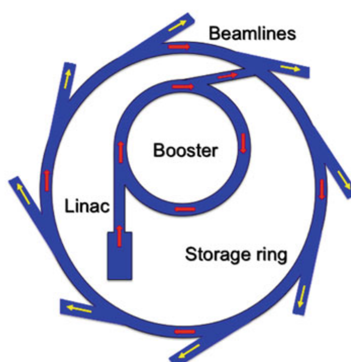

Figure 2.1: Schematic view of a typical synchrotron source facility [49].

A linear accelerator (LINAC) uses high electric field to accelerate and inject high energy electrons into a booster ring, where bunches of electrons are furthermore accelerated, in a ring-shaped vacuum tube, to a suitable energy. The energy is given according to the speed of the particles and the radius of the ring, which ranges from tens of meters to over one hundred. When the bunch of electrons reaches a threshold energy, which is close to the speed of light, it is kicked in the storage ring, where the electron energy and speed, as well as the spatial displacement between different bunches, is kept constant by resonant-frequency cavities (RFC). The circular path in both the booster and the storage rings is controlled by bending dipolar magnets, while the spatial confinement is achieved by quadrupole and sextuple magnets, placed along the electron's path.

The production of X-rays occurs through special devices placed along the storage ring. The emission of high energy photons occurs when electron bunches pass through a dipolar magnet. Due to the Lorentz force, the electrons bend their trajectory and lose energy through the emission of photons, according to the electron dipole radiation in the relativistic regime [49]. The light is emitted in a narrow cone tangent to the curved path followed by the electrons. This shape originates from the natural collimation of the radiation emitted by electrons travelling close to the speed of light, and the angular aperture depends on this speed through the relativistic Lorentz factor γ. The emitted light is collimated by slabs on the "horizontal" plane, the one that hosts the electron trajectory, while on the perpendicular "vertical" plane the collimation is the natural one.

The most common device that produces synchrotron radiation is the bending magnet, that can emit a wide range energy spectrum (Figure 2.2), with the photon flux intensity peak in the X-rays range.

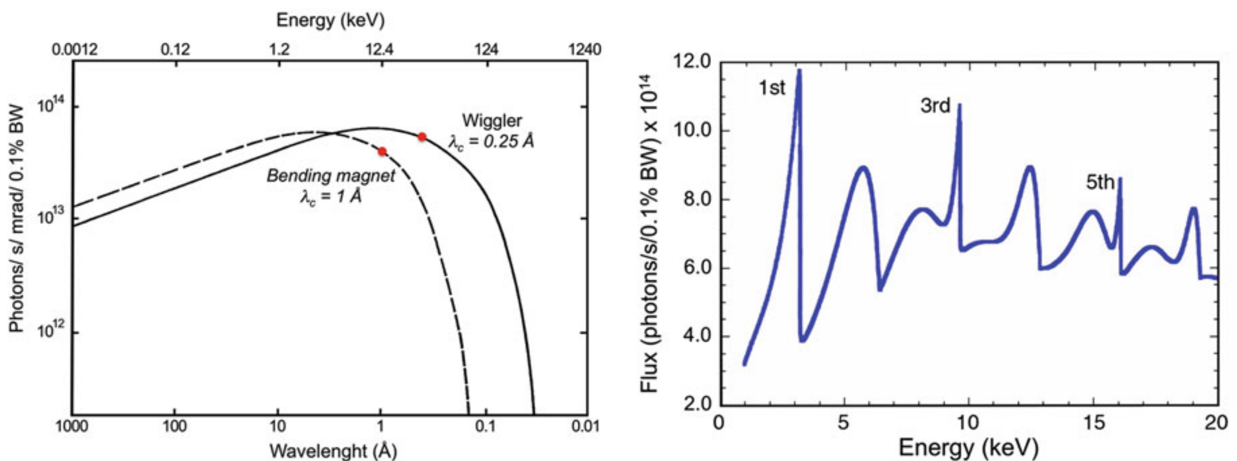

Figure 2.2: (left) Emitted photon flux of a typical wiggler and a bending magnet at the same magnetic field, where λ_C expresses the cut-off wavelength; (right) the emission flux of an undulator, with marked the peaks of harmonics for a given value K [49].

Devices based on arrays of alternating magnets are called "insertion devices" and are employed both to enhance the photon flux and to generate polarized X-rays, achieved by shifting the arrays of magnets along the electron trajectory. The two most common insertion devices are the wigglers and the undulators.

The wiggler is used to achieve a higher energy peak maximum due to a higher magnetic field, which also extends the spectral range of the storage ring toward higher energies by shifting the cut-off wavelength λ_C toward lower values. The emitted spectrum is the result of an incoherent sum of the radiation emitted by each magnetic pole of the array (Figure 2.2). This insertion device resembles the same characteristics of a bending magnet of the same magnetic field but with the emission intensity multiplied by N, the number of the magnetic poles in the device.

The undulator emission is based on a constructive interference of radiation emitted by electrons at different positions of the sinusoidal trajectory, that the particles follow in a multipole array of magnets. The interference occurs for a well-defined phase shift, which depends on the magnetic field and the geometry of the magnetic array. The emission spectrum along the axis of the undulator is a combination of the fundamental wavelength, due to electron oscillation length, and the higher order odd harmonics (Figure 2.2). The intensity of the signal emitted by the undulator is proportional to the square of the number of poles N^2.

The emitted broad-energy X-ray distribution is focused on straight paths, called beamlines, where it is possible to select a narrow window $\Delta\lambda$ around a single wavelength of the incoming beam with a monochromator. When the incoming beam is in the low soft X-ray range, optical gratings are used as monochromators, and the constructive interference is given by the path difference of the reflected light according to the Bragg's law. Monochromatic light is then focused with special mirrors onto the measuring chamber, where the so-called "end station" is located. End stations are usually equipped with different detectors, depending on the studied physical process.

2.1.2 X-Treme beamline at SLS

The Swiss Light Source (SLS) is a 3rd-generation synchrotron with an energy of 2.4 GeV and a storage ring of 288 m circumference. The booster is located in the same tunnel of the storage ring, which facilitates the periodical transfer of electrons from one ring to the other. The 12 straight sections host undulator magnets, which generate ultraviolet and X-ray light of high brightness. Three dipole magnets are optimized to produce hard X-rays. The SLS hosts 18 beamlines, 16 of which are in user operation (Figure 2.3).

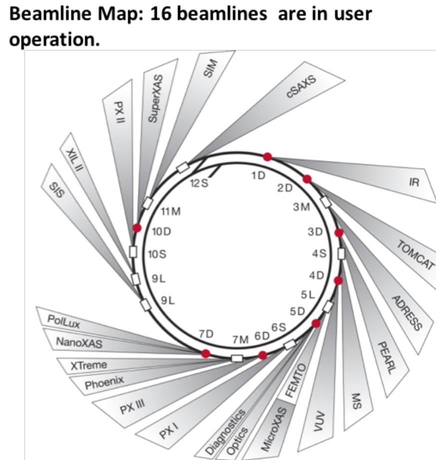

Figure 2.3: Schematic refiguration of insertion devices and beamlines at the Swiss Light Source. Red dots are Bending magnets while white rectangles are insertion devices [50].

X-Treme is one of the soft X-ray beamlines dedicated to the polarization-dependent X-ray absorption spectroscopy at low temperature and high magnetic fields. The possibility to change the polarization of the incoming photons allows the use of techniques like X-ray magnetic circular dichroism (XMCD), X-ray magnetic linear dichroism (XMLD) and X-ray natural linear dichroism (XNLD) [51].

The beamline is located in the straight section 7M of the SLS storage ring. The source is an Apple II undulator with 54 mm period of the magnetic array, for a total length of 1.7 meters. The polarization can be set to circular left/right and linear, from 0° (linear horizontal) to 90° (linear vertical). This can be done by shifting the array of magnets as illustrated in Figure 2.4.

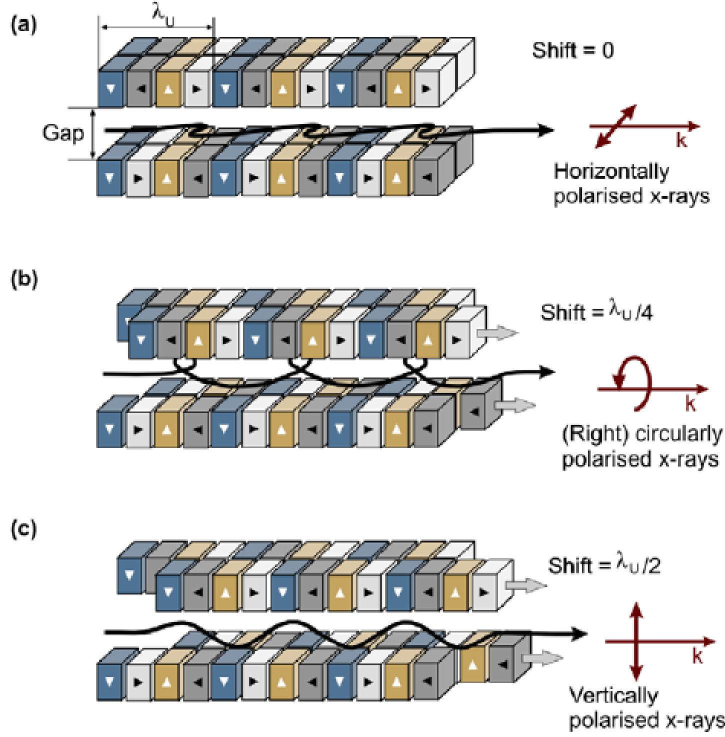

Figure 2.4: Generation of polarized light by Apple II undulator [52].

The degree of the circular polarization is expressed by the ratio K_X/K_Y where the parameter K is defined in terms of the undulator magnetic field B and the undulator period λ_u in centimeters:

$$K = 0.934B\lambda_u \tag{2.1}$$

where $K^2 = K_X^2 + K_Y^2$. In the first harmonic the ratio gives 1, which makes it 100% circularly polarized. However, a maximum energy of 1 keV is achievable by the first harmonic and higher energies require higher harmonics. The X-Treme beamline uses the range from 400 eV to 1800 eV of the undulator spectrum.

After the undulator, by changing the aperture of the moving blades of the front end, it is possible to select the angular acceptance of the cone-shaped emission of the insertion device. A toroidal collimating mirror is then used to focus the beam both vertically and horizontally on the monochromator. The monochromator is based on a plane-grating design (PGM), with a fix-focus constant (C_{ff}) kept independent from the energy. The C_{ff} is given by:

$$C_{ff} = \frac{cos\beta}{cos\alpha} \tag{2.2}$$

where the angles α and β are expressed in the Figure 2.5.

These two angles can conveniently be expressed as function of the deflection angle θ, which simplifies the grating equation to:

$$\frac{m\lambda}{d} = \sin(\theta + \beta)cos\theta \tag{2.3}$$

Where $m\lambda$ is the mth harmonic of λ wavelength and d is the grating distance. By controlling the C_{ff}, the monochromator can be optimized for flux, energy resolution and harmonic rejection [53].

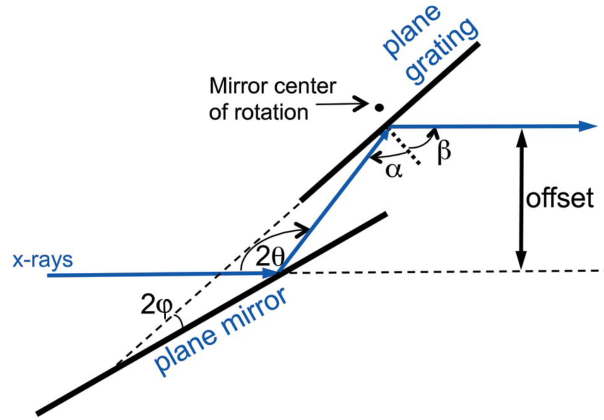

Figure 2.5: Scheme of the plane-grating monochromator, with the relevant angles that controls the energy selection [51].

After the monochromator, a focusing and a refocusing mirrors are used to enhance the spot size down to a FWHM of 220 μm on the horizontal direction, while the vertical size can be controlled by the exit slit size. It is possible to retract the refocusing mirror to change from a focused to a defocused beam, as some samples could be sensitive to radiation damage. The defocused beam has a reduced photon flux density impinging the sample, with a spot size of 490 μm FWHM horizontally and 1.3 mm FWHM vertically for a $C_{ff} = 5$. By changing the C_{ff} it is possible to control the vertical spot size.

The energy resolution of the beamline depends on the energy range and the machine parameters like the C_{ff} and the exit slit. The FWHM evaluated at $\sim$860 eV photon energy, a C_{ff} of 5 and an exit slit of 10 μm, is $\Delta E = 90$ meV. A maximum photon flux registered on the sample is 4.7×10^{12} photons s^{-1}. The intensity of the incoming beam is monitored by a gold mesh positioned between the exit slit and the refocusing mirror.

The end station is the chamber where the sample is located, along with the cryostat, the magnets and the detectors. A schematic view is presented in Figure 2.6. The biggest component of the end station is the ^{4}He cryostat, which allows to reach temperatures as low as 2 K. The required temperature is stabilized by controlling the helium flow and a heater next to the sample. The liquid nitrogen bath surrounding the vacuum chamber

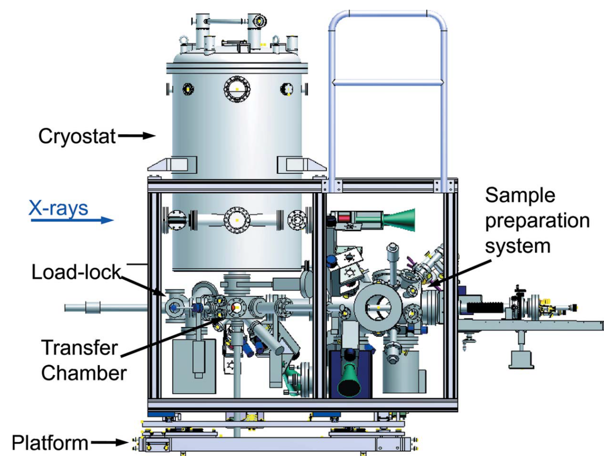

Figure 2.6: Schematic view of the X-Treme beamline end station [51].

works well as infrared radiation shield, in order to achieve and keep the temperature as low as possible.

The sole openings are 6 ports, which are used to transfer the sample, move in/out an additional detector and let the X-rays in. One of the ports has a sapphire window, for an optical visualization of the sample.

The cryostat houses two split-coil pairs of NbTi superconducting wires, which generate the magnetic field at the sample position. One pair of coils generate a field up to 7 T along the direction of the beam, while the other pair generates up to 2 T on the horizontal direction, perpendicular to the beam. The field is homogeneous within 1% on a radial extension of 10 mm from the center of the sample. When the magnets are cooled with liquid helium, a pressure of low 10^{-11} mbar range can be achieved in the experimental chamber.

The samples are loaded in the measurement chamber through a load lock and a transfer chamber, where they are outgassed to the UHV pressure. Once the sample is transferred in the cryostat, it is possible to control its position remotely. The sample is connected to a current amplifier through the SMA (SubMiniature version A) feedthrough, which allows to measure the total-electron-yield current. Transmission and fluorescence measurements are also possible.

The end station is equipped with an in-situ sample preparation chamber, which allows to grow and characterize samples without breaking the vacuum. The preparation chamber has different ports designed to host detachable atomic and molecular evaporators. It implements an ion sputter gun, a low energy electron diffraction instrument, a heating/cooling stage where the sample temperature can be controlled in a range from 30 K to 1800 K and a variable-temperature scanning tunnelling microscope [51]. The chamber is kept in UHV regime by two Turbo pumps, supported by a non-evaporable getter pump (NEG) and a titanium sublimation pump (TSP) [54] [21].

2.1.3 Polarization Dependent X-Ray Absorption Spectroscopy

X-ray absorption fine structure (XAFS) is based on the absorption of X-rays by a sample, which is used to study the physical properties of matter. When a photon flux Φ_0 passes through a material of thickness x, it is reduced according the Lambert-Beer law [49]:

$$\Phi = \Phi_0 exp(-\mu(\omega)x) \tag{2.4}$$

where Φ is the final flux and $\mu(\omega)$ the total linear attenuation coefficient, which depends on the photon energy $\hbar\omega$ and the composition of the sample. The attenuation coefficient decreases with increasing photon energy, as it is proportional to the probability of the interaction of X-rays with the material. Such probability is expressed by the atomic cross section and is different for each chemical element.

As the attenuation factor depends on both the absorption and the scattering of the incoming flux, three different cross sections are usually reported as functions of the interacting photon energy, for each element. These are the photoelectric absorption, the elastic and the inelastic cross sections, reported in Figure 2.7.

The behaviour of the absorption cross section shows discontinuities in correspondence of the absorption edges, which occurs at specific energies, characteristic of the specific absorption edge and chemical element. These edges reflect a higher rate of electron transitions, which happen when a photon of sufficiently high energy is absorbed by deep level (core) electrons and promoted in an unoccupied bound level.

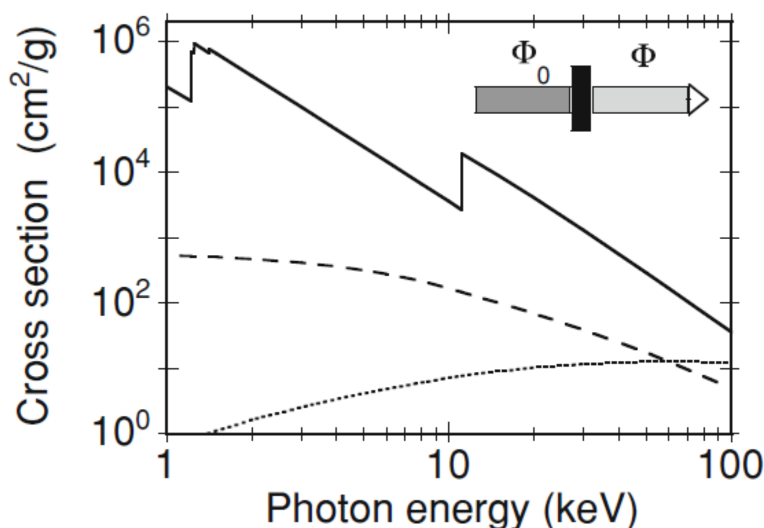

Figure 2.7: X-ray absorption cross section for germanium. Solid line represents the photoelectric absorption, dashed line the elastic (Thomson) scattering, dotted line the inelastic (Compton) scattering [49].

If the absorbed photon energy is sufficiently high, an electron can be ejected from the atom, ionizing it (photelectric absorption). As X-rays match the binding energies of core electrons, the electronic transitions occur from the innermost atomic levels, which are labelled with the letters as in Table 2.1.

Edge:	M_V	M_{IV}	M_{III}	M_{II}	M_I	L_{III}	L_{II}	L_I	K
Core level:	$3d_{5/2}$	$3d_{3/2}$	$3p_{3/2}$	$3p_{1/2}$	3s	$2p_{3/2}$	$2p_{1/2}$	2s	1s

Table 2.1: Principal X-rays absorption edges and corresponding core level electron orbitals.

In the energy range up to 40 keV the photoelectric absorption is the dominant process and, in most cases, it is possible to approximate the total attenuation coefficient μ with the photo-electric absorption coefficient.

The absorption edges are element sensitive and display an X-ray absorption fine structure (XAFS) which is the complex structure that arises around the absorption edge and comes from the geometric and chemical structure surrounding the absorbing atom. At the photoelectric absorption edge, the coefficient μ can be expressed in terms of the absorption cross section $\sigma_A(\hbar\omega)$ and the density of the absorbing atoms n:

$$\mu(\omega) = n\sigma_A(\hbar\omega) = \left(\frac{2\hbar}{\epsilon_0 \omega A_0^2 c}\right) n \sum_f w_{fi} \tag{2.5}$$

The term in the rightmost parenthesis is the inverse of the incoming photon flux, where A_0 is the magnitude of the vector potential of the electromagnetic field, ϵ_0 is the vacuum permittivity and c the speed of light. The term w_{fi} expresses the probability of the transition per unit time of an atom from its initial ground (unperturbed) state $|\Psi_i\rangle$ to the final excited state $|\Psi_f\rangle$, after a core electron has been excited to the continuum of free states. According to the Fermi Golden Rule, this transition occurs only if the absorbed photon energy matches the energy difference between the ground and the excited states.

From the time-dependent perturbation theory, the transition rate can be expressed in terms of the matrix elements between the two states, which depend on the interaction Hamiltonian, and can be written as:

$$w_{fi} = \left(\frac{\pi e^2 A_0^2}{2\hbar m^2}\right) < \Psi_f | \sum_j e^{i\mathbf{k}\cdot\mathbf{r}_j} \mathbf{p}_j \cdot \hat{\eta} | \Psi_i > \tag{2.6}$$

where e and m are the electron charge and mass, $\mathbf{p}_j$ the momentum operator of the j-th electron, $\hat{\eta}$ and $\mathbf{k}$ are the polarization vector and the wavevector of the electromagnetic field, and $\rho(E_f)$ the density of the final continuum states, where $E_f = E_i + \hbar\omega$.

The previous expression (2.6) can be further simplified by several approximations:

- The one-electron approximation assumes that only the absorbing core-electron and the final states are relevant in the process, while the other N - 1 electrons simply relax their orbitals around the core hole. This splits the attenuation factor in two contributions $\mu(\omega) = \mu_{el}(\omega) + \mu_{inel}(\omega)$, where the elastic signal represents the transitions fulfilling this approximation, while the inelastic combines the effects involving the other electrons of the same atom.

- The electric dipole approximation allows to expand the exponential term in (2.6) and truncate it at the first term when the radiation wavelength is much larger than the system size. Within the one- electron approximation, this statement holds, as the photon interacts only with the core electron level.

- The sudden approximation assumes that the emitted photoelectron does not interact with other electrons of the same atom, which allows to extract the atomic wavefunctions of all the other states in a single factor $S_0^2 = |\left\langle \Psi_f^{N-1} \middle| \Psi_i^{N-1} \right\rangle|^2$ This term expresses the superposition integral and it is usually in the range of 0.7 - 0.9 [49].

The elastic attenuation coefficient can thus be rewritten as:

$$\mu_{el}(\omega) = n\left(\frac{\pi e^2 \omega}{\epsilon_0 c}\right) < \Psi_f | \hat{\eta} \cdot \mathbf{r} | \Psi_i > S_0^2 \rho(\epsilon_f) \tag{2.7}$$

In which Ψ, r and ϵ_f are the wavefunction, the vector position and the final energy of the single electron involved in the process. For $S_0^2 = 1$ the total linear attenuation factor $\mu(\omega)$ coincides with the elastic attenuation factor $\mu_{el}(\omega)$. Within those approximation are always valid the angular selection rules [49].

The penetration depth of X-rays can be determined through the attenuation factor. For soft X-rays, the drop of the photon flux of a factor $1/e$ happens in the region of the sampled material from few nm to several μm, with the penetration depth increasing as the photon energy increases.

Different detection modes are used to measure the XAFS spectra of a sample, one of which is the total electron yield (TEY) [49]. The escape depth of photoelectrons is on the order of 5-50 Å (Figure 2.8), which makes the total electron-yield detection mode with soft X-rays strongly surface sensitive with respect to the other techniques. In case of thin films, the detected current as function of the incoming X-rays energy is proportional to the absorption coefficient.

In the equation (2.7) it is evident that the polarization $\hat{\eta}$ of the interacting electromagnetic wave greatly affects the absorption rate. If the absorption of a sample changes by changing the polarization of the incoming wave, the material is called dichroic. This feature can be used to investigate the magnetic properties as well as the symmetry of the system, but in the present work the focus will be given to the latter.

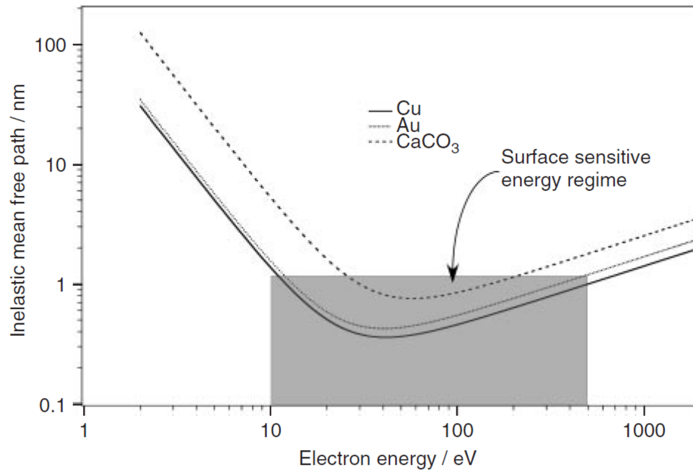

Figure 2.8: The shape of the universal curve of electron mean free path in solid matter, for Cu, Au and $CaCO_3$ [15].

If linearly polarized X-rays are employed, the measured intensity could depend on the orientation of the sample with respect to the incoming photon flux. This effect is known as X-ray Natural Linear Dichroism (XNLD) and it originates from a non-spherosymmetric charge distribution of the excited atoms when the surrounding environment (ligand field) displays a low symmetry. When the linearly polarized vector **E** is aligned along an empty orbital it gives the maximum absorption, so by changing the angle of the incoming light it is possible to probe the anisotropy of the orbital symmetry.

XNLD has a broad application in intrinsically low symmetry systems like 2D interfaces and monolayer surfaces. In those systems, the anisotropy of the empty states is measured by consecutive measurements on a sample kept with its surface plane at a grazing angle. According to the geometry of the experimental setup, the in-plane orbitals are probed by one of the two polarizations (eg. vertical) and a component of the out-of-plane orbitals by the polarization perpendicular to the previous one (eg. horizontal).

The XNLD spectra are displayed as the difference between the two polarization dependent XAFS. The intensity I_{XNLD} is given as:

$$I_{XNLD} = I(\sigma_v) - I(\sigma_h) \tag{2.8}$$

of which σ_v and σ_h are the vertical and horizontal polarization vectors of the electric field.

A detailed quantitative analysis of the XNLD spectra require advanced simulations of the lattice geometry and the ligand field. However, a qualitative analysis of the asymmetry of the absorption edge is always possible, especially when combined with other characterization techniques.

2.2 Scanning Tunneling Microscopy

2.2.1 STM principles

The general principle of work of the scanning tunneling microscopy (STM) is based on the sampling of the local density of states (LDOS) of the biased sample surface through the detection of a tunnelling current by a small grounded tip of the STM microscope.

The core of the device is the metallic tip, usually made of Tungsten or a Pt-Ir alloy, which is moved across the surface of the sample by piezo-drive motors. As shown in the Figure 2.9, the motors are three mutually perpendicular piezoelectric transducers, that expand or contract when a proper voltage is applied to them. The X and Y piezo motors are used to move the tip along equally spaced parallel lines across the surface plane, while the Z piezo is used to detect the current by moving the tip perpendicularly to the surface.

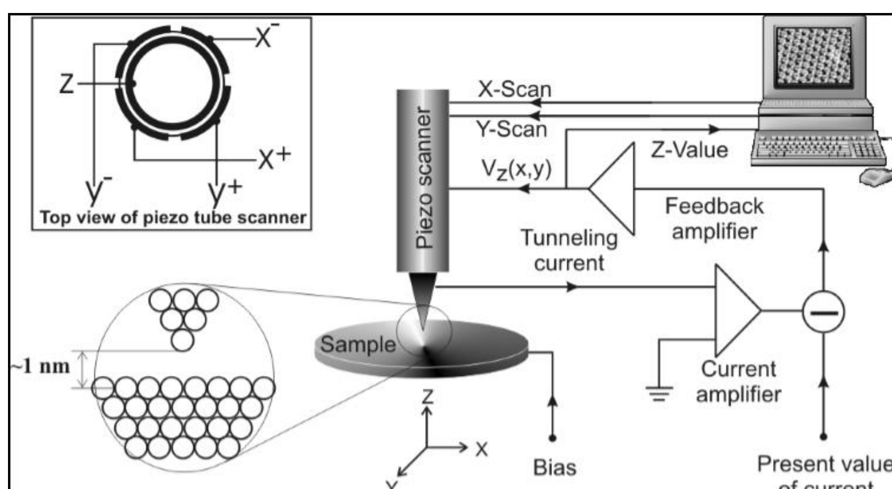

Figure 2.9: A schematic representation of the working principle of a scanning tunnel microscope [55].

When the electron wavefunction of the tip overlaps with that of the surface, a finite tunnelling conductance is generated, which gives rise to a tunnelling current when a bias voltage between the tip and the sample is applied. By setting a current set-point value $I - set$, the feedback system of the microscope is able to control the Z piezo and move the tip closer/further to/from the surface in order to match the set-point value. The variation between the measured current and the set-point value is thus proportional to the displacement z of the tip, which is recorded by the device. By detecting the variation of the z position over the xy plane, the surface local density of state is mapped. The variation of LDOS is recorded in form of gray-scale colour image. The lateral size of the STM images usually ranges from some tens of nanometers to tens of micrometers.

From a quantum-mechanical point of view, the tunnelling current can occur only when electrons have empty states to fill. It can be demonstrated [56] that the measured tunnelling current $I(z)$ has an exponential behaviour with the distance z between the electrodes and depends on the applied voltage through the tunnelling conductance $G = \frac{I(z)}{V}$. The Bardeen model [56] relates the conductance G to the electron density of states of the sample (ρ_S) and the tip (ρ_T) through the formula:

$$G = 2\pi^2 G_0 |M_{\mu\nu}|^2 \rho_S(E_F)\rho_T(E_F) \tag{2.9}$$

in which $G_0 = \frac{2e^2}{h} \approx 77.48\mu S$ is the conductance quantum and $M_{\mu\nu}$ the tunnelling matrix element, which expresses the tunnel probability. The formula (2.9) holds only if the bias voltage applied to the sample does not shift the electron energy levels E_n of the sample too far from the fermi level E_F with respect to the vacuum level [56].

The detected current is compared with a reference value chosen through the computer interface. In a standard tunnel microscope, for voltages up to 10 V a current up to $\sim 1\mu$A region can be used. The difference $\Delta I = I_{ref} - |I_{sign}|$ between the reference and the signal values is used as the input of a feedback loop which drives the Z piezo. When ΔI is positive, the voltage applied to the Z piezo brings the tip close to the sample, and vice versa. In such way, an equilibrium z position is kept as long as the surface tunnelling current does not change. By a general convention, the voltage V is applied to the sample, so when $V > 0$ the electrons tunnel from the occupied states of the tip to the empty states of the sample (for negative voltages the process is reversed).

By assuming the LDOS of the tip constant, it is possible to measure the LDOS of the sample by keeping constant the x, y and z position and changing the bias voltage potential. The registered current is then proportional to the sample surface state density. This technique is called scanning tunneling spectroscopy (STS) and is widely used to analyse the states close to the Fermi energy by the so-called dI/dV measurement spectra.

In order to achieve well resolved STM images, it is fundamental to isolate the system from vibrations. This could be done by adding vibration damping systems (springs, suspensions, etc.), or by digital frequency filters. The measurements are usually done in UHV regime and at low temperature.

When a metal surface is scanned by a tunnel microscope, the signal is proportional to the projected LDOS of the Fermi level of the sample. The registered variation of the z piezo position is then proportional to the real morphology of the sampled surface. However, if the surface hosts materials with a different density of states and conductivity, it is a hard task to extract real heights from the displacement of the tip. The images then usually present apparent heights and the relative displacement from a reference level value is considered.

2.2.2 Omicron VT-STM

The X-Treme beamline at the Swiss Light Source is equipped with a dedicated UHV chamber with a scanning probe microscope Scienta Omicron VT-SPM 50/500, which allows to use both the scanning tunneling microscope (STM) and the atomic force microscope (AFM) modes (Figure 2.10).

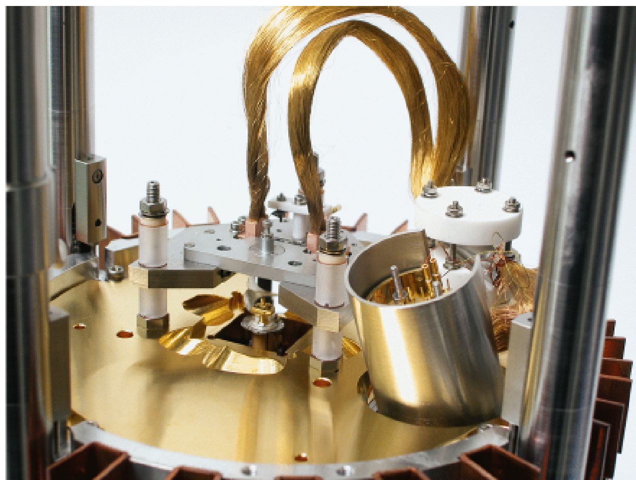

Figure 2.10: Omicron VT-SPM 50/500 [57].

The device is equipped with a heating filament at the sample stage and a removable attachment for the liquid nitrogen/helium cooling (Figure 2.11). This allows to control the sample temperature in the region from 50 K to 500 K with a good stability of the tip. The omicron sample stage is designed to easily change the sensors in-situ, by attaching/detaching the sensor from the tip stage through magnetic contacts.

The STM sensor is based on a sharp tungsten tip, which allows current measurements from 1 pA to 330 nA by the IVC H3 pre-amplifier, designed to provide a signal-to-noise ratio close to the theoretical minimum. The bias voltage of up to ± 10 V can be applied to the sample, while the tip is virtually grounded. The feedback loop of the vertical z sensor and the sampling speed can be controlled manually, for an optimal imaging setup.

The tip approach is done remotely by setting the sample bias voltage and the current set-point. In the scanning mode, the piezo motors allow to sample variable-size areas in a contour of 10 μm x 10 μm, while the vertical extension range is 1.5 μm. The whole scanner is mounted on a floating suspension system with an integrate eddy current damping, which ensures vibration isolation. Several windows allow to control the navigation of the sample inside the chamber, which is done remotely on the SPM stage and manually with a wobble stick to the other UHV components.

The chamber is connected to the preparation chamber through a gate valve. A NEG pump is connected to the chamber and ensures a stable pressure of low 10^{-10} mbar. The

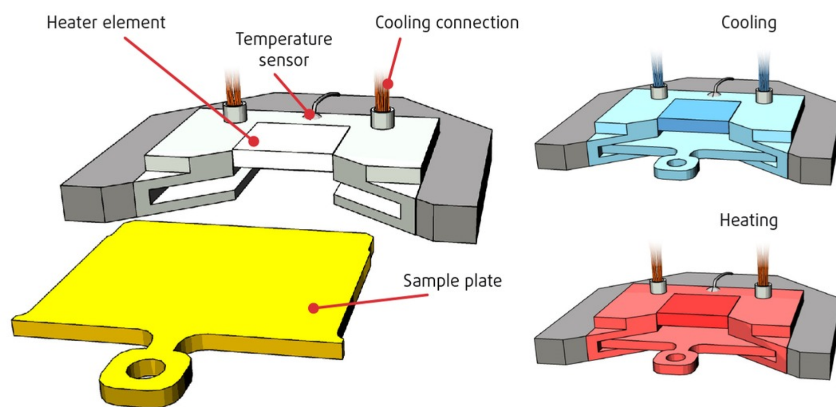

Figure 2.11: The VT-SPM sample stage with the heating/cooling system. The samples are loaded facing downward on a Omicron sample plate [57].

remote control and the signal collection are done by the MATRIX program, which also allows to keep track of the signal in real time. The program allows to switch between the AFM, STM and STS modes, which makes the Omicron VT-SPM a powerful all-in-one scanner.

2.3 Low Energy Electron Diffraction

2.3.1 LEED principles

The low energy electron diffraction (LEED) is a technique used to sample the lattice structure of a surface in UHV conditions. An electron gun is used to accelerate electrons toward the sample surface, where they can interact through different processes, depending on the energy of the incoming electrons. Low energy electrons, in the range between roughly 20 and 500 eV, interact strongly with the matter via elastic scattering and a LEED measurement detects the elastically scattered electrons from a few atomic layers of the sample surface (see Figure 2.8).

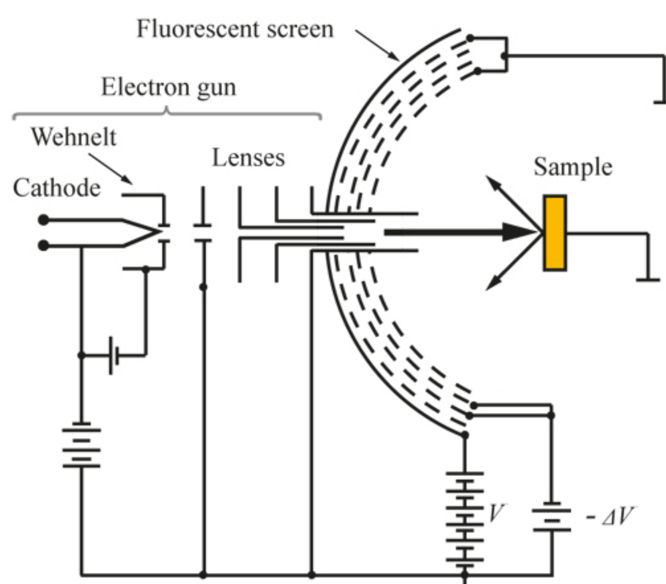

Figure 2.12: The schematic view of a LEED device [58].

A typical LEED device is illustrated in Figure 2.12. A high voltage cathode emits electrons with a specific energy toward a grounded sample. The Wehnelt potential is used to control the magnitude of the beam as it allows to tune the energy bandwidth of the electron current. The lenses are used to properly focus the beam on the sample. The impinging beam is backscattered by the surface and electrons are detected by hemispherical concentred grids designed to screen out the inelastically scattered electrons. This is done by the application of a retarding field after which a suppressor removes the electrons with an energy higher or lower than the required by elastic scattering. Then, the electrons are accelerated toward a fluorescent screen held at a high voltage and the pattern is recorded by an external camera.

The kinematic scattering theory assumes that the scattering process occurs only once for each incoming electron. The elastic scattering process can thus be understood by simple geometric considerations of the lattice structure of a crystalline material.

The lattice of a three-dimensional crystal can be modelled through a unit cell, identified by three primitive lattice vectors $\vec{a_1}, \vec{a_2}$ and $\vec{a_3}$. By choosing three integer numbers n_1, n_2 and n_3, a linear combination of the primitive lattice vectors gives a "direct lattice" vector $\vec{R} = n_1\vec{a_1} + n_2\vec{a_2} + n_3\vec{a_3}$, pointing at any lattice point. Similarly, it is possible to define a reciprocal lattice, whose primitive lattice vectors $\vec{b_1}, \vec{b_2}$ and $\vec{b_3}$ are related to the crystal lattice by the following relations:

$$\vec{b_1} = 2\pi\frac{\vec{a_2} \times \vec{a_3}}{\vec{a_1} \cdot (\vec{a_2} \times \vec{a_3})}, \vec{b_2} = 2\pi\frac{\vec{a_3} \times \vec{a_1}}{\vec{a_1} \cdot (\vec{a_2} \times \vec{a_3})}, \vec{b_3} = 2\pi\frac{\vec{a_1} \times \vec{a_2}}{\vec{a_1} \cdot (\vec{a_2} \times \vec{a_3})} \tag{2.10}$$

Any vector of a reciprocal lattice can be expressed as $\vec{K} = h\vec{b_1} + k\vec{b_2} + \ell\vec{b_3}$ with h, k and ℓ three integer numbers.

When a low energy electron is elastically scattered by a surface, a wavevector $\vec{q} = \vec{k_f} - \vec{k_i}$ is exchanged in the process, where $\vec{k_i}$ and $\vec{k_f}$ are the incoming and the scattered electron wavevectors. It can be shown [49] that a constructive interference of the scattered electrons occurs when $\vec{q} = \vec{K}$, which gives rise to a diffraction peak. In other terms, the diffraction happens when two parallel crystal planes at a distance $d_{hk\ell}$ elastically scatter incoming low-energy electrons at the same angle, according to Bragg's law (Figure 2.13):

$$m\lambda = d_{hk\ell} sin\theta \tag{2.11}$$

where the angle θ is the diffraction angle, λ is the De Broglie wavelength of the electrons and m an integer number representing the diffraction order, which originates from the geometrical path difference of the incoming plane wave between the parallel planes $hk\ell$.

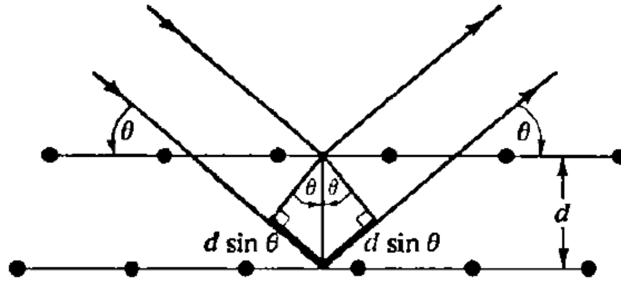

Figure 2.13: Geometrical construction of Bragg's law [59].

As electrons, with a fixed energy, could match the diffraction conditions for different lattice planes, each set of planes give arise to a diffraction "Bragg" peak. For homogeneous samples with long range order, Bragg peaks appear as sharp intensity points on the LEED diffraction pattern. The position of the peaks can also be understood through the Ewald construction.

By removing one dimension from the reciprocal lattice, the three-dimensional array of points becomes an array of rods perpendicular to the sample surface. Assuming an electron beam with a fixed energy, which corresponds to an electron wavevector $\vec{k_i}$ in the reciprocal lattice, it is possible to draw a sphere with a radius k_i centered on an arbitrary rod in the momentum space. The incoming wavevector is assumed to lie along this rod, which is denoted as the origin rod (0,0) (Figure 2.14). The intersection of the Ewald sphere with the rods gives the angles of the Bragg peak conditions.

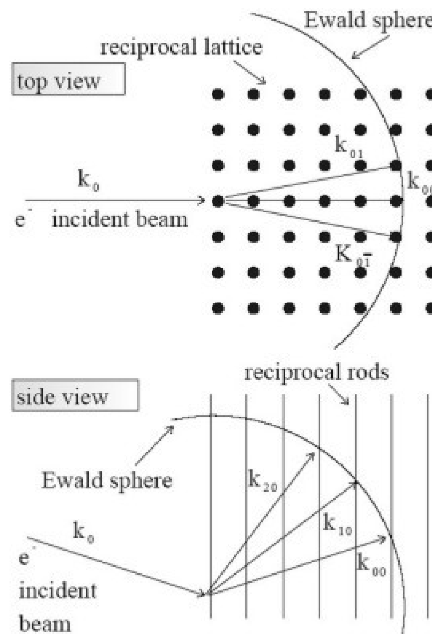

Figure 2.14: Construction of the Ewald sphere for LEED [60].

The detector of the LEED is designed to recover the positions of the peaks inside a solid angle acceptance. Therefore, the detected diffraction pattern, as the one in Figure 2.15, is a picture of the two-dimensional reciprocal lattice of the probed surface, with the spots labelled by Miller indexes (h, k) of the diffraction plane. By changing the energy of the incoming electrons, the radius of the sphere changes, allowing to probe a variable portion of the reciprocal space.

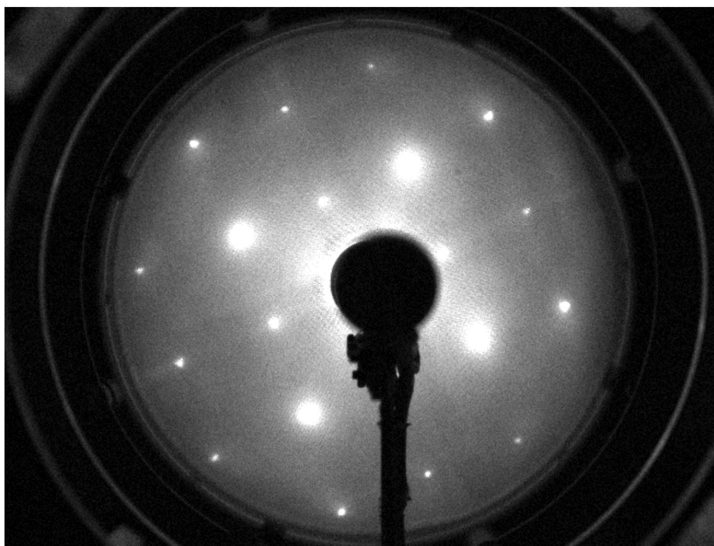

Figure 2.15: LEED pattern of an Ag(100) surface at 140 eV electron energy, taken at X-Treme beamline.

The analysis of the diffraction patterns is possible by comparing the acquired patterns with the reference patterns and estimating the geometry of the lattice based on the point-group symmetry theory. From the shape of the diffraction pattern the periodicity of the surface can be recovered, but the information on the arrangement of atoms in the unit cell, as well as their chemical nature, is hidden in the intensities of the Bragg peaks.

The intensity of a diffracted spot depends on the structure factor term $F_{hk\ell} = \sum_f f_j e^{i\mathbf{k}_{hk\ell}\cdot\mathbf{r}}$, which takes into account the positions of each atom in the unit cell and the magnitude of the electron interaction with a given atom through the atomic factor f_j. Atomic factors of all the atoms in the crystal unit cell are summed, which can give arise to a null value of the structure factor for certain diffraction spots. This effect is known as the "systematic absence" of the peak diffraction and could be seen as "missing" intensity spots of specific Bragg peaks. However, as electrons interact strongly with the matter via multiple scattering, a detailed analysis of the LEED intensities is complicated and often done with the support of simulations.

The width of the spots can also be relevant when evaluating the LEED pattern, as diffraction coming from small real-space structures (eg. nanoparticles) would broad the signal in the reciprocal space. Because electrons are charged particles, it is more suitable to analyse metallic surfaces, as insulators could give arise to charging problems. For its high surface sensitivity and a fairly simple interpretation of the acquired images, the LEED is widely used in the study of surface science.

2.3.2 ErLEED specifics

The end station of the X-Treme beamline at the Swiss Light Source is equipped with a SPECS ErLEED 150, used to study the diffraction patterns of surfaces in UHV chamber (Figure 2.16).

Figure 2.16: SPECS ErLEED 100/150 [61].

The LEED optics is mounted on a DN 150 CF flange attached to the preparation chamber. On the atmospheric side the LEED flange is equipped with a window, which allows to see the diffraction pattern on the fluorescent screen located on the vacuum side. The screen and the electron gun are mounted on an extendable system of base rings, which allows to minimize the sample-device distance. The electron energy can be varied between 1 and 3000 eV with the ErLEED 3000D power supply. The screen is normally operated at a high voltage of 6 keV.

An integrated shutter allows to isolate the LEED optics from the chamber when annealing, evaporation or sputtering processes occur. The device is controlled remotely by the control panel on the power supply, which allows to select easily the electron beam energy, once the other parameters are set. On the atmosphere side of the window, a GigE digital camera is installed for optical acquisition of the LEED patterns. The camera is mounted on a retractable shielded stage with a rotating frame, optimal for image acquisition of LEED patterns.

2.4 Quartz Microbalance

Quartz crystal microbalance (QMB) is an instrument used to measure the frequency change of quartz crystal resonator when a mass variation occurs on its surface. The shift of the resonant frequency occurs when a small mass is deposited on the crystal, which makes this technique useful to determine the evaporation rate of substances in UHV environments. The measurement is based on the piezoelectric effect of a small quartz crystal under an applied alternating current. The current induces a standing acoustic resonance at high frequency, which variation is easily detectable by electrical means. As the resonance frequency depends on the thickness of the crystal, any variation induced by as low as a fraction of a monolayer can be probed.

In the approximation of low coverage thicknesses, compared to the size of the crystal, the Sauerbrey equation can be used. This requires that the ratio of the frequency shift Δf and the resonance frequency f_0 of the crystal must be such that $\frac{\Delta f}{f_0} < 0.05$. Also, the deposited mass is assumed to be rigid and evenly distributed on the crystal surface. In this case, it is possible to relate the frequency shift Δf to the mass variation Δm as:

$$\Delta f = -\frac{2f_0^2}{A\sqrt{\rho_q \mu_q}}\Delta m \tag{2.12}$$

in which ρ_q is the density of the quartz, μ_q the shear modulus of quartz for AT-cut crystal and A is the effective area between the electrodes, where the deposition occurs. The Sauerbrey model is limited to the conditions stated above, especially the UHV environment as it excludes any damping performed by a surrounding fluid.

The X-Treme beamline (at SLS) is equipped with an Inficon quartz crystal of 6 MHz resonance frequency and a radius of 4 mm of the piezoelectric active area (Figure 2.17).

Figure 2.17: An Inficon 6 MHz quartz crystal mounted on a UHV sensor support [62].

Assuming the density of the deposited film does not change from bulk, it is possible to determine the thickness of the film by inverting the Sauerbrey formula (2.11). This technique is also used to determine the evaporation/sublimation rate of materials

from the effusion cells, by pointing the cell toward the sensor and measuring the frequency shift in Hz/min. However, the evaluation of the rate is not straightforward as the Sauerbrey model assumes a series of approximations, the most important of which is the independence of the deposition from the sticking coefficient.

As stated in Section 1.4, the chemical nature, the deposition temperature and the type of interaction at the interface play a major role in the adsorption rate, which is expressed by the sticking coefficient. Thus, by neglecting this factor it is supposed that all the impinging atoms are adsorbed on the surface, which is not always true. If the substrate for the deposition is changed, the sticking coefficient must be considered for a correct evaluation of the deposited film thickness. Anyway, the QMB technique is a useful tool to estimate and compare the evaporation/sublimation rates of a great variety of materials used in surface science.

Results and Discussion

3.1 Sample Preparation

LiF was deposited on silver via thermal sublimation. LiF powder of 3-6 mm diameter and 99.9% purity from Lesker company was used as source material. Few milligrams of powder were loaded in a Al_2O_3 crucible, which was previously outgassed up to 1550 K. The cell was constantly cooled with water flow through the shroud surrounding the heating filament and a high current power supply (TDK Lambda) provided the necessary power via a PID controller (Eurotherm 2400). The cell was isolated by a vacuum bellow and interfaced to the preparation chamber of the X-Treme beamline (SLS) [51]. It was pumped to a pressure range of 10^{-10} mbar and constantly cooled by water flowing through the pipes connected to the cell shroud. A sketch of the setup is presented in Figure 3.1, where the different components are labelled.

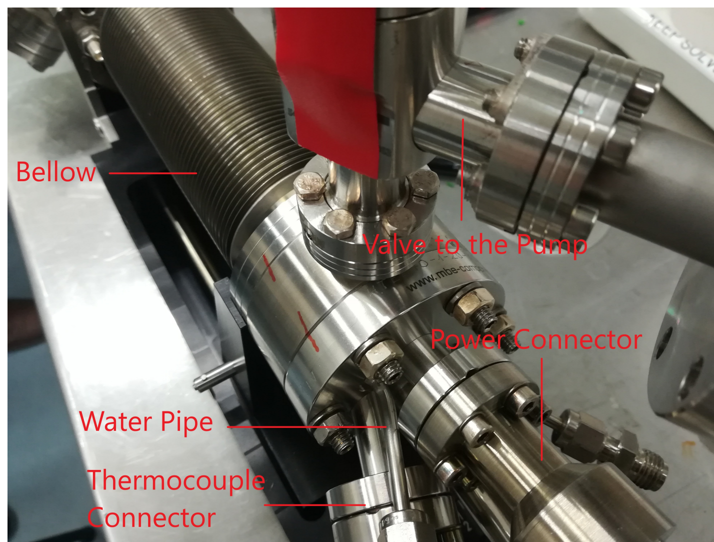

Figure 3.1: MBE Komponenten high-temperature effusion cell, located inside the vacuum below.

The LiF source was outgassed up to 1080 K, with a step rate of several Kelvin per minute, to keep the low-pressure range in the preparation chamber. The evaporation rate of the source was detected via quartz crystal microbalance (QMB) measurements at the same position as the substrate and the results are presented in Figure 3.2.

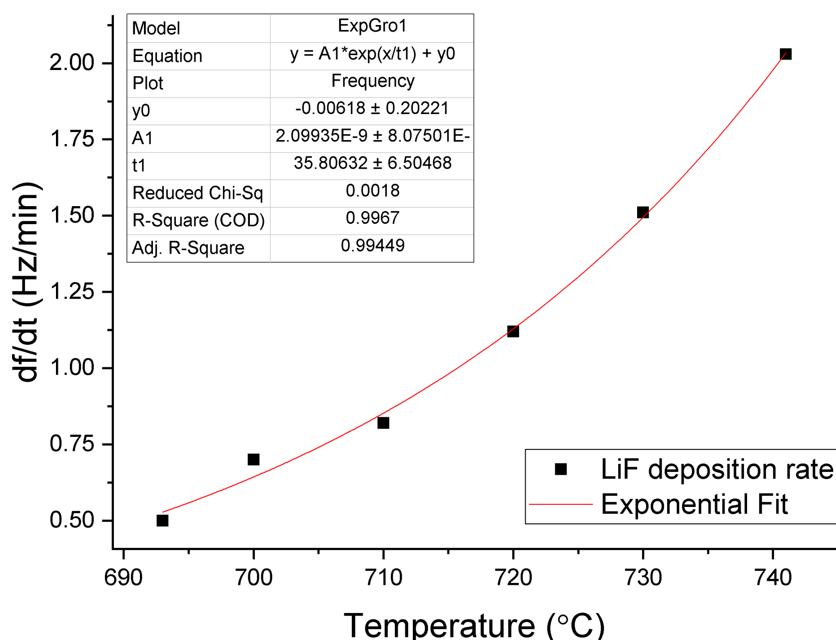

Figure 3.2: LiF evaporation rate detected by Quartz Microbalance measurements.

Even if most experimental works reported a deposition temperature above the LiF melting point [63] [64], Montereali et al. [65] reported crystallite formations at an evaporation temperature of 800°C. The evaporation temperature was then chosen to be 700°C, for its stable low deposition rate measured by the quartz balance reference.

The deposition was done onto a Ag single crystal cylinder of 7 mm diameter and 3 mm thickness, cut along the (100) surface. The crystal was mounted on an Omicron plate and processed in situ with several sputtering and annealing cycles. The sputtering was done with Ar^+ ions at 2 keV and at a pressure of 3×10^{-7} mbar, for an average current of 4 μA, measured at the sample plate, and a duration varying from 90 min for the first cycle to 20 min for the latest. The annealing was done after each sputtering cycle, using an electron beam heater mounted right below the sample stage in the preparation chamber.

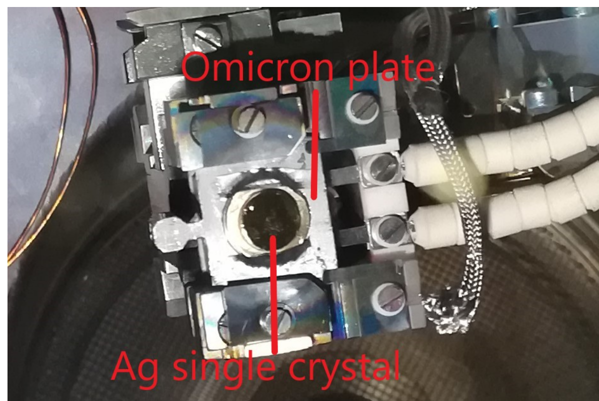

Figure 3.3: Ag single crystal mounted on an Omicron plate and used as substrate for the evaporations in the preparation chamber.

The temperature was optically detected via a pyrometer pointed onto the surface of the crystal through a window of the chamber. As the direct input of the pyrometer detector is the thermal radiation J_T of the sample, a program is used to convert the detected radiation to temperature values T through the Stefan-Boltzmann law $J_T = \varepsilon\sigma T^4$, where σ is the Stefan-Boltzmann constant and ε the emissivity. Emissivity values of common materials are tabulated. For the polished silver crystal substrate $\varepsilon = 0.05$ was used. The average maximum temperature measured was 500°C, with an emission current of 10 mA and 1.2 kV potential, for a total power emission of 12 W. The sputtering and annealing cycles were carried on aiming for the largest possible clean terraces on the Ag(100) surface, which were detected via the VT-STM in the adjacent chamber, without breaking the vacuum.

With the approximations done by the Sauerbrey equation (see Section 2.4), the conversion from frequency variation Δf to the thickness Δt of the sample was obtained. It was evaluated that a shift of $\Delta f = 4.2$ Hz corresponds to $\Delta t = 1.98$Å, which was estimated to be close to a monolayer (ML) of LiF, whose thickness was identified as half of the bulk lattice constant (nominally $a/2 = 2.01$Å).

Several samples were prepared by depositing each time LiF on the surface of the previous one (except for the first deposition), thus obtaining a series of growing thicknesses. Series of samples were repeated for each experimental technique. In some cases, samples of defined thickness were prepared ad hoc, starting with a clean surface, and analyzed in sequence by a combination of STM, XAFS and LEED. The prepared samples are presented in Table 3.1, where the letter represents the estimated thickness, while the number labels the techniques it was studied by ("1"= STM, "2"=STM&XAFS, "3"=XAFS, "4"=STM/LEED,"5"=LEED). The evaporation time represents the cumulated evaporation time for the samples grown in series.

Thickness label	Sample technique label	Evaporation time (minutes)	QMB Δf (Hz)	Estimated Thickness (MLs)
A	A1 (STM); A3 (XAFS); A4 (STM&LEED); A5 (LEED)	1	0.7	∼0.2
B	B1 (STM); B3 (XAFS); B4 (STM&LEED); B5 (LEED)	3	2.1	0.5
C	C1 (STM); C2 (STM&XAFS); B5 (LEED)	6	4.2	1
D	D1 (STM); D3 (XAFS); D5 (LEED)	18	12.6	3
E	E1, E1bis (STM); E3, E3bis (XAFS); E4 (STM&LEED)	36	25.2	6
F	F1 (STM); F3 (XAFS)	72	50.4	12

Table 3.1: Deposited samples labelled according to the technique used (number) and grouped by sample thickness (letter). The evaporation time of samples grown in series represents the cumulated evaporation time.

3.2 LiF XAFS and XNLD

The possibility to prepare in situ samples and easily transfer them to the measuring chamber of the X-Treme beamline, where XAFS measurements can be performed with linearly and circularly polarized light, without breaking the vacuum. This allowed us to measure the sample every time a new deposition was added on the substrate, proceeding to study the evolution of XAFS and XNLD spectra by increasing the amount of LiF on the silver substrate. To detect the fine structure of the fluorine K edge (nominally 696.7 eV), we used an energy range from 675 eV to 750 eV. The signal was detected by the total electron yield (TEY) mode, scans were performed in the "on-the-fly" monochromator and undulator mode. This allowed a fast sampling while sweeping the energy of the incoming photon flux. To prevent the samples from radiation damage a defocused beam was used, with an X-ray spotsize of 0.3 mm horizontally and 1.2 mm vertically, at $C_{ff} = 5$ (see Section 2.1.2). The samples were oriented with the normal of the surface at 60

degrees from the incoming light beam propagation vector. In this configuration, vertically polarized X-rays probe in plane electronic orbitals, while horizontally polarized light interacts mostly with out-of-plane electronic orbitals (see Section 2.1.3). As standard procedure, a magnetic field of 50 mT was applied along the direction of incoming X-rays, to enhance the detected polarization-dependent electronic yield. All the measurements were done at room temperature ($\sim$ 300 K). We started by acquiring the fluorine K-edge of a clean Ag(100) substrate; then we proceeded by depositing LiF for a total of 6 thicknesses. The reported spectra in this section refer to the samples A3, B3, C2, D3, E3 and F3 presented in Table 3.1.

All the acquired spectra were normalized to the incoming photon flux intensity, detected by the gold mesh, right before the measuring chamber, and interpolated to the same energy scale, with steps of 40 meV. For each sample thickness, spectra of same polarization were averaged, and an arbitrary straight line was subtracted from each averaged signal in order to make them match the lateral boundaries, namely the pre-absorption edge background and the tail of the fine structure extended region. The XAFS spectra were obtained by averaging the two polarizations $(\sigma_v + \sigma_h)/2$, while XNLD signal was obtained, by definition, as $\sigma_v - \sigma_h$.

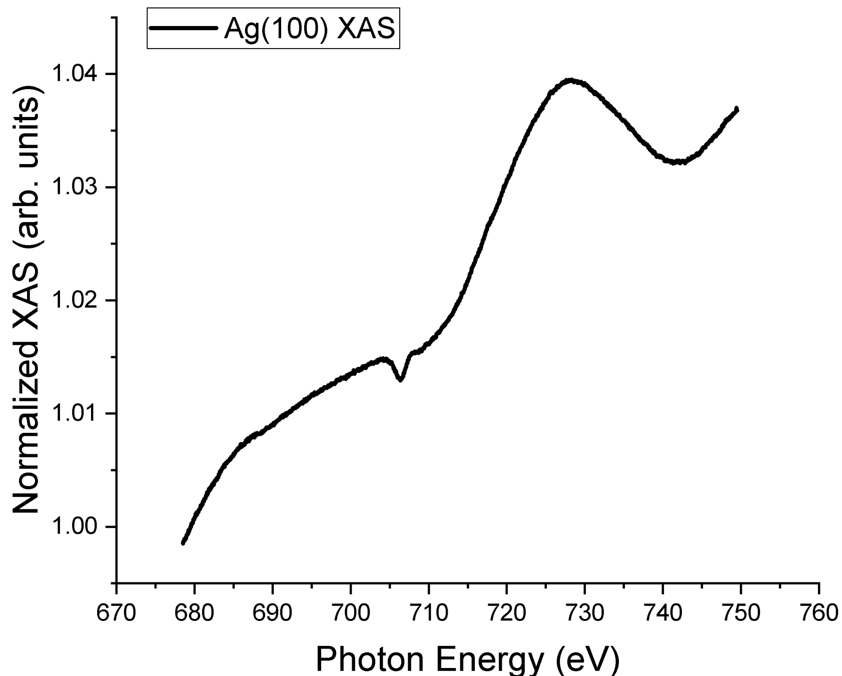

Figure 3.4: Clean Ag(100) XAFS at fluorine K-edge. The M1 Ag absorption edge is estimated to start at 715 eV.

The clean silver spectrum in Figure 3.4 shows the Ag M1 absorption edge starting around 715 eV, and a feature at 706.5 eV. The latter was systematically appearing for

every acquired spectrum, and it was attributed to the Fe L-edge, due to a contamination of the Au mesh measuring the incoming flux after the monochromator.

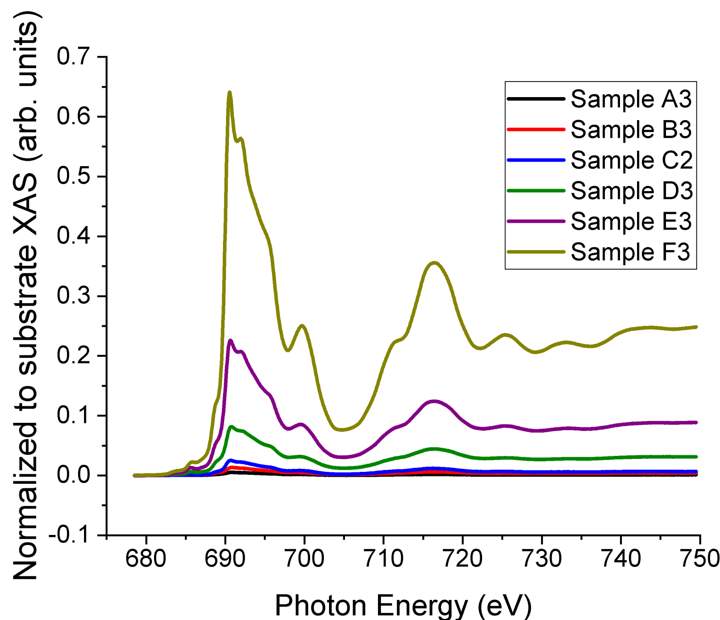

Figure 3.5: LiF/Ag(100) XAFS with varying thickness. The spectra are normalized to Au mesh and Ag spectrum.

Sample	Nominal # of layers	Conversion Factors α_C
A3	~0.2	0.21
B3	0.5	0.54
C2	1	1.00
D3	3	3.23
E3	6	8.94
F3	12	25.37

Table 3.2: Multiplying factors used to normalize spectra to the absorption peak at 690.75 eV of the nominal 1 ML thick sample.

The LiF/Ag absorption spectra in Figure 3.5 were normalized to the substrate signal, which is a reasonable assumption even for higher thicknesses, as the approximation of ultrathin film agrees with STM images (see Section 3.3). From the acquired XAFS spectra it was detected that the intensity of the signal increases with the amount of deposited material with a rather linear trend for low coverages (from 0.2 to 3 MLs). To compare the spectra for all the LiF thicknesses, it was chosen to consider the XAFS peak

at 690.75 eV as representative (labelled as "main"). As the coverage of the sample C2 was estimated to be of 1 ML ($\Delta f = 4.2$ Hz on QMB), the intensities of the "main" peak of the other spectra were confronted with the one of the C2 sample. The conversion factors α_C were obtained as the ratio of the "main" intensity peaks I_x/I_{C2}, where x are the samples A3, B3, D3, E3 and F3 are listed in Table 3.2.

The XAFS spectra were normalized by the conversion factors α_C to the intensity of the "main" peak of the nominal 1 ML coverage sample C2 and plotted in Figure 3.6. For coverage higher than 3 MLs, the intensity of the signal does not follow a linear behavior, which can be seen by plotting the conversion factors y versus the nominal thickness of the samples x (Figure 3.7). The general trend of the "main" peak can be approximated with a quadratic polynomial curve $y = A + B_1x + B_2x^2$. A good fit is obtained with parameters: $A = 0.06 \pm 0.10$, $B_1 = 0.80 \pm 0.06$ and $B_2 = 0.109 \pm 0.005$ (red curve in Figure 3.7).

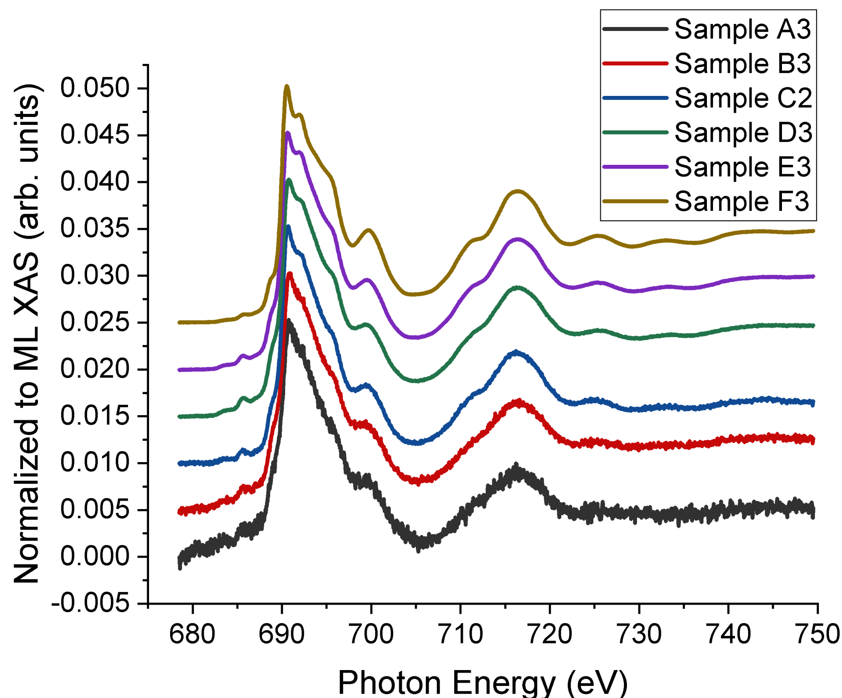

Figure 3.6: Fluorine K-edge of LiF/Ag, normalized to the main absorption peak intensity of 1 ML sample spectrum.

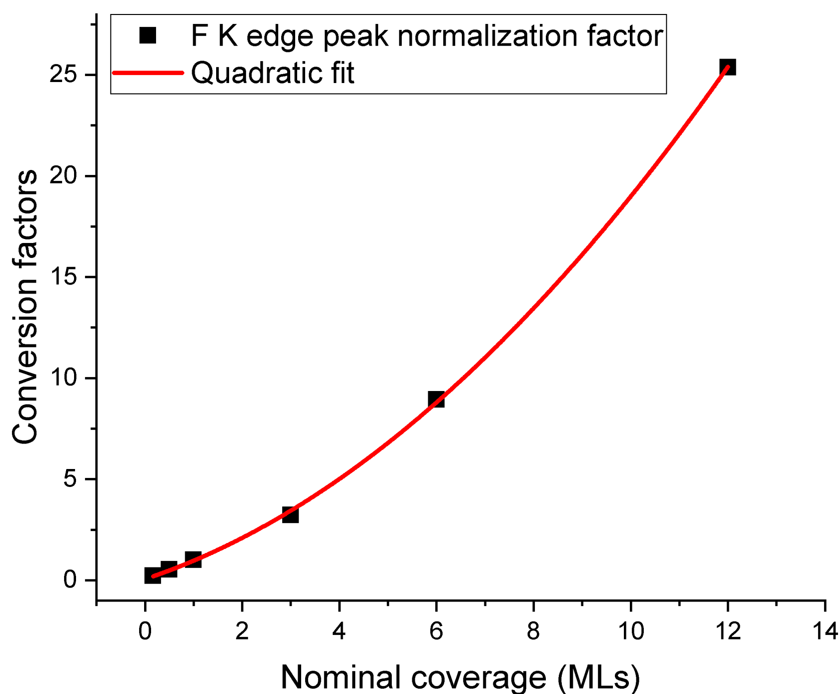

Figure 3.7: Conversion factors obtained from the normalization of the F K edge peak to the signal of the nominal 1 ML sample C2. The trend follows a parabolic behaviour.

In order to check whether the deposited LiF conserves the same lattice structure, as well as to exclude the possibility that the signal originated from a different material, a control experiment was performed with refernece samples.

As a reference for the LiF bulk signal, a LiF powder sample was prepared on carbon tape and measured with the same experimental conditions as LiF/Ag depositions. The signal was processed in the same way as the other samples, without the Ag normalization. The deposited LiF spectra were compared with respect to the bulk after a proper intensity normalization. In order to do so, the "main" absorption peak intensity of each spectrum was used to normalize its value to unity, respect to the pre-edge baseline, fixed to zero (Figure 3.8).

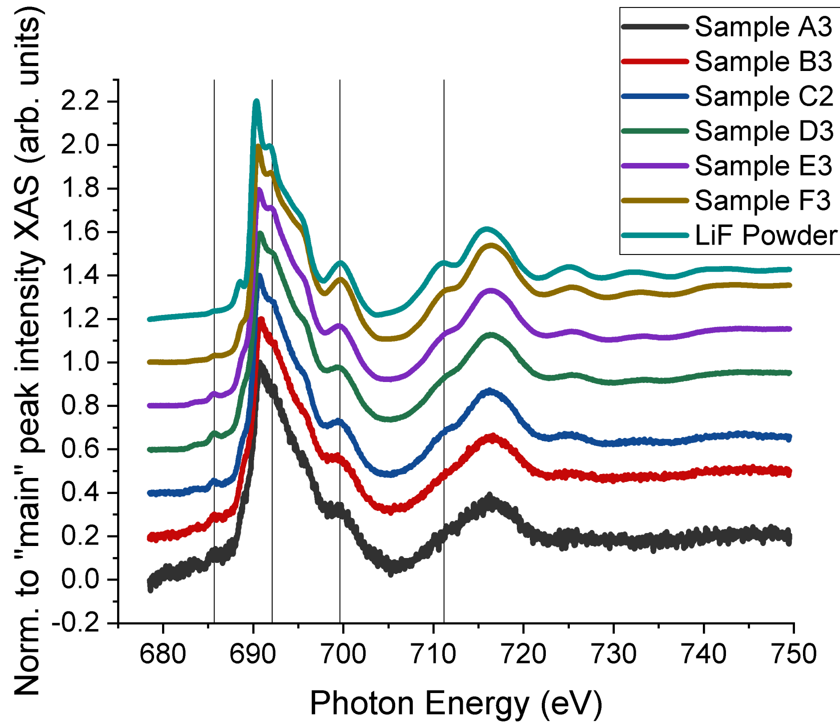

Figure 3.8: Fluorine K-edge absorption spectra of LiF/Ag, normalized to the jump.

By analyzing the evolution of XAFS spectra in Figure 3.8, it is possible to draw the following considerations:

1. The shape of the fluorine K absorption edge does not differ substantially from sub-monolayer coverage to bulk.

2. The intensity of the small pre-peak at 685.68 eV decreases with increasing thickness of LiF. This is clearly visible by looking at the trend of spectra from 6 to 12 MLs, and then to bulk (Figure 3.9).

3. The main peak is a superposition of two signals: the first centered at 690.75 eV and the second at 692.08 eV. At low coverage the ratio between the two is stable, while for 12 MLs and the powder sample the ratio increases. This affects the intensity of the whole shape of those spectra (especially the bulk one), as the height of the first peak was used for the normalization.

4. The position of the highest signal of the main absorption peak evolves with thickness from 690.90 eV at ~ 0.2 ML to 690.37 eV for bulk, with a non-linear behaviour.

5. The peak at 699.63 eV of the powder sample has a more pronounced height compared to the deposited LiF.

6. The shoulder at 711.07 eV, present since the first deposition, assumes a clear peak shape for the powder spectrum.

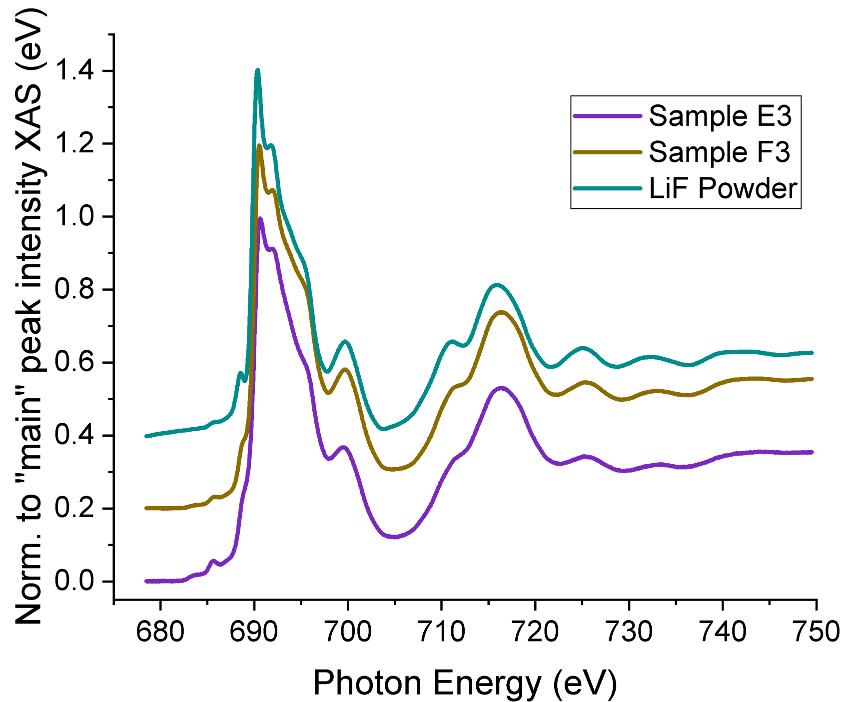

Figure 3.9: Overlap of 6 MLs, 12 MLs and bulk LiF fluorine K-edge spectra, normalized to the jump.

The fine structure of the acquired absorption spectra depends on the polarization of the incoming X-rays, as shown in the Figure 3.10. The dependence of the polarization is usually displayed in form of XNLD spectra, where the difference between the vertically and the horizontally polarized signals is reported. The shape of the LiF XNLD spectra, displayed in Figure 3.11, does not change considerably with the amount of material.

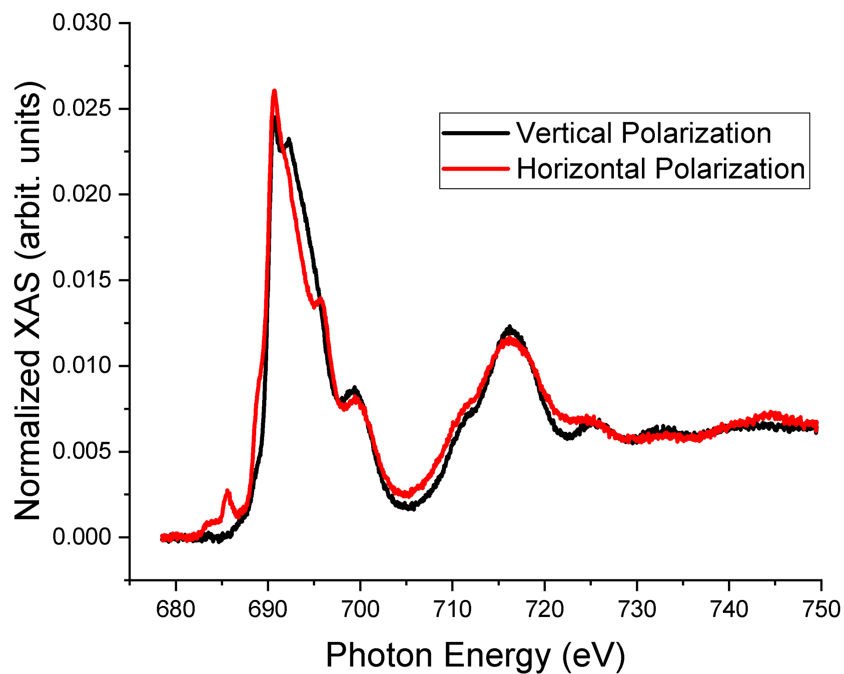

Figure 3.10: Polarization-dependent XAFS of the sample C2, normalized to the substrate.

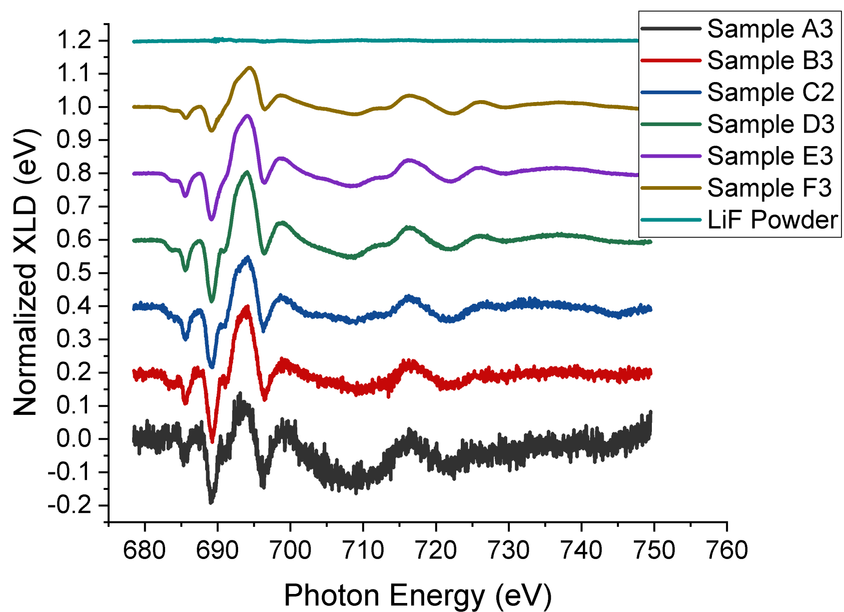

Figure 3.11: LiF XNLD normalized using the conversion factors in Table 3.2.

The intensity of the signal is normalized with the same conversion factors reported

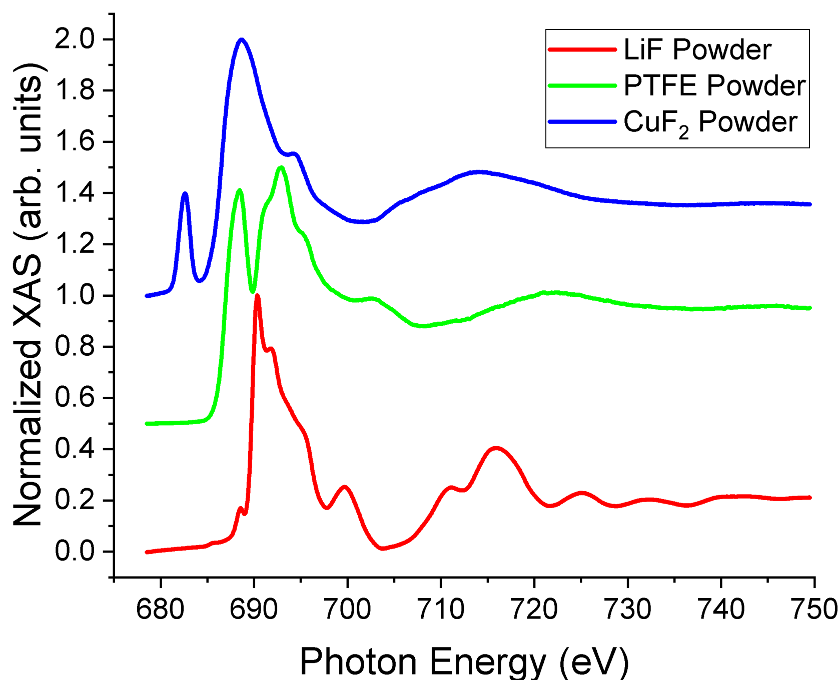

Figure 3.12: Fluorine K-edge of LiF, CuF_2 and PTFE powders. The spectra were normalized to the highest peak intensity.

in the Table 3.2. For sample A3 to E3, the intensity of the different peaks is slightly oscillating. The only exception is the F3 sample, which has a less strong XNLD. This is clearly visible at 689.3 eV, where the intensity of the F3 XNLD peak is lower by a factor of 2 compared to the E3 sample. As expected, the XNLD spectrum of the LiF powder gives no reasonable signal.

The LiF powder spectrum was found to be in good agreement with literature data of bulk lithium fluoride crystal [63]. Two other fluorinated compounds were measured and compared at the F K absorption edge (Figure 3.12).

Copper difluoride (CuF_2) was chosen among other materials, as it has a different stoichiometry while still being a fluorinated metal compound. Polytetrafluoroetilene (PTFE) is a good candidate to represent organofluorinated materials for its different structural shape and a well-known fluorine K-edge [64],[66]. All the three XAFS spectra were collected at normal incidence and the signals were normalized by setting the pre-edge to 0 and the maximum peak intensity to 1. Compared to LiF powder, CuF_2 spectrum shows a much broader fluorine absorption K-edge, while the peak maximum is shifted by 1.6 eV toward higher energies. At 682.6 eV there is a quite pronounced pre-peak, which in the other two compounds is shifted by almost 6 eV.

The PTFE spectrum displays a much more structured shape of the main peak. The maximum is shifted to higher energies by 4.08 eV compared to LiF, while the pre-peak

is stable at 688.5 eV, at the same position of that in the LiF spectrum. The main difference of the two pre-peaks is their intensity, which is much higher in the PTFE signal. All the three spectra show a shoulder on the right of the main peak. Despite the adsorption edge evolves at higher energies for all the spectra, lithium fluoride displays a clear second peak centered at 716 eV. The great difference in the fine structure of the fluorine K edge underlined even more the peculiar shape of the LiF spectra. The spectra in Figure 3.12 are all in agreement with the ones found in literature [63],[64],[66],[67]. These considerations, along with the remarkable match of the deposited spectra with the distinct shape of the LiF powder, provide the evidence that the deposited compound is lithium fluoride.

3.3 LiF Surface Morphology

The morphology of LiF/Ag(100) surface was studied by scanning tunneling microscopy (STM) in UHV environment. Square images from 250 nm to 500 nm were collected with a 516X516 pixels resolution. The feedback loop gain was set according to the scan speed (1 line/s).

At first, the microscope was used to check the cleanliness of the silver substrate during the sputtering and annealing cycles. The STM tip was prepared by pulses of ± 7 V alternated with indentations on a clean Ag surface up to 5 nm. Terraces up to 200 nm were observed on the surface, which was assumed to be the Ag(100) surface, later confirmed by LEED patterns (see Section 3.4). The orientation of the steps on the surface, as well as their density, showed differences depending on the scanned area. Due to a high thermal and electical noise level of the microscope, a rather high fluctuations of the tip position was detcted. The uncertainty was estimated with the standard deviation method. An example of the Ag surface scan is shown in Figure 3.13. With a bias voltage of -1V and a current set-point of 100 pA, the apparent height of the steps is (2.5 ± 0.3)Å.

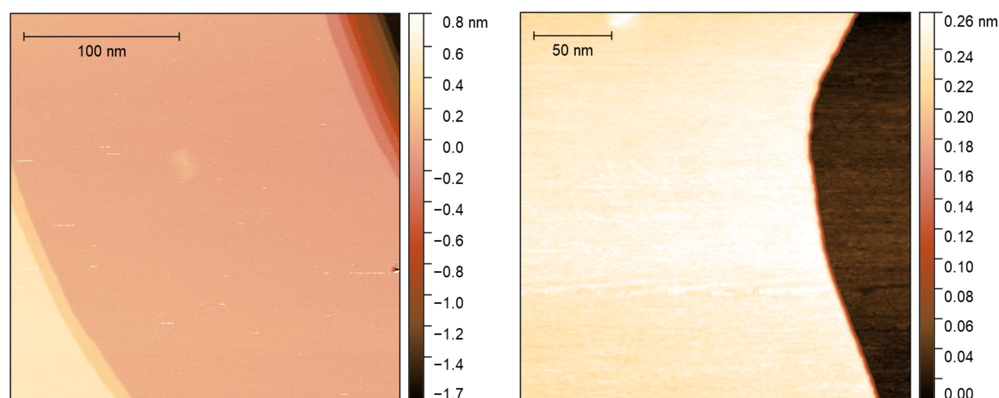

Figure 3.13: STM images of Ag(100) surface at -1 V bias and 100 pA current set-point.

After the deposition of the sample A4 ($\Delta f = 0.7$ Hz on QMB), the current set-point was lowered to 10 pA and, at +1 V, a tiny amount of material was detected on the surface and along the step edges, on both sides of the steps (Figure 3.14 left).

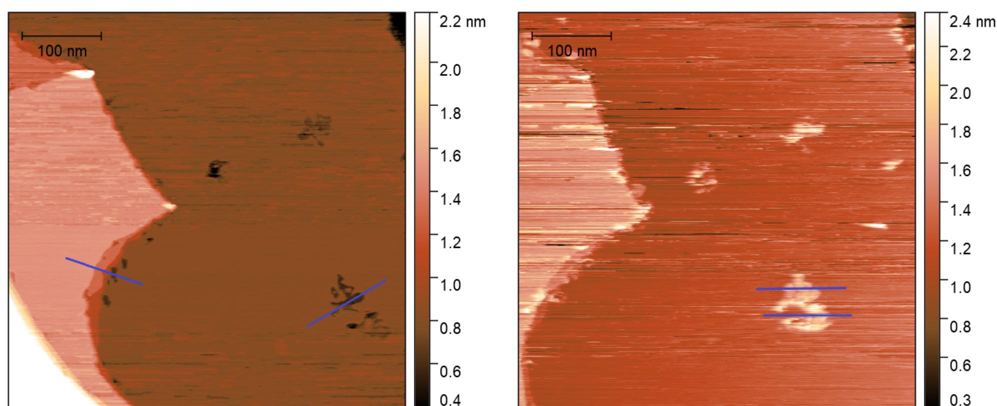

Figure 3.14: STM images of sample A4 surface at 10 pA current set-point, (left) +1 V and (right) +5 V bias voltage.

Linear profiles (marked in blue) show islands of average depths of (2.5 ± 0.3)Å. The origin of depths rather than heights is the poor conductivity of adsorbed insulating LiF on the surface. The stacking of a second layer of lithium fluoride was also detected, with (5.0 ± 0.3)Å average depth, compared to the Ag terrace level. At room temperature, the microscope was unable to operate in the dI/dV spectroscopy mode, but a sweep in voltage from -6 V to 6 V was performed on different positions of the scanned area. A reproducible change in contrast was detected at bias voltage of +3.8 V, which was also seen for all the other LiF coverages. The phenomenon was explained by the matching of the Fermi level of the tip with the conduction band of LiF induced by the bias, which increased drastically the conductivity through LiF islands, changing the apparent height profile from depths to elevations. Both the images in Figure 3.14 show the same area, but at a different bias voltage. At +5 V, LiF islands have a height profile ranging from (4.0 ± 0.3)Å to (9.8 ± 0.3)Å, without any clear step shape on the LiF surface. No thickness variation was detected for Ag steps between the two images. The slight difference in topography of the two is caused by thermal drift of the tip (see below). Subsequent depositions of LiF on Ag(100), from $\Delta f = 2.1$ Hz (sample B4) to $\Delta f = 25.2$ Hz (sample E4), are presented below.

Figure 3.15 displays two images taken at a nominal thickness of half a monolayer (sample B4), while in Figure 3.16 a nominal coverage is 1 ML (sample C2) is shown. Both the Figures were taken at +1 V bias voltage and low current set-points. The images on the left display stepped areas where it is clearly visible that LiF nucleates along the step edges, with a lateral extent of a few nanometers. From the LiF along the steps, branches of different lengths extend both above and below the edges, along some preferred

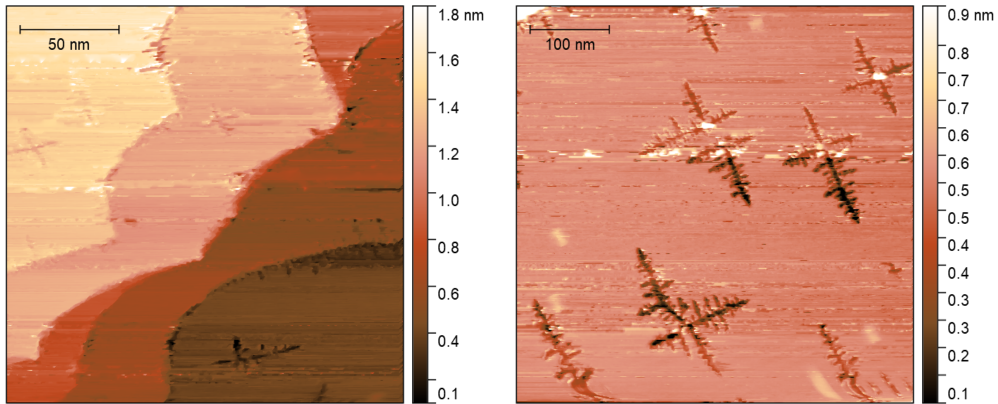

Figure 3.15: STM images of sample B4 surface at +1 V bias voltage, (left) 10 pA and (right) 1 pA current set-point.

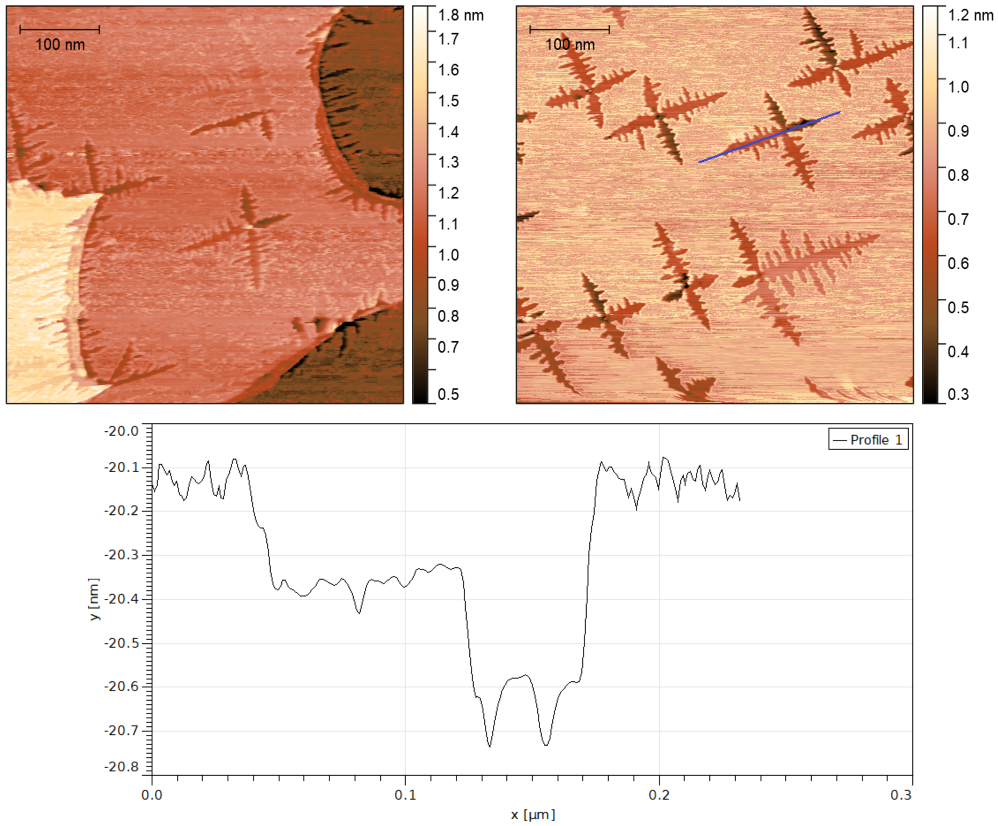

Figure 3.16: STM images of sample C2 surface at +1 V bias, (left) 1 pA and (right) 5 pA current set-point. Below, the line profile reported in blue in the image on the right.

directions. In the images on the right, the nucleation of LiF on Ag(100) flat terraces can be observed. The nucleation occurs by forming dendrites of a core "X" shape, with the two main arms oriented almost perpendicularly one with respect to the other. In most cases a deviation of $3 - 5^{\circ}$ with respect to right angle was found and, in rare cases, it was as much as 10°. The four perpendicular arms extend from a common nucleation center at their intersection, where a change to a positive height was often observed. The nucleation spots were therefore recognized to be impurities, vacancies or kinks along the step edges. The extent of the main arms did not have a fixed length, although structures longer than 150 nm were not detected. Every main arm of a dendrite displays smaller perpendicular branches, which in turn have other sub-branches perpendicular to them, with no apparent trend on lateral or longitudinal extent. The axes of the dendrites are rotated counter clockwise on average by of $(19 \pm 3)^{\circ}$ compared to the image frame. The uncertainty on the angle rotation is related to a non-uniform lateral thickness of the main arms, which limited the detection of the growth direction with a greater precision. In several cases, a deviation from this geometry was detected, which is explained later in this paragraph. In the left image of Figure 3.16 the lateral LiF branches evolve into a dendritic shape, with the same preferred growth direction as explained above.

In Figure 3.16 is also reported a height profile of a dendrite, taken along one of the main axes of LiF growth (blue line), which is extracted from the right image of the Figure by averaging on a 5 pixels thick line. Although two levels of the structure can be easily spotted, with terraces at (2.5 ± 0.3)Å and (5.0 ± 0.3)Å below the Ag surface, deviations from this structure, above the uncertainty value, were found in multiple cases.

Figure 3.17 displays two images of the sample D1, taken at 1 pA current set-point, but at different bias voltages. The two images were collected by two consecutive scans of the same area, with the change of the sole bias voltage between the two. In the same Figure the height profile of the blue line in the image on the right is reported. By looking at the height distribution, no clear terrace is visible, although various steps of approximative 0.2 nm height are present. The maximum height of the dendrites reaches (10.0 ± 0.3)Å compared to the substrate level, with a random distribution of the step positions. Indeed, no major nucleation center is detected above the first layer of LiF. An atomic corrugation is present on the surface of steps, whether it is not clear if the cause is a physical effect rather than noise.

The images in Figure 3.17 are presented again in Figure 3.18, where is made clear that the step edges (blue), compared to the frame of the image, have different orientation and a slightly different geometry. With the help of highlighted arms (dark green) and secondary branches (light green) of some chosen dendrites, it is rather easy to convince oneself that the two images are not just rotated one respect the other (estimated $\Delta\Theta \sim 19^{\circ}$), but the direction of the dendrite arms is distorted by the creep of the piezo motors of the microscope. Due to a small thermal drift of the tip or sample, the shape of the image could be distorted. Moreover, the drift could affect the sampled area in two consecutive scans, by moving the area boundaries. The change of the bias voltage moves the tip

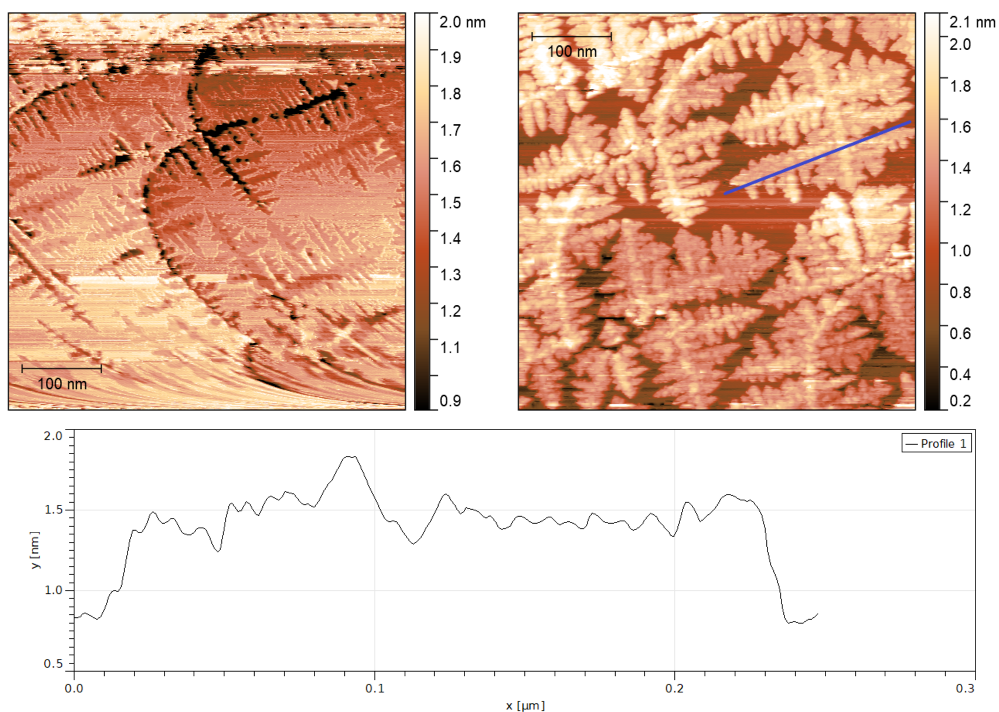

Figure 3.17: STM images of sample D1 surface at 1 pA current set-point, (left) +1 V and (right) +4.5 V bias voltage. Below, the profile of the blue line in the image on the right.

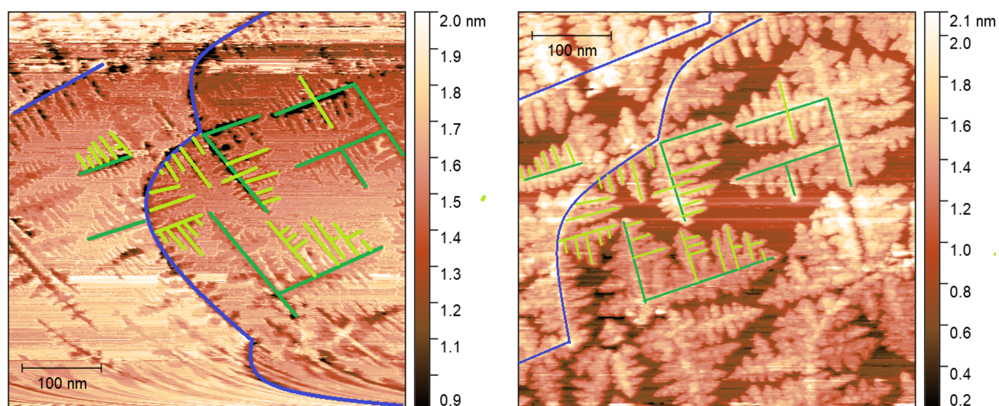

Figure 3.18: Changes in topography of the same area at two consecutive STM scans of sample D1 at 1 pA current set-point, (left) +1 V and (right) +4.5 V bias voltage. The blue curve highlights the Ag step edge, while dark green and light green represent some chosen main and secondary branches of LiF dendrites.

with respect to the sample surface, which also could affect the tip condition and/or drag the LiF between the dendrites, thus changing slightly the shape of the structures. Those effects are the main reasons of the apparent differences in topography between the two images in Figure 3.18. With that in mind, it is possible to understand why some STM images displayed different growth directions of the LiF branches with respect to the image frame and why some of them do not display straight arms. This is also justified by the fact that all the dendrites display a distorted growth direction within the same image, while some scans showed an obvious bend of straight lines.

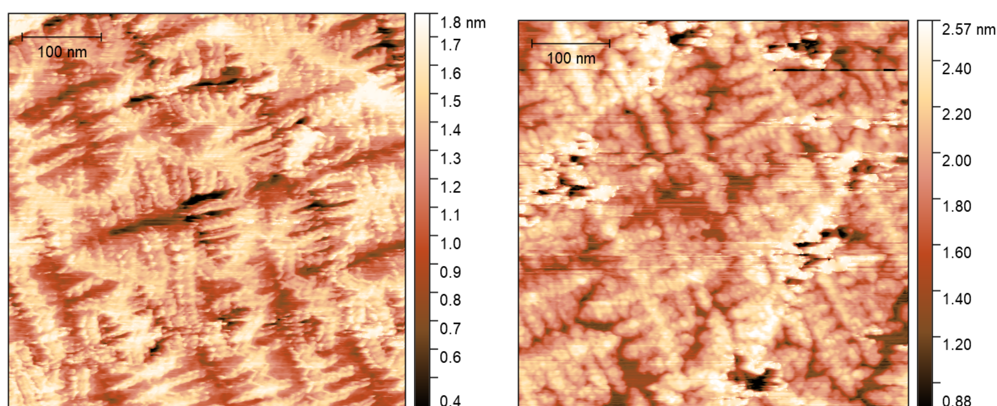

Figure 3.19: STM images of sample E4 surface at 1 pA current set-point, (left) +1 V and (right) +4.2 V bias voltage.

In Figure 3.19, two STM images of the E4 sample (Δf = 25.2 Hz on QMB) are displayed. The image on the left was collected at 1 pA current set-point and +1 V bias, while the one on the right was scanned at +4.2 V. The images display two different areas with the previously explained contrast due to the bias voltage. On both the images the island density is increased with respect to the previous deposition (Figure 3.17), although small flat areas of the substrate between the dendrites are still present.

The longitudinal extension of the dendrites scaled up with the amount of deposited material, for a maximum detected length of 250 nm for the sample E4. The lateral extension of branches also increased from 7 nm of the sample B4 to 45 nm of the sample E4.

The scanning of the sample F1, with a nominal coverage of 12 MLs gave no reliable outcome, most probably due to the insulating nature of the LiF.

The surfaces with different LiF coverage presented also other general phenomena:

- Subsequent scans of the same areas of samples B4, C2, D1 and E4 showed that the position of the dendrites does not change over time. As explained above, defects and impurities were detected to be the nucleation centers of the dendrites in most cases (Figure 3.15 and 3.16), which could strongly affect the pinning of the LiF to the surface.

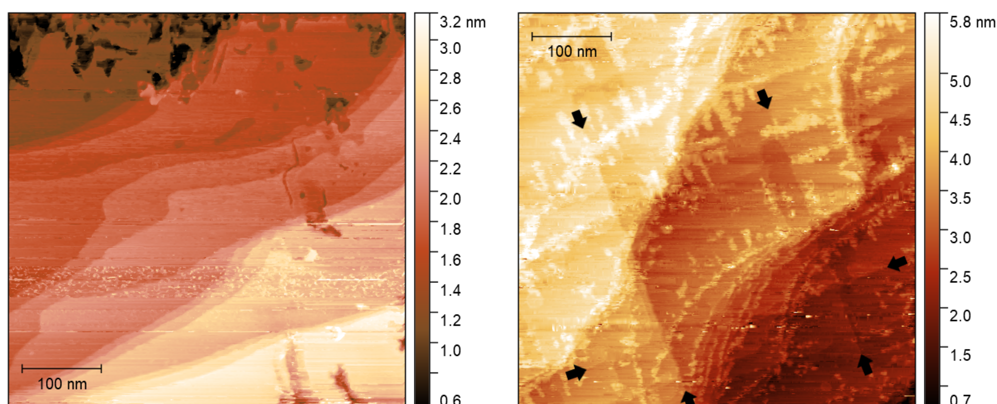

Figure 3.20: STM images of LiF/Ag(100) surface. On the left, Ag terraces and mobile non-structured LiF on sample E1 at +1 V bias and 1 pA current set-point. On the right, test sample (1.5 nominal ML) at +6 V bias and 10 pA current set-point; black arrows enhance the position of steps originated form a tip crash on the surface.

- In STM images of samples D1 and E4 a quite high spatial inhomogeneity of LiF dendrite density was found. Sample D1 was produced in a single deposition, after which other three nominal MLs were added after 24 hours to form the sample E1. Scans of 250 nm square areas (Figure 3.20 left) emphasized partially clear silver terraces, free from LiF dendrites. As some of the scans were done many hours after the deposition, mobile LiF could have nucleated to form the non-structured islands in Figure 3.20.

- In some cases, subsequent scanning of the same area showed a variation of the positions of smaller non-structured islands of LiF reported in Figure 3.20. The detected islands do not have a nucleation center like the dendrites explained before. The reason for this behaviour is not clear but it could be related to the absence of pinning centers for the LiF islands combined with a high mobility of the islands. It is also probable that the STM tip interaction with the sample could have dragged the islands on the terraces, which is why the positions of the islands changed.

- A first "trial" sample of LiF was deposited for a total amount of 1.5 nominal ML LiF coverage. While testing the STM on this sample a light crash of the tip on the surface occurred. After this event straight lines were detected on the surface, which were attributed to the formation of line dislocations, caused by the compressive stress exert by the tip. The lines match the $< 100 >$ crystallographic directions of the substrate and the direction of LiF dendrites growth, which is later confirmed by LEED patterns (see next Section 3.4).

3.4 LEED of LiF/Ag(100)

The surface symmetry and the growth mode of LiF/Ag(100) was studied with a commercial low energy electron diffraction instrument, as explained in Chapter 2. A qualitative analysis of the diffraction spots was performed both on clean Ag(100) surface and on the samples A5, B5, C5, D5, E5 and F4 (see Table 3.1). The samples were checked in the electron energy range from 60 eV to 225 eV. The reported images were collected at the same Wehnelt potential and at three representative electron beam energies of 60 eV, 112 eV and 170.5 eV. For the comparison of the patterns, a filter with the same brightness conditions were applied to the raw images.

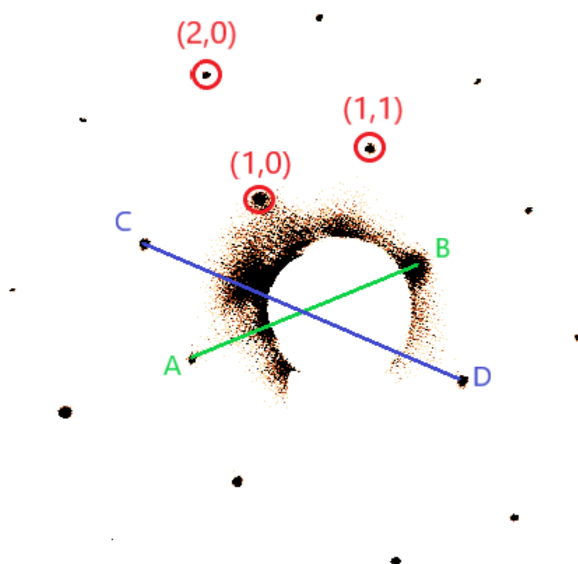

Figure 3.21: LEED pattern of Ag(100) surface at 130 eV electron energy. Three chosen diffraction points are labelled in red. The blue line links the two equivalent (1,1) spots, while the green one connects the equivalent (1,0) spots.

At first, the clean Ag(100) surface was checked and the fourfold symmetry was determined. To prove that the LEED pattern of silver comes from the (100) surface, the diffraction pattern at 130 eV electron energy was used (Figure 3.21). By assuming the labelled diffraction points in the figure as correct, the ratio AB/CD corresponds to the ratio of the magnitude of reciprocal vectors pointing at the (1,0) and (1,1) points. From the Bragg's law (2.11), by fixing the electron wavelength and the distance $d_{hk\ell}$ along the silver (100) and (110) directions, the diffraction angles $\Theta_{(100)}$ and $\Theta_{(110)}$ can be determined. At normal incidence, the ratio $tan\Theta_{(100)}/tan\Theta_{(110)}$ corresponds to the ratio

AB/CD of the reciprocal space vectors. Within the uncertainty coming from the LEED width spots, the assumptions proved correct by using the nominal values of the Ag bulk lattice reported in litterature [68], $d_{100} = 4.086$Å and $d_{110} = 2.889$Å. The Ag(100) LEED patterns were also confronted with the ones reported in literature and found to be in good agreement (see next Section 3.5). For comparisons with the LiF diffraction patterns, the Ag(100) patterns at the three relevant energies are displayed in Figure 3.22.

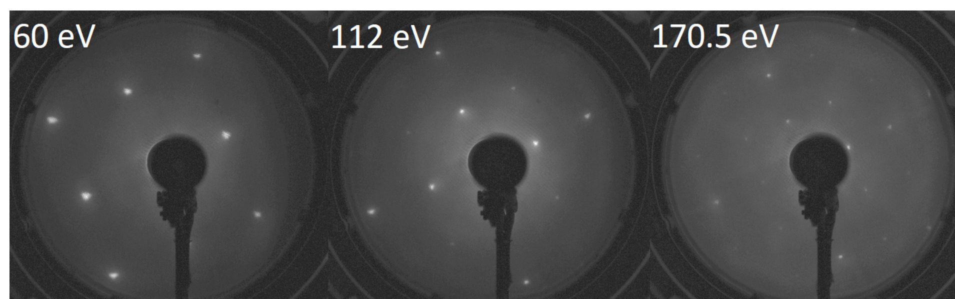

Figure 3.22: LEED pattern of a freshly prepared Ag(100) surface at 60, 112 and 170.5 eV electron energies. Images are collected at the same Wehnelt voltage and are processed with the same brightness filter.

The positions of the diffraction spots for different LiF thickness are presented below.

In Figure 3.23, an increasing coverage of LiF/Ag(100) is displayed, with the same labelling presented in Table 3.1. For thicknesses up to 1 nominal ML (samples A, B and C), no major difference from the clean Ag(100) pattern is observed (Figure 3.22). However, images D and E display a progressive fading of the peak intensity and the broadening of the diffracted spots, with almost vanishing spots along <110>directions for the sample E4 (Figure 3.23 E). In the Figure 3.23 F, the reappearance of the (1,1) spots goes along with an increase in the intensity of the (1,0) points. The expansion of the peak width is evident, with a shift of the FWHM on the angle of the reflection from 0.4° (Figure 3.23 A) to 1.3° (Figure 3.23 F).

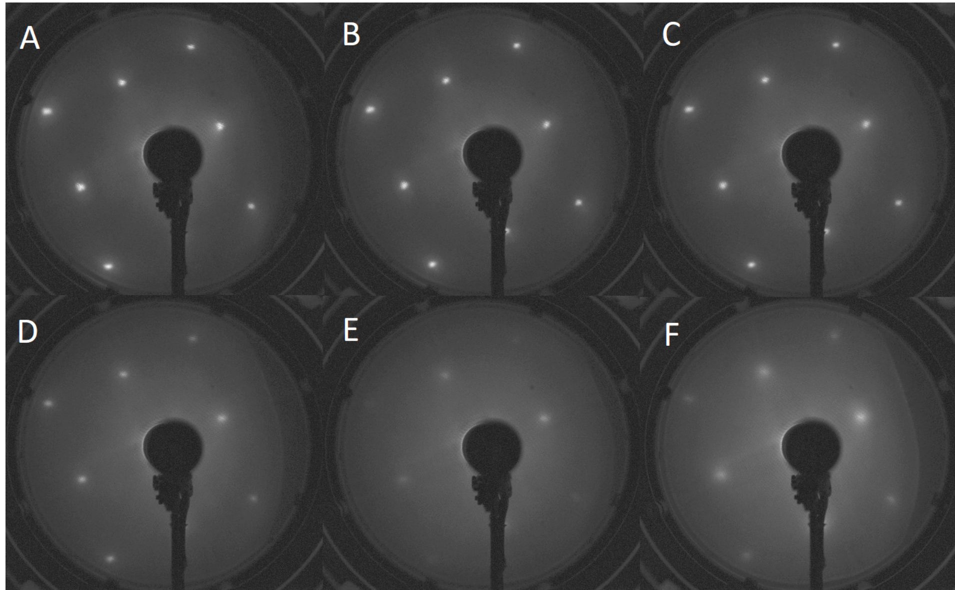

Figure 3.23: LEED pattern of LiF/Ag(100) surface at 60 eV electron energy. The labels correspond to (A) 0.7 Hz, (B) 2.1 Hz, (C) 4.2 Hz, (D) 12.6 Hz, (E) 25.2 Hz and (F) 50.4 Hz of frequency variation on the QMB reference measurement. Images are collected at the same Wehnelt voltage and are processed with the same brightness filter.

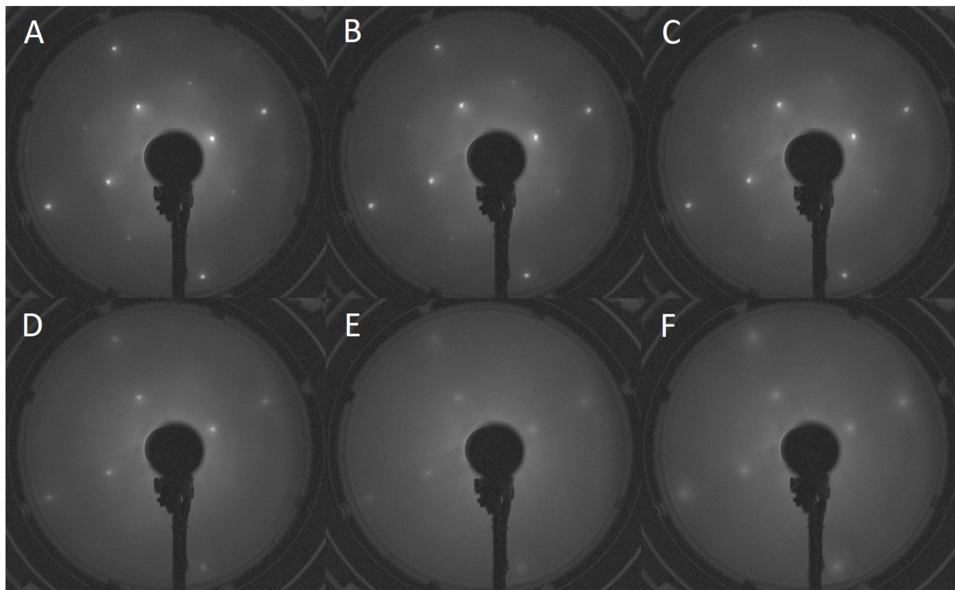

Figure 3.24: LEED pattern of LiF/Ag(100) surface at 112 eV electron energy. The labels correspond to (A) 0.7 Hz, (B) 2.1 Hz, (C) 4.2 Hz, (D) 12.6 Hz, (E) 25.2 Hz and (F) 50.4 Hz of frequency variation on the QMB reference measurement. Images are collected at the same Wehnelt voltage and are processed with the same brightness filter.

Figure 3.24 displays the diffraction patterns collected at 112 eV electron energy. As for the previous series, the first three images do not deviate appreciably from the silver pattern. However, a progressive decrease in brightness of the (1,1) peaks is visible, until the complete vanishing in the Figure 3.24 D. At a nominal thickness of 3 MLs (Figure 3.24 D), the (1,0) and (2,0) spots visibly start fade away along with the broadening of the spots, which culminates for the E sample, where the fourfold rotational symmetry is barely visible. The last image displays the pattern from the highest LiF coverage and, although the peaks width does not shrink, the intensity is higher than the one in Figure 3.24 E, if compared to the background brightness level.

Figure 3.25 displays the LiF electron diffraction patterns at electron energy of 170.5 eV. The points along the <100>directions are more intense in the whole series and, as previously, there is a progressive smearing out of the other spots. In Figure 3.25 D the (1,0) and (2,0) points are hardly visible. By confronting it with the image of the sample E, it is possible to estimate a higher background level of the latter and the broadening of the shape of the almost vanishing (1,0) and (2,0) diffraction spots. Figure 3.25 F deviates from this trend by recovering the points along the <100>directions, as well as the (1,1) spots.

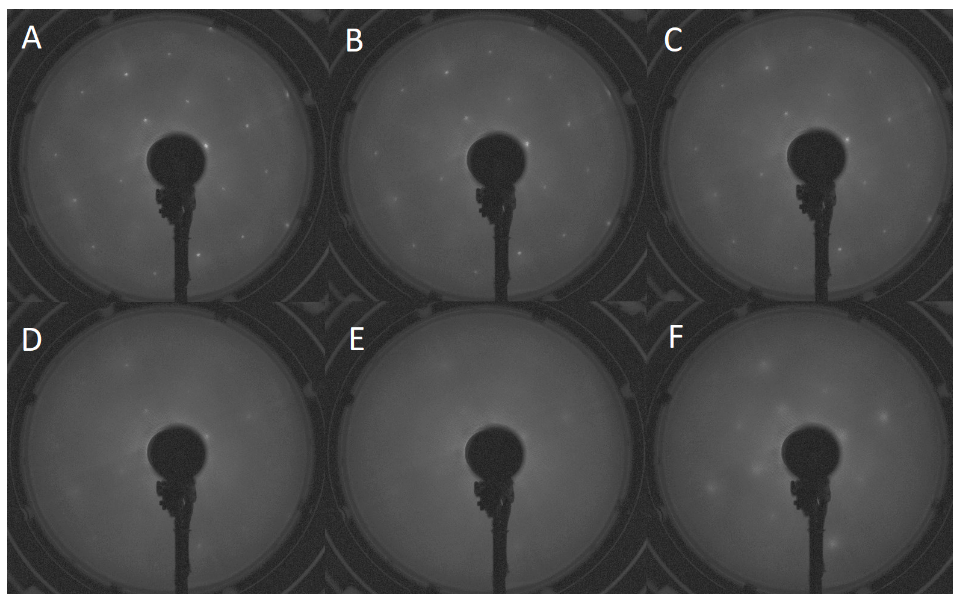

Figure 3.25: LEED pattern of LiF/Ag(100) surface at 170.5 eV electron energy. The labels correspond to (A) 0.7 Hz, (B) 2.1 Hz, (C) 4.2 Hz, (D) 12.6 Hz, (E) 25.2 Hz and (F) 50.4 Hz of frequency variation on the QMB reference measurement. Images are collected at the same Wehnelt voltage and are processed with the same brightness filter.

3.5 Discussion

In this section, all the data collected on the growth mode of LiF/Ag(100) and illustrated above are summarized and critically discussed.

First of all, the assumption of the sticking coefficient to be $S_C = 1$ let us estimate a nominal LiF coverage of 1 ML for $\Delta f = 4.2$ Hz frequency shift on the quartz balance with the Sauerbrey equation. However, this estimation was discredited by the STM scans, which showed a coverage at least three times less than expected for 1 nominal ML of LiF (Figure 3.16). A precise esteem of the sticking coefficient proved to be challenging, as the LiF growth mode does not follow the planar layer-by-layer growth, which makes it difficult to evaluate the real amount of material on the surface. The STM analysis confirmed that our approximation of the sticking coefficient was rather crude. A multiplication factor of ≈ 0.3 on the nominal coverage would give a more realistic amount of material.

F K-edge XAFS spectra were measured using linearly polarized light. The same lineshape of the spectra was found for all the LiF coverages (Figure 3.8). The XAFS signal was then compared to the powder reference and a remarkable match between the bulk and the thin film absorption spectra was found (Figure 3.9). This confirms that the fluorine on the silver surface has the same environment of the bulk LiF, such that the composition and stoichiometry of the adsorbate during the transfer from source to substrate is conserved. XAFS spectra of copper difluoride and polytetrafluoroethylene powders were also measured, displaying a completely different fine structure due to the different local environment, as expected (Figure 3.12). A good agreement was found for both the reference compounds [66], [67], [69] and the LiF spectra reported by Balasubramanian et al. [63].

The LEED pattern of the clean (100) silver surface was studied at different electron energies and the fourfould symmetry, expected for the FCC structure, was detected (Figure 3.22). The Ag diffraction spots of the (100) surface detected at 60 eV are validated by the images reported by Palmberg et al. [70] at 58 eV. Also, J. Wang [71] presents an Ag(100) pattern taken at 110 eV, displaying the (1,0) spots with stronger intensity than the (1,1), the same behavior we report for the 112 eV pattern in the present work (Figure 3.22).

As the bulk LiF lattice constant has a mismatch of 1.4% with respect to the silver, tensile strain of deposited LiF films was expected. The deviation from the cubic symmetry was detected by XNLD measurements of the samples (Figure 3.11). LEED measurements showed also variations of the diffraction patterns with increasing thickness of LiF.

The growth mode of lithium fluoride on Ag(100) surface was detected for low coverages, with depositions on the substrate held at room temperature. The orientation of the LEED pattern of the clean Ag(100) surface in Figure 3.22 was confronted with the

STM images and it was determined that lithium fluoride grows mainly along the [001] and [010] directions of the substrate. Such anisotropic growth was detcted for all the studied samples.

At electron energies of 60 eV, coverages $\leq$ 1 nominal ML did not alter the clean Ag(100) diffraction pattern and no variation of diffracted peaks or the appearence of new spots was detected. This agrees with STM images that show large areas of bare substrate, where most of the LEED signal comes from, as shown in Figure 3.26.

For samples from D to F, the signal coming from the LiF starts to be significant. A progressive broadening of the diffraction spots with the amount of material on surface is detected. The pattern also shows the fading of (1,1) spots. The latter behaviour was also reported by Mechehoud et al. [72] as well as Ouvrard et al. [73] for ultrathin MgO films deposited on Ag(100) surface. The loss of the (1,1) diffraction spots of thin MgO films was also reported by Valeri et al.[74]. As MgO shares similarities with LiF lattice structure, the fading of (1,1) diffraction peaks is expected to have its origin in the interference by atoms in the unit cell. Indeed, the (1,1) spots intensity fades progressively as the LiF islands cover the silver substrate, the same behaviour reported for MgO [73].

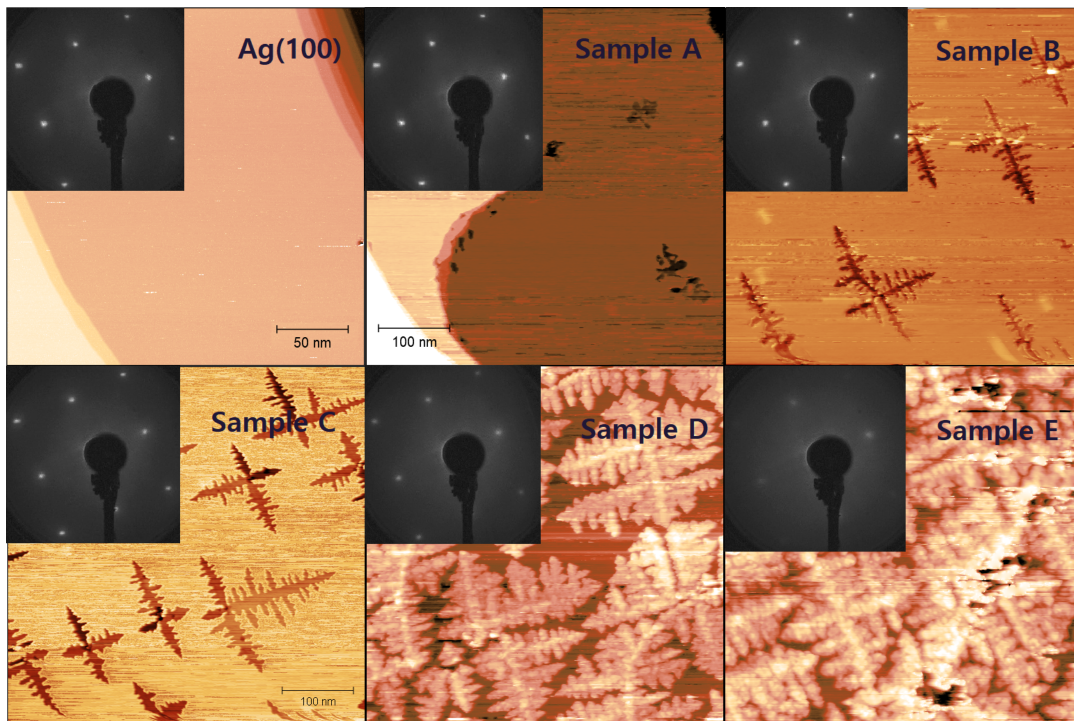

Figure 3.26: Selected STM and LEED images of bare Ag(100) and samples A, B, C, D and E, taken from Section 3.3 and Figure 3.23.

The broadening of the diffraction spots with the amount of material is attributed to

the growth mode: for low coverages a complete registry of the deposited material and the substrate is expected, due to the LiF strain on the Ag surface. With increasing thickness of the deposited material, the amount of grain bondaries and step edges of LiF dendrites increases. This cause deviations from the stuctural long-range order, which affects the shape of the LEED diffraction spots. Moreover, the presence of smaller branches of lateral extension on the order of few nanometers, as well as the out-of-plane inhomogeneous growth of LiF, contribute to the broadening of the diffraction peaks. Also, it is not to be excluded that the LiF lattice constant of the topmost layers of the samples D, E and F tends to relax to that of the bulk value, as the thickness of the sample increases, which can also contribute to broaden the shape of the peaks.

Indeed, it is expected that multilayer LiF grows with bulk lattice constant, as reported by Roberts et al.'s study on the LiF/Pt(111) surface [75]. Their work displays a LiF diffraction pattern taken at 106 eV, that resembles the one in the present work at 112 eV (Figure 3.24). However, they annealed the substrate at $\sim 300°$ C after deposition, which makes a direct comparison of the diffraction pattern impossible.

At 112 eV electron energy the behaviour is rather similar (Figure 3.24). LEED patterns at 170.5 eV display a progressive fading of the diffraction spots even at low coverages, although hardly visible as a low signal was detected even for bare Ag (Figure 3.25).

The STM images display an anisotropic growth of the material in the shape of dendrites, with the developing of the main branches in-plane, along the silver <010>directions, and smaller secondary branches perpendicular to them. The evolution of the dendrites with amount of LiF is presented in Figure 3.26.

In the work of Braun et al. on the fractal growth of LiF on Ag(111), dimers are assumed to be the smallest stable cluster size. By assuming ionically bound LiF dimers as stable diffusing units in our case as well, the dendritic growth of LiF can be explained due to a combination of several factors. In the experimental conditions of our work, the low LiF-Ag interaction determines highly mobile LiF dimers and small clusters, which diffuse toward greater islands. This also can explain why larger LiF dendrites are preferable instead of small LiF islands. Moreover, the diffusion rate across the LiF steps of adatoms impinging on LiF islands is lower than the lateral growth rate of the dendrites. In fact, the strong ionic interaction of LiF-LiF dimers cause an island growth also perpendicularly to the surface, with increasing thicknesses for samples from A to E (Section 3.3).

The in-plane growth is determined by energetically favourable spots at the LiF cluster edges, which are located at the <010>angles, as polar edges are generally avoided [76]. At low temperature, an anisotropic diffusion of LiF on Ag terraces is also expected, as diffusion rates along lower energy directions dominate. This two factors contribute to the dendritic island formation on the surface. Surface defects act as nucleation centers, by pinning small LiF clusters to the surface, where incoming LiF monomers or small clusters bind along the energetically favourable directions. Such directions coincide with

the <010>directions of both the Ag substrate and the LiF, which was observed and reported in the previous sections.

By line profiles extracted from STM images, we detected an inhomogeneous vertical extension of LiF islands (Figure 3.17), which agrees with the strong LiF-LiF binding behaviour stated above. The vertical growth is thus believed to be at the first stages of LiF on LiF columnar growth. The work of Kaiser et al. [77] confirms this hypothesis, as they present a study done on LiF films ranging from 50 to 500 nm deposited on different substrate temperature by PVD. Following the classical structure zone model (SZM), they claim that grains, with the (100) surface almost parallel to the surface, grow on room temperature substrates. This shape originates mainly from poor surface diffusion of LiF impinging on LiF films, which correspond to the zone 1 definition of the SZM model. In the sub-monolayer regime, as in the present work, the first monolayer of LiF aggregates in a dendritic shape and grows in plane by following the substrate lattice direction, while out of plane the growth is supposed to be columnar.

We also report a difference in the trend of both the XNLD shape (Figure 3.11) and the LEED images occurring at the thickness transition from sample E to sample F (Figures 3.23 - 3.25, images E and F). The XNLD spectrum of sample F3 shows a reduction of the intensity up to 50%. The reason of this could be found in the strain relaxation of the topmost LiF layers and a partial recovery of the octahedral symmetry of the LiF film of such thickness. At the same thickness, which corresponds to actual ≈4 MLs (with the considerations from above), LEED spots display higher brightness compared to the previous coverage. A higher intensity of the spots reflects a more ordered structure of the surface topmost layers. This behaviour confirms that LiF grows out-of-plane, as discussed above.

A small distribution of round shaped LiF islands was detected on few areas of the samples D1 and E4 (Figure 3.20), but this was attributed to a variation of the sample preparation, as explained in Section 3.3.

Conclusion

The purpose of this research was to understand the growth type of ultrathin LiF films deposited via thermal sublimation on an Ag(100) surface at room temperature. It was found that LiF forms 3D islands with a strong anisotropic growth along the substrate plane, in the shape of dendrites.

The performed XAFS analysis revealed a remarkable match of the F K-edge spectra of the deposited LiF and the powder sample, thus confirming that the fluorine local environment of LiF powder is preserved in the films. The XNLD measurements showed that the LiF at the surface does not have a perfect cubic symmetry. STM images showed that the branches of the LiF dendrites develop along the $< 010 >$ crystallographic directions of the Ag(100) surface, confirmed also by LEED diffraction patterns. The anisotropic growth is attributed to a strong ionic interaction of LiF dimers and a relatively weak interaction of the islands with the substrate, as well as to the thermodynamic conditions of the film deposition.

By increasing the amount of deposited material, the size and density of dendrites was detected to increase, along with a progressive out-of-plane inhomogeneous growth, detected by STM profiles. A general broadening of the LEED spots and a progressive disappearance of the (1,1) spots were found for LiF samples approaching a complete substrate coverage. The former behaviour was attributed to the growth of the LiF dendrites, which deviates from a perfect long-range order for samples of higher thicknesses, while the contribution to the diffraction from the Li and F atoms in the unit cell could explain the latter behaviour. The XAFS and the XNLD spectra displayed the same pattern for all the LiF thicknesses, meaning that no structural changes occured during the growth.

A higher intensity of the LEED spots and a drop of XNLD intensity signal of $\approx 50\%$ was detected for the thickest grown LiF sample ($\approx$ 4 monolayers). Indeed, a partial recovery of the cubic symmetry and a more ordered structure can be expected for such thickness of the LiF film.

The present study of ultrathin films of LiF deposited on Ag(100) surface at room temperature allows to understand the growth type of lithium fluoride at sub-monolayer to few monolayers coverage. This knowledge can be employed in further applications such as the growth of decoupling layer for Single Molecule Magnets, as well as other applications that requires ultrathin insulating films.

The interesting properties that emerged from this work suggest also that the LiF growth on Ag surface depends on the substrate temperature. Further investigations are

required in order to understand better the role of the temperature in the LiF growth and if a different substrate temperature can give rise to a different growth type.

Bibliography

[1] W. Sung and P. J. Park, "Polymer Translocation through a Pore in a Membrane," *Physical Review Letters*, vol. 77, pp. 783–786, jul 1996.

[2] H. Brune, "Microscopic view of epitaxial metal growth: nucleation and aggregation," *Surface Science Reports*, vol. 31, no. 4-6, pp. 125–229, 1998.

[3] M. A. Kats, R. Blanchard, P. Genevet, and F. Capasso, "Nanometre optical coatings based on strong interference effects in highly absorbing media," *Nature Materials*, vol. 12, no. 1, pp. 20–24, 2013.

[4] M. Birkholz, K. E. Ehwald, D. Wolansky, I. Costina, C. Baristiran-Kaynak, M. Fröhlich, H. Beyer, A. Kapp, and F. Lisdat, "Corrosion-resistant metal layers from a CMOS process for bioelectronic applications," *Surface and Coatings Technology*, vol. 204, no. 12-13, pp. 2055–2059, 2010.

[5] H. Kaiser, N. and Pulker, *Optical Interference Coatings*, vol. 88 of *Springer Series in Optical Sciences*. Berlin, Heidelberg: Springer Berlin Heidelberg, 2003.

[6] P. Bruno and C. Chappert, "Oscillatory coupling between ferromagnetic layers separated by a nonmagnetic metal spacer," *Physical Review Letters*, vol. 67, pp. 1602–1605, sep 1991.

[7] J. P. Velev, P. A. Dowben, E. Y. Tsymbal, S. J. Jenkins, and A. N. Caruso, "Interface effects in spin-polarized metal/insulator layered structures," *Surface Science Reports*, vol. 63, no. 9, pp. 400–425, 2008.

[8] J. W. Yoo, H. W. Jang, V. N. Prigodin, C. Kao, C. B. Eom, and A. J. Epstein, "Giant magnetoresistance in ferromagnet/organic semiconductor/ferromagnet heterojunctions," *Physical Review B - Condensed Matter and Materials Physics*, vol. 80, no. 20, pp. 1–9, 2009.

[9] F. Donati, S. Rusponi, S. Stepanow, C. Wackerlin, A. Singha, L. Persichetti, R. Baltic, K. Diller, F. Patthey, E. Fernandes, J. Dreiser, . Ljivan anin, K. Kummer, C. Nistor, P. Gambardella, and H. Brune, "Magnetic remanence in single atoms," *Science*, vol. 352, pp. 318–321, apr 2016.

[10] C. Wäckerlin, F. Donati, A. Singha, R. Baltic, S. Rusponi, K. Diller, F. Patthey, M. Pivetta, Y. Lan, S. Klyatskaya, M. Ruben, H. Brune, and J. Dreiser, "Single-Molecule Magnets: Giant Hysteresis of Single-Molecule Magnets Adsorbed on a Nonmagnetic Insulator (Adv. Mater. 26/2016)," *Advanced Materials*, vol. 28, no. 26, pp. 5142–5142, 2016.

[11] A. J. Nozik, M. C. Beard, J. M. Luther, M. Law, R. J. Ellingson, and J. C. Johnson, "Semiconductor Quantum Dots and Quantum Dot Arrays and Applications of Multiple Exciton Generation to Third-Generation Photovoltaic Solar Cells," *Chemical Reviews*, vol. 110, pp. 6873–6890, nov 2010.

[12] P. V. Kamat, "Quantum dot solar cells. Semiconductor nanocrystals as light harvesters," *Journal of Physical Chemistry C*, vol. 112, no. 48, pp. 18737–18753, 2008.

[13] R. D. Hoff, *Thermodynamics in Materials Science, Second Edition.* CRC Press, mar 2006.

[14] P. Arora, W. Li, P. Piecuch, J. W. Evans, M. Albao, and M. S. Gordon, "Diffusion of atomic oxygen on the Si(100) surface," *Journal of Physical Chemistry C*, vol. 114, no. 29, pp. 12649–12658, 2010.

[15] K. W. Kolasinski, *Surface Science.* Chichester, UK: John Wiley & Sons, Ltd, 2nd editio ed., apr 2012.

[16] D. D. McNamara, "How do eclogites deform in subduction and collision zones? An Alpine study," no. January 2009, p. 6, 2009.

[17] A. J. Newman, P. S. Krishnaprasad, S. Ponczak, and P. Brabant, "Modeling and Model Reduction for Control and Optimization of Epitaxial Growth in a Commercial Rapid Thermal Chemical Vapor Deposition Reactor," *Technical Report 98-45, Institute for Systems Research*, no. October 1998, 1998.

[18] H. Ibach, *Physics of surfaces and interfaces.* 2006.

[19] P. Pete, "Commercial Vacuum Pumps: A Summary of Styles & Applications," *http://blog.precisionplus.com/commercial-vacuum-pumps-a-summary-of-styles-applications/.*

[20] K. J. Lesker, "Turbomolecular Pumps," *https://www.lesker.com/.*

[21] D. M. Hoffman, U. David M. Sarnoff Research Center Princeton, New Jersey, B. Singh, U. David M. Sarnoff Research Center Princeton, New Jersey, I. John H. Thomas, and U. 3M Research Laboratories St. Paul, Minnesota, eds., *Handbook of Vacuum Science and Technology.* Elsevier, 1998.

[22] H. Brune, “Epitaxial Growth of Thin Films,” in *Surface and Interface Science*, pp. 421–492, Weinheim, Germany: Wiley-VCH Verlag GmbH & Co. KGaA, nov 2014.

[23] A. Devi, “‘Old Chemistries’ for new applications: Perspectives for development of precursors for MOCVD and ALD applications,” *Coordination Chemistry Reviews*, vol. 257, pp. 3332–3384, dec 2013.

[24] T. Kelwing, S. Mutas, M. Trentzsch, A. Naumann, B. Trui, L. Herrmann, F. Graetsch, C. Klein, L. Wilde, S. Ohsiek, M. Weisheit, A. Peeva, I. Richter, H. Prinz, A. Wuerfel, R. Carter, R. Stephan, P. Kücher, and W. Hansch, “Physical and electrical properties of MOCVD and ALD deposited HfZrO 4 gate dielectrics for 32nm CMOS high performance logic SOI technologies,” *ECS Transactions*, vol. 33, no. 3, pp. 3–14, 2010.

[25] M. Ohring, *The Materials Science of Thin Films*, vol. 2008. Chichester, UK: Elsevier, apr 1992.

[26] H. Ibach, “The role of surface stress in reconstruction, epitaxial growth and stabilization of mesoscopic structures,” *Surface Science Reports*, vol. 29, pp. 195–263, jan 1997.

[27] R. W. Balluffi, S. M. Allen, and W. C. Carter, *Kinetics of Materials*. Hoboken, NJ, USA: John Wiley & Sons, Inc., sep 2005.

[28] P. Benigni, A. Berche, G. Mikaelian, and J. Rogez, “Transformation of a double focusing B-E mass spectrometer for multiple-cell knudsen effusion - Part I: Scientific concepts,” *ECS Transactions*, vol. 46, no. 1, pp. 127–141, 2012.

[29] “Midwest Tungsten Service, Electron Beam Evaporation,” *https://www.tungsten.com/tips/electron-beam-evaporation/*.

[30] J. A. Venables, “Rate equation approaches to thin film nucleation kinetics,” *Philosophical Magazine*, vol. 27, pp. 697–738, mar 1973.

[31] I. Lifshitz and V. Slyozov, “The kinetics of precipitation from supersaturated solid solutions,” *Journal of Physics and Chemistry of Solids*, vol. 19, pp. 35–50, apr 1961.

[32] J. B. Hannon, C. Klünker, M. Giesen, H. Ibach, N. C. Bartelt, and J. C. Hamilton, “Surface self-diffusion by vacancy motion: Island ripening on Cu(001),” *Physical Review Letters*, vol. 79, no. 13, pp. 2506–2509, 1997.

[33] L. Makkonen, “Young’s equation revisited,” *Journal of Physics: Condensed Matter*, vol. 28, p. 135001, apr 2016.

[34] M. J. Powell, “VO2 Thin Films and Nanoparticles , from Chemical Vapour Deposition and Hydrothermal Synthesis, for Energy Efficient Applications,” *Help in Thesis*, no. September 2015, 2015.

[35] B. Movchan and A. Demchishin, “Structure and Properties of Thick Condensates of Nickel, Titanium, Tungsten, Aluminum Oxides and Zirconium Dioxide in Vacuum,” *The Physics of Metals and Metallography*, 1969.

[36] Y. Furukawa and H. Nada, “Anisotropy in microscopic structures of ice-water and ice-vapor interfaces and its relation to growth kinetics,” *Advances in the Understanding of Crystal Growth Mechanisms*, pp. 559–573, 2012.

[37] Y. Couder, N. Gérard, and M. Rabaud, “Narrow fingers in the Saffman-Taylor instability,” *Physical Review A*, vol. 34, pp. 5175–5178, dec 1986.

[38] P. J. Feibelman, “Self-diffusion along step bottoms on Pt(111),” *Physical Review B*, vol. 60, pp. 4972–4981, aug 1999.

[39] H. Brune, H. Röder, K. Bromann, K. Kern, J. Jacobsen, P. Stoltze, K. Jacobsen, and J. Norskov, “Anisotropic corner diffusion as origin for dendritic growth on hexagonal substrates,” *Surface Science*, vol. 349, pp. L115–L122, mar 1996.

[40] G. Messina, “Growth and Characterisation of Thermally- Evaporated Lithium Fluoride Thin Films for High-Energy Radiation Detectors Growth and Characterisation of Thermally- Evaporated Lithium Fluoride Thin Films for High-Energy Radiation Detectors,” 2013.

[41] K. Dupré, K. Recker, and F. Wallrafen, “Directional solidification of the LiF - LiBaF3 eutectic,” *Materials Research Bulletin*, vol. 27, pp. 311–318, mar 1992.

[42] E. Lück and G. v. R. Lipinski, “Organic Fluorine Compounds,” *Ulmann’s Encyclopedia of industrial chemistry*, pp. 671–692, 2012.

[43] D. Roessler and W. Walker, “Electronic spectrum of crystalline lithium fluoride,” *Journal of Physics and Chemistry of Solids*, vol. 28, pp. 1507–1515, aug 1967.

[44] D. S. McGregor, S. L. Bellinger, and J. Kenneth Shultis, “Present status of microstructured semiconductor neutron detectors,” *Journal of Crystal Growth*, vol. 379, pp. 99–110, 2013.

[45] J. Serp, M. Allibert, O. Beneš, S. Delpech, O. Feynberg, V. Ghetta, D. Heuer, D. Holcomb, V. Ignatiev, J. L. Kloosterman, L. Luzzi, E. Merle-Lucotte, J. Uhlíř, R. Yoshioka, and D. Zhimin, “The molten salt reactor (MSR) in generation IV: Overview and perspectives,” *Progress in Nuclear Energy*, vol. 77, pp. 308–319, nov 2014.

[46] H. Kim and A. H. King, "Grain growth and texture development in lithium fluoride thin films," *Journal of Materials Research*, vol. 23, no. 2, pp. 452–462, 2008.

[47] J. Bullock, P. Zheng, Q. Jeangros, M. Tosun, M. Hettick, C. M. Sutter-Fella, Y. Wan, T. Allen, D. Yan, D. Macdonald, S. De Wolf, A. Hessler-Wyser, A. Cuevas, and A. Javey, "Lithium Fluoride Based Electron Contacts for High Efficiency n-Type Crystalline Silicon Solar Cells," *Advanced Energy Materials*, vol. 6, no. 14, pp. 1–7, 2016.

[48] S. Prada, U. Martinez, and G. Pacchioni, "Work function changes induced by deposition of ultrathin dielectric films on metals: A theoretical analysis," *Physical Review B*, vol. 78, p. 235423, dec 2008.

[49] A. Balerna and S. Mobilio, *Introduction to Synchrotron Radiation.* 2015.

[50] "SLS Beamlines," *https://www.psi.ch/en/sls/beamlines-at-sls.*

[51] C. Piamonteze, U. Flechsig, S. Rusponi, J. Dreiser, J. Heidler, M. Schmidt, R. Wetter, M. Calvi, T. Schmidt, H. Pruchova, J. Krempasky, C. Quitmann, H. Brune, and F. Nolting, "X-Treme beamline at SLS: X-ray magnetic circular and linear dichroism at high field and low temperature," *Journal of Synchrotron Radiation*, vol. 19, no. 5, pp. 661–674, 2012.

[52] C. Schmitz-Antoniak, "X-ray absorption spectroscopy on magnetic nanoscale systems for modern applications," *Reports on Progress in Physics*, vol. 78, no. 6, p. 62501, 2015.

[53] R. Follath, "The versatility of collimated plane grating monochromators," *Nuclear Instruments and Methods in Physics Research, Section A: Accelerators, Spectrometers, Detectors and Associated Equipment*, vol. 467-468, pp. 418–425, 2001.

[54] A. Gupta and J. Leck, "An evaluation of the titanium sublimation pump," *Vacuum*, vol. 25, pp. 362–372, aug 1975.

[55] M. F. M. R. Group, "Scanning Tunnel Microscope," *http://home.iitk.ac.in/~gopan/index_files/STM.htm.*

[56] C. J. Chen, *Introduction to Scanning Tunneling Microscopy*, vol. 63. Oxford University Press, sep 2007.

[57] "Scienta Omicron, VT SPM," *https://www.scientaomicron.com/en/products/variable-temperature-spm.*

[58] S. A. et al. Oura K., Lifshitz V. G., *Introduction to surface physics (rus).* 2006.

[59] A. Mermin, “Solid State Physics. Von N. W. Ashcroft und N. D. Mermin; Holt, Rinehart and Winston, New York 1976, XXII, 826 Seiten, $19,95,” *Physik in unserer Zeit*, vol. 9, no. 1, pp. 33–33, 1978.

[60] Jurgen Klein, *Epitaktische Heterostrukturen aus dotierten Manganaten*. PhD thesis, 2001.

[61] “John Morris Group, ErLEED 100/150,” *https://www.johnmorrisgroup.com/AU/Product/197833/ 100150*.

[62] “Kurt J. Lesker, Front Load Sputtering Sensor,” *https://www.lesker.com/newweb/process_instruments/processequipment_inficon_frontload_sputterin*

[63] M. Balasubramanian, H. S. Lee, X. Sun, X. Q. Yang, A. R. Moodenbaugh, J. McBreen, D. A. Fischer, and Z. Fu, “Formation of SEI on Cycled Lithium-Ion Battery Cathodes: Soft X-Ray Absorption Study,” *Electrochemical and Solid-State Letters*, vol. 5, no. 1, p. A22, 2002.

[64] E. Kobayashi, K. K. Okudaira, and T. Okajima, “Effects of annealing on the molecular orientation in polytetrafluoroethylene thin films,” *Surface and Interface Analysis*, vol. 44, no. 6, pp. 740–743, 2012.

[65] R. M. Montereali, G. Baldacchini, S. Martelli, and L. C. S. Do Carmo, “LiF films: Production and characterization,” *Thin Solid Films*, vol. 196, no. 1, pp. 75–83, 1991.

[66] D. G. Castner, K. B. Lewis, D. A. Fischer, B. D. Ratner, and J. L. Gland, “Determination of Surface Structure and Orientation of Polymerized Tetrafluoroethylene Films by Near-Edge X-ray Absorption Fine Structure, X-ray Photoelectron Spectroscopy, and Static Secondary Ion Mass Spectrometry,” *Langmuir*, vol. 9, no. 2, pp. 537–542, 1993.

[67] C. Sugiura, “K α X-Ray Emission Spectra and K X-RayAbsorption-Edge Structures of Fluorinein 3 d Transition-Metal Difluorides,” *Journal of the Physical Society of Japan*, vol. 60, pp. 2710–2717, aug 1991.

[68] I.-K. Suh, H. Ohta, and Y. Waseda, “High-temperature thermal expansion of six metallic elements measured by dilatation method and X-ray diffraction,” *Journal of Materials Science*, vol. 23, pp. 757–760, feb 1988.

[69] D. L. Howlett, J. E. Lester, and G. A. Somorjaj, “Vacuum vaporization studies of lithium fluoride single crystals,” *The Journal of Physical Chemistry*, vol. 75, no. 26, pp. 4049–4053, 2005.

[70] P. W. Palmberg and T. N. Rhodin, “Surface structure of clean Au (100) and Ag (100) surfaces,” *Physical Review*, vol. 161, no. 3, pp. 586–588, 1967.

[71] J. Wang, *Low Energy Electron Diffraction Studies of Transition Metal Oxide Surfaces and Films*, vol. 4. 2005.

[72] F. Mechehoud and C. Barth, "Morphology, Work Function, and Silver Ad-Structures of High-Temperature Grown Ultrathin MgO Films on Ag(001)," *Journal of Physical Chemistry C*, vol. 119, no. 42, pp. 23990–23995, 2015.

[73] A. Ouvrard, J. Niebauer, A. Ghalgaoui, C. Barth, C. R. Henry, and B. Bourguignon, "Characterization of thin MgO Films on Ag(001) by low-energy electron diffraction and scanning tunneling microscopy," *Journal of Physical Chemistry C*, vol. 115, no. 16, pp. 8034–8041, 2011.

[74] S. Valeri, S. Altieri, A. di Bona, P. Luches, C. Giovanardi, and T. Moia, "Thickness-dependent strain in epitaxial MgO layers on Ag()," *Surface Science*, vol. 507-510, pp. 311–317, jun 2002.

[75] J. G. Roberts, M. A. Van Hove, and G. A. Somorjai, "Surface structural analysis of LiF(1 0 0) thin films grown on Pt(1 1 1)," *Surface Science*, vol. 518, no. 1-2, pp. 49–56, 2002.

[76] B. Poelsema, A. Acun, L. Schouten, F. Derkink, M. Tsvetanova, Z. Zhang, H. J. W. Zandvliet, and A. van Houselt, "Polar edges and their consequences for the structure and shape of hBN islands," *2D Materials*, vol. 6, p. 035010, apr 2019.

[77] U. Kaiser, N. Kaiser, P. Weißbrodt, U. Mademann, E. Hacker, and H. Müller, "Structure of thin fluoride films deposited on amorphous substrates," *Thin Solid Films*, vol. 217, no. 1-2, pp. 7–16, 1992.

Acknowledgements

First of all, I would like to thank my supervisor prof. Federico Boscherini who inspired my accademic interests, showed me how fascinating the world of X-ray spectroscopy is and constantly followed me at all the steps of the thesis work.

I would like to acknowledge all my collegues from the "Magnetism and Microscopy" group, who supported me and helped me througout my stay at the Swiss Light Source, which made me feel welcomed and part of such an amazing research group. Special thanks goes to my local supervisor, doc. Jan Dreiser, for his precious advices and his constant positive and kind attitude, which made me love the experimental work I did at the X-Treme beam line.

I would also like to thank Francesca Neri for her extraordinary support, which constantly pushed me forward and motivated me to give always my best. In addition, I would like to thank my parents for their emotional and practical support, which allowed me to pursue my dreams all this years.

Finally, I thank all my friends and the people who always supported me and believed in my success, which gave me the strength to persue my goals and overcome the troubles met along the way.